Università degli Studi di Torino
Scuola di Dottorato

Modeling gravitational waves using the effective-one-body approach

Piero Rettegno

Università degli Studi di Torino
Scuola di Dottorato

Dottorato in Fisica

Modeling gravitational waves using the effective-one-body approach

Piero Rettegno

Tutors: Nicolao Fornengo, Alessandro Nagar

1 Abstract

The detection of gravitational waves by the LIGO and Virgo interferometers has changed the way we look at the universe. We are now able to use gravitational interactions to study astrophysical phenomena that used to be invisible. Through gravitational waves, we can also test physics in extreme conditions, such as near black hole event horizons and inside neutron stars.

The analysis of gravitational wave signals emitted by compact binary coalescence rely on accurate theoretical predictions. These are obtained by solving Einstein's equations using either analytical perturbative approaches or numerical methods. The most accurate semi-analytical models at the moment are based on the effective-one-body approach and are completed using numerical relativity information.

In this thesis, after briefly introducing these models, I will present three of the collaborative works I contributed to during my PhD.

The first will compare the two main families of models based on the effective-one-body framework, highlighting their main structural differences. These types of studies are necessary to understand the theoretical uncertainty waveform approximants inherently possess.

The second will describe the building of a gravitational wave model for hyperbolic encounters and dynamical captures of black hole binaries. An accurate theoretical prediction of the signal emitted in these scenarios is nowadays missing and it is needed to complement the current analyses based on models for quasi-circular binaries.

Finally, the third will detail the development of a complete model, able to generate waveforms for quasi-circular, eccentric and hyperbolic systems with sufficient accuracy to be used in parameter estimation of future detections.

Contents

2 Introduction

The first direct detection of gravitational waves (GWs) by the Laser Interferometer Gravitational-Wave Observatory (LIGO) detectors on September 14, 2015 [1] was a watershed moment for astrophysics: it marked the beginning of GW astronomy. The GW150914 event implied the existence of stellar-mass black hole (BH) binaries and proved that General Relativity (GR) predictions were consistent with the observations. This happened around a hundred years after Einstein discovered that GR implied the propagation of gravitational waves [2, 3] and that Schwarzschild demonstrated it permitted the existence of BHs [4].

Two years later, on August 17, 2017 the three LIGO and Virgo detectors captured the GW signal originated by the merger of a binary neutron star (BNS) system [5]. This detection and the following observation of the electromagnetic (EM) counterpart [6] were of similar importance, being the first demonstration of GW-EM multi-messenger astronomy.

2.1 Gravitational wave detectors

The first attempt at detecting GWs was made with resonant bars [7, 8], massive aluminum cylinders that would vibrate at the passing of a GW with a specific resonance frequency. However, claims of GW detections with resonant bars were never confirmed.

Current ground-based observatories, such Advanced LIGO [9] and Virgo [10] as well as KAGRA [11], use enhanced Michelson interferometry with suspended mirrors. They measure variations in the light travel time between separated test masses, configured such that each is in near free fall. With arm lengths of 3 to 4 kilometers, they are able to reach displacement sen-

sitivities of less than 10^{-19} meters. These interferometers are sensitive to GW frequencies between 10 Hz and 10 kHz, a band dominated by stellar-mass compact binaries, and (theoretically) rotating neutron stars (NSs) and supernovae. A network of such detectors globally distributed is beneficial to better constrain the position of the GW source.

Plans to build a third generation of GW detectors are underway. These include two ground-based detectors, Cosmic Explorer (CE) [12] and Einstein Telescope (ET) [13], and a space-based one, the Laser Interferometer Space Antenna (LISA) [14]. CE will follow the same layout of the current generation of observatories, but will improve on their sensitivity, in particular by increasing the arm lengths to around 40 kilometers. ET, instead, will be an underground facility hosting a triangle-shaped interferometer. It will increase the arm size to around 10 kilometers and implement new technologies, most notably a cryogenic system to cool some of the optics to around 10-20 K. Both ET and CE will be significantly more sensitive than current interferometers and will be able to detect stellar mass binary coalescence throughout the history of our universe. They will allow for tighter measurements of the source parameters and more precise tests of GR. The LISA mission instead is scheduled to launch around 2035 and will be constituted by three spacecraft that will form an equilateral triangle with arm lengths of around 2.5 million kilometers. Being in space allows for longer laser path lengths and eludes most of the noise sources present on Earth, but makes the instrument more susceptible to laser power limitations and diffraction losses. These characteristics make LISA more suitable for lower frequency bands, from around 100 μHz to 100 mHz. In this band, it will be able to detect mergers of intermediate-mass and supermassive BHs, as well as extreme mass-ratio mergers of stellar-size objects and supermassive BHs. It will also probably see the early inspiral of stellar mass BBHs

whose merger would be detected by ground-based interferometers years later, providing very precise sky localization of the events to help the search for an EM counterpart [15].

2.2 Current detections

The first three observation runs of the LIGO and Virgo interferometers resulted in a total of 91 merger detections [16, 17, 18, 19]. Most of the observed systems are inferred to be BBHs and only two are considered to be BNSs, with GW190425 [20] being the second after GW170817. There was however no clear detection of an EM counterpart in coincidence with GW190425, confirming the extraordinary nature of the GW170817 observation. There are 4 events consistent with originating from a mixed BH-NS system [21, 22] and 2 more that could be interpreted as either BBHs or BH-NS binaries. These considerations are mainly based on the inferred individual masses (considering NSs any object with mass smaller than 3 $M_\odot$ [23, 24]), since a measurement of tidal effects themselves is much more complicated.

Masses are generally the best constrained source parameters. In particular, combinations of individual masses such as the chirp mass [25] and the total mass are more precisely measured than the two component masses. The chirp mass is the greatest influence on the GW signal during the inspiral phase, making it better constrained in lower-mass systems, where the inspiral lies in the most sensitive frequency band of the detectors. On the contrary, the total mass determines the merger-ringdown waveform and is hence more precisely measured for higher-mass sources. The higher total mass measured so far is around 150 $M_\odot$. The BHs observed through GWs to date span a wide range of masses from just under 10 $M_\odot$ to almost 100 $M_\odot$. Most BBH observations are consistent with equal mass or marginally un-

equal mass binaries, although two of the events show inferred mass ratios around 5. The remnants BHs formed in these mergers have masses similar to the total mass of the original binary, since the energy radiated in GWs generally corresponds to a few percent of the starting total mass. Some of the heaviest remnants are consistent with being intermediate-mass black holes (IMBHs) [26]. As for systems containing a candidate NS, they generally have more extreme mass ratios, with the highest one being inferred to be more than 20. Because of the relatively small number of NS observations it is more difficult to extract useful information about the population of these objects throughout the universe. It seems however that the inferred NSs have a relatively flat mass distribution extending from 1.2 to 2.0 $M_{\odot}$.

Spins have more subtle effects on the emitted GWs and are hence harder to measure. In particular, we are able to precisely infer only some combinations of the individual masses and spins [27, 28, 29, 30, 31, 32]. Most of the observed objects are consistent with non-spinning bodies. However, there are binaries than support non-negligible spins, both aligned and anti-aligned with the orbital angular momentum of the binary. We also observe evidence of misalignment of spins relative to the orbital angular momentum, which gives rise to precessing systems. The observation of such precessional signatures could be important in order to distinguish different BBH formation scenarios [33, 34].

Almost every analysis of GW signals from coalescing binaries is done under the assumption that the inspiral is quasi-circular. This is because GW emission is very efficient in circularizing isolated binaries before they enter the detectors frequency band. However, population studies [35, 36, 37, 38, 39, 40] suggest that binaries dynamically formed in active galactic nuclei and globular clusters may still possess some eccentricity that could be detected by ground-based detectors. At the moment, no evi-

dence of eccentricity has been found [41, 42, 43].

2.3 Scientific insights

GWs are a powerful probe of the universe, because of their use of gravity instead of electromagnetism to measure astrophysical systems. Measuring GWs is often compared to hearing the universe, opening the possibility to study phenomena that would otherwise be invisible.

Since GWs generated by compact binaries carry characteristic information about the astrophysical properties of the objects, we are able to constrain the mass and spin distributions of BHs and NSs. Together with their estimated rate of mergers (and possibly the binary eccentricity), they help us understand their formation channels and evolution. The current detections of GW events have already demonstrated the existence of BHs in previously unexplored mass ranges [44].

The observation of GWs from inspiralling BBHs provides us the possibility of performing precision tests of GR near BH horizons, that is in the high-curvature, strong-field regime [45, 46, 47, 48, 49, 50, 51]. For instance, we can put constraints on the graviton mass, violations of local Lorentz invariance, and additional GW polarizations [52, 53, 54, 55]. Due to the current absence of accurate waveforms derived in alternative theories of gravity, we cannot directly compare GR predictions to other specific theories. We can however check the self-consistency of our analyses or introduce parameterized deviations from GR in the waveform and check that these are compatible with 0. To date, all GW detections are consistent with GR predictions [48, 50]. For example, subtracting the maximum-likelihood GR waveform from the data finds residuals consistent with the detector noise and there is no evidence for non-tensor polarization modes or dispersion of GWs. At the moment, however, the limits on devi-

ations from GR are still dominated by the statistical uncertainty due to the detector noise.

The next generation of detectors [13, 14, 12] will be significantly more sensitive than current ones and will be able to probe the existence of stellar-mass BHs throughout the history of the universe. They will allow us to measure more accurately BH masses and spins, perform more precise tests of GR [56, 57, 58] and possibly even enable us to perform BH spectroscopy by measuring individual quasi-normal modes [59, 60]. The detection of hundreds of BBHs with different redshifts will allow to probe fundamental physics spanning a wide range of energy scales [61, 62], gaining insights on the nature of dark energy and possible modifications of GR at cosmological scales. By associating GW sources to nearby galaxies, it will be also possible to make an independent measure of the Hubble constant [63], that could clear up the tension between the local and early universe measurements [64].

The detection of BNS mergers instead sheds light on the interior structure of NSs and on fundamental properties of cold high-density matter [65, 66, 67, 68, 69, 70]. In fact, we still do not have a good understanding of the internal composition of NSs. At the moment, detected BNSs determined the NS radii to be between 9 and 13 kilometers [70] and strongly disfavor the stiffest equations of state (EOS), which predict NSs not compact enough to match the observations. The GW170817 detection alone [5], with the subsequent observations of its electromagnetic counterpart [6], was the first demonstration of the link between BNS mergers and short gamma-ray bursts [71, 72, 73, 74, 74, 75, 76, 77, 78, 79] and the first definitive observation of a kilonova [80, 81, 82, 83, 84, 85, 86]. It also entailed the production of heavy elements through r- process nucleosynthesis during the merger [87, 88, 89, 90, 91, 92]. Perhaps most importantly, the multi-messenger signal proved that GWs travel at the speed

of light (as predicted by GR) to astounding precision (a few parts in 10^{15}). This measurement also provided an independent method for measuring the Hubble constant using GWs for determining the absolute distance to the source [93, 94, 95]. Basically, these multi-messenger observations allowed to use GW170817 as a standard siren, the GW analog of an astronomical standard candle.

Detecting more BNS events will put more limiting constraints on the NS EOS and will better determine the spectrum of NS masses throughout the universe, which in turn will provide insights into the physics of supernovae. Joint gravitational and EM observations will help us understand the NS matter properties, the nature of mass ejecta following BNS mergers and the structure of relativistic jets.

BHs and NSs mergers could also provide insights into the nature of dark matter [96], either directly as primordial BHs [97] or through the effects that dark matter would have on the binary dynamics and hence on the emitted GWs [61, 98].

2.4 Data analysis and parameter estimation

In order to detect and extract a signal from a detector noise, GW scientists use match filtering [99, 100, 101, 102], the optimal linear filter for signals buried in noise. This method relies on waveform templates that correctly describe the GWs emitted by merging systems for a range of different configurations. A real GW signal should also match in all interferometers (bearing in mind detectors blind spots) with a time difference depending on the source position and at most equal to the light travel time between the instruments.

By comparing the observational data with theoretical templates, it is possible to infer the original binary parameters via Bayesian inference [103, 104, 105, 106, 107, 108, 109, 110]. This

task can only be tackled numerically through stochastic samplers, mainly because of the large dimensionality of the parameter space. For quasi-circular, non-spinning binary systems, we need to simultaneously determine 9 parameters: 2 component masses, luminosity distance, sky location (right ascension and declination), system orientation with respect to the line of sight (inclination and polarization angles), time of coalescence and a reference phase. The parameter space can grow even larger integer if more detailed physics is included in the gravitational models. For example, if we take into account spin effects, the parameter space becomes 15-dimensional (11-dimensional if we restrict to the aligned-spin case). The system eccentricity can be derived including an additional parameter. The dimensionality increases as well if we want to also determine the nature of the objects that generated the GW signal. In fact, if the binary was composed of NSs, their tidal deformabilities have to be simultaneously estimated.

Generally, one should expect to compare the detector data with around 10^7 waveforms generated by a chosen theoretical model. This requires GW approximants to also be fast computationally, since even a waveform generation time of one second could result in months-long parameter estimation runs.

2.5 Theoretical models

We have seen that most analyses on GW signals relies on accurate theoretical predictions that link source parameters to waveforms. However, Einstein's equations are non-linear and it is generally impossible to exactly solve them. As it is custom when facing these situations, we can approach the problem from two different directions, either relying on analytical approximations or using numerical methods.

2.5.1 Numerical relativity

Numerical relativity (NR) is the branch of GR that uses numerical methods to solve the general relativistic two-body problem in its full generality.

The numerical simulations are a very powerful tool, since they constitute the most accurate representation of the dynamics and GW emission of a binary system in the strong-field regime. They are also important because they provide the complete waveform through merger and ringdown. Their main downside historically is their heaviness in terms of computing power.

The first simulations of BBH mergers date back to the "NR breakthrough" in 2005 [111, 112]. At the beginning, they were restricted to the computation of the last few orbits of equal-mass non-spinning BBHs. Nowadays simulations explore spinning (and spin-precessing) binaries, eccentric-orbit systems, and longer evolutions [113, 114, 115, 116, 117, 118, 119, 120]. However, the sampling in the parameter space is still sparse, with very long waveforms, large mass ratios and high spins still posing difficult challenges.

The available NR waveforms can be interpolated to build surrogate models [121, 122, 123], which at the moment constitute the most accurate models available but are limited in waveform length and parameter space coverage. The merger-ringdown waveforms obtained from NR simulations are also a key ingredient in the construction and verification of other accurate waveform models used in GW data analysis: effective-one-body (EOB) models and phenomenological waveforms (we will discuss both of these shortly).

NR simulations are able to also describe BH-NS and BNS systems. In these cases, simulations are more complex and must include detailed physics for the nuclear, electromagnetic and weak interactions [124, 125, 126, 127, 128]. As is the case for

BBHs, NR simulations are the only tool we have to accurately model the merger waveform and final remnants. These latter are determined by an interplay of all types of interactions and can be constituted by a BH or a (short or long-lived) NS and various types of mass ejecta. As a consequence, a waveform emitted by a BNS will look very similar to one generated by a BBH in the inspiral regime, having the typical chirping form, but could differ drastically in the postmerger phase.

2.5.2 Perturbative expansions

The only way to approach the solution of Einstein's equations analytically is to assume some approximation.

The most common one is the post-Newtonian (PN) approximation [129, 130, 29, 131, 132, 133, 134, 135, 136, 137, 138], an expansion in the typical source velocity around the Newtonian solution. It is valid in the slow-motion, weak-field regime and hence it is well-suited for describing the motion of compact binaries in the inspiral phase. It starts to lose its validity at small separations, when the system goes towards plunge and merger.

Another possibility consists in solving Einstein's equations around Minkowski's solution, using Newton's constant G as a formal expansion parameter. This post-Minkowskian (PM) approximation [139, 140, 141, 142, 143, 144, 145, 146, 147, 148] also breaks down near the end of a binary system evolution, when the assumption of weak fields no longer holds true. This approach is particularly suitable for unbound systems, when the object velocities can be relativistic without entering the strong-field regime.

Finally, the gravitational self-force (GSF) approach [149, 150, 151, 152, 153, 154, 155, 156] studies perturbations around the Schwarzschild (or Kerr) solution using the mass ratio as expansion parameter.

Using analytical approximations we can also gain some insight in the ringdown waveform. The quasi-normal mode spectrum emitted after a merger resulting in a perturbed BH can be described by BH perturbation theory [157, 158]. While the analytic prescription provides the mode frequencies and damping times, it does not determine the amplitude of the waves, that must be extracted with the help of numerical simulations [159].

We are also able to model the tidal deformations of NSs due to the gravitational field of its companion. Such effects depend on the EOS and enter the PN expansion at the fifth PN order [160, 161, 162].

2.5.3 Effective-one-body approach

The EOB approach [163, 164, 165, 27] to the general relativistic two-body problem is a way to map the binary dynamics into an effective one-body problem of a test particle moving in an external effective metric. This metric is a deformation of the Schwarzschild (or Kerr) one, with a deformation parameter that depends on the mass ratio of the original binary. This continuous link between the test-mass case, where GR is exactly solvable, and the equal-mass one is of paramount importance. It allows to meaningfully resum perturbative information in order to accurately describe the dynamics during the late stages of inspiral and plunge.

The currently most accurate semi-analytical models are built using PN series resummed through the EOB prescription and completed by NR information [166, 167], that is needed to correctly model the merger and ringdown parts of the waveforms. Nowadays, EOB-NR models are able to take into account higher harmonics and precession [168, 169], while the building of reliable approximants for eccentric orbits is underway [170, 171, 172, 173, 174].

EOB-NR models are very accurate and allow us to have control over the underlying physics so that they can be easily modified, for example to take into account beyond GR effects. The downside of such models is that they generally require to solve a system of coupled ordinary differential equations (Hamilton's equations), which makes the waveform generation rather costly. This drawback must be mitigated, at the cost of a slight reduction in accuracy through the building of surrogate models [175, 176, 177, 178] or by using approximations during the early inspiral [179, 178, 180, 181].

2.5.4 Phenomenological models

Another approach to waveform generation consists in building phenomenological approximants [182, 183, 31, 184, 185, 186, 187]. These focus only on modeling the frequency domain GW signal without solving equations of motions for the binary system, aiming to be as fast as possible for data analysis purposes.

In order to do so, they model separately the amplitude and phase of the waveforms and split them in three regions. The inspiral region is modeled using PN series typically calibrated using EOB-based models. The late inspiral and the ringdown are modeled using different functional forms but are both calibrated to NR results.

State-of-the-art phenomenological approximants are able to generate multipolar waveforms for precessing systems [188, 186]. Nowadays, their accuracy is comparable to the ones of EOB-NR models [186, 187, 189], while being 3-4 times faster than their surrogates [168, 187].

Both EOB-NR and phenomenological waveforms can be extrapolated beyond the limitations of NR surrogates, but their accuracy and validation strongly depend on the availability of NR simulations.

3 EOB-NR models

At the moment, there are two families of state-of-the art EOB-NR models. One is `TEOBResumS` [190, 191, 192, 166, 179, 193, 194, 195, 196, 170, 178, 168, 171] and the other is the `SEOBNRv*` series [197, 198, 199, 200, 201, 202, 203, 204, 205, 206, 175, 167, 169]. Their most recent iterations are able to compute waveforms generated by compact binary coalescence, taking into account spin contributions (including spin-orbit precession) and tidal effects.

Lately, a lot of effort has been put into extending their scope beyond quasi-circular orbits, so to compute GWs emitted by systems in eccentric or hyperbolic orbits [170, 171, 207, 208, 173]. Eccentric waveform models will be fundamental in order to analyse data from extreme-mass-ratio-inspirals (EMRIs) that could be detected by LISA. Hyperbolic ones instead will help in discerning scatterings and dynamical captures from highly precessing systems [209]. These extensions are however not yet accurate enough to be used for data analysis purposes, mostly because of the lack of NR simulations to be used for calibration and validation.

While the `TEOBResumS` and `SEOBNRv*` models share the foundational aspects of the EOB framework, they do not always produce the same results. In fact, they differ not only in the amount of analytical information used to build them, but most notably in a series of arbitrary decisions, such as resummations and gauge choices that have to be made along the way.

3.1 Effective-one-body basics

The EOB method maps the two-body dynamics into a point particle moving in an effective metric [163, 164, 27]. The formalism utilises ideas coming from quantum mechanics to build the map-

ping and obtains a relation between the relativistic energies in the real and effective systems, such as

$$\frac{E_{\rm eff}}{\mu} = \frac{(E_{\rm real})^2 - m_1^2 - m_2^2}{2\, m_1\, m_2}. \tag{1}$$

where m_1 and m_2 are the masses of the objects in the original system and $\mu \equiv (m_1 m_2)/(m_1 + m_2)$ is the reduced mass.

This quadratic relation translates to the μ-rescaled EOB Hamiltonian, obtained from the effective Hamiltonian by means of

$$\hat{H}_{\rm EOB} \equiv \frac{H_{\rm EOB}}{\mu} = \frac{1}{\nu}\sqrt{1 + 2\nu\left(\hat{H}_{\rm eff} - 1\right)}, \tag{2}$$

where we introduced the symmetric mass ratio $\nu \equiv \mu/M$, with M being the total mass of the system. ν varies continuously varies between 0, for a test-mass orbiting a BH, and 1/4 in the equal-mass case.

The effective metric is a deformation of the Schwarzschild (Kerr) one, with ν as a deformation parameter. The effective metric, using dimensionless coordinates defined as [$r \equiv R/M$, $t \equiv T/M$, $p_r \equiv P_r/\mu$, $p_\varphi \equiv P_\varphi/(\mu M)$], is written in the form

$$ds^2 = -A(r;\nu)dt^2 + B(r;\nu)dr^2 + r^2 d\Omega, \tag{3}$$

with

$$B(r;\nu) = \frac{D(r;\nu)}{A(r;\nu)}, \tag{4}$$

where A and D are the EOB metric potentials.

The effective Hamiltonian will then be written as

$$\hat{H}_{\rm eff} = \sqrt{A(r;\nu)\left[1 + \frac{p_\varphi^2}{r^2} + \frac{p_r^2}{B(r;\nu)} + Q(r, p_r;\nu)\right]} + \hat{H}_{\rm eff}^{\rm SO} + \hat{H}_{\rm eff}^{\rm SS}, \tag{5}$$

where Q is the third EOB potential and $\hat{H}_{\rm eff}^{\rm SO}$ and $\hat{H}_{\rm eff}^{\rm SS}$ are the spin-orbit and spin-spin Hamiltonians.

In order to determine the dynamics of the system, one still needs to choose a a representation of the radiation reaction due to the emission of GWs. Then, we can solve Hamilton's equations:

$$\begin{aligned} \frac{d\mathbf{x}}{dt} &= \frac{\partial \hat{H}_{\mathrm{EOB}}}{\partial \mathbf{p_x}}, \\ \frac{d\mathbf{p_x}}{dt} &= -\frac{\partial \hat{H}_{\mathrm{EOB}}}{\partial \mathbf{x}} + \hat{\mathcal{F}}_{\mathbf{x}}, \\ \frac{d\mathbf{S_i}}{dt} &= \frac{\partial \hat{H}_{\mathrm{EOB}}}{\partial \mathbf{S_i}} \times \mathbf{S_i}, \end{aligned} \tag{6}$$

where $\mathbf{x} = \{r, \varphi, \theta\}$ is the coordinate vector, $\mathbf{p_x} = \{p_r, p_\varphi, p_\theta\}$ is the momentum vector and $\hat{\mathcal{F}}_{\mathbf{x}} = \{\hat{\mathcal{F}}_r, \hat{\mathcal{F}}_\varphi, \hat{\mathcal{F}}_\theta\}$ contains the three radiation reaction fluxes.

The model is finally completed by a prescription to compute the waveform emitted towards infinity. To preserve the model internal consistency, this is usually the same used for radiation reaction.

3.2 Resummation choices

Of course, even within the EOB framework, we cannot reach an exact solution to Einstein's equations. Both the EOB potentials and fluxes are still to be determined using some other approach, most commonly PN expansions. The strength of the EOB methods consists in imposing a non-linear resummation to the Hamiltonian, which helps to stabilize the (asymptotic) PN series.

The idea behind its functioning is that instead of expanding a structure directly in a polynomial series, it imposes an exact general behaviour and expands only the residual substructures. In particular, instead of using a polynomial representation of the Hamiltonian (as it is done in PN approximants), EOB models use an Hamiltonian containing square roots, within which

the A potential is obtained by (subsequently resummed) PN series [210, 200, 190].

The same is done for the multipolar waveform, where the different modes are not just expanded as PN series. Known structures, such as a source term, motivated by the particle limit expression, or tail effects are imposed to the final functional form [211, 212, 213, 214, 215, 216].

Imposing the EOB resummation and all exact behaviours we have knowledge of is still not enough to have an accurate GW approximant. In fact, we still have to choose resummations for all the residual PN series and determine the gauge for the spin sector among other things. This is the main reason why the different families of EOB-based models diverge. All these choices are arbitrary, but necessary. Keeping PN series in their polynomial form is itself a form of resummation, even though it may seem more natural. Furthermore, a high-order PN polynomial will diverge very fast when approaching the plunge, when the system velocities increase, making it completely unreliable. A correctly chosen resummation will instead make the series more stable and accurate during the late stages of the evolution.

3.3 Numerical relativity completion

Both the intrinsic (EOB) and the arbitrary resummations help extend the usefulness of perturbative expansions beyond the early inspiral regime. However, NR information is fundamental to achieve the desired accuracy during the late inspiral and plunge [217, 218, 219]. Thus, fictitious parameters can be added to the dynamics and waveform at high order. These are then fitted to NR simulations so that the resulting GWs are consistent with numerical results up to some degree.

Moreover, EOB approximants have no way to model the post-merger and ringdown waveform. Hence, this part is generally

modeled using NR fits and a smooth transition between the inspiral and postmerger waveforms is required [220, 210, 200, 221, 222].

3.4 `TEOBResumS` model overview

We briefly introduce here the main structures entering the `TEOBResumS` waveform model, that will be central in the following Chapters. We will repeat some of the definitions when necessary, the most used parameters and symbols are reported in Appendix A.

3.4.1 Non-spinning Hamiltonian

Within `TEOBResumS`, the orbital (non-spinning) effective Hamiltonian entering Eq. (2) is written as

$$\hat{H}^{\rm orb}_{\rm eff}\big|_{(S_i=0)} \equiv \frac{H^{\rm orb}_{\rm eff}\big|_{(S_i=0)}}{\mu} = \sqrt{p^2_{r_*} + A_{\rm orb}(r)\left[1 + \frac{p^2_\varphi}{r^2} + Q_{\rm orb}(r, p_{r_*})\right]}, \tag{7}$$

where we introduced $p_{r_*} \equiv \sqrt{A/B}\, p_r$, the radial momentum conjugated to the tortoise radial coordinate r_*.

The EOB potentials A, B and Q are expressed as PN series and are currently known at 5th PN level:

$$\begin{aligned} A_{\rm 5PN}(u) &= 1 - 2u + 2\nu\, u^3 + \nu a_4\, u^4 + \nu\left[a^c_5 + a^{\log}_5\, \ln(u)\right] u^5 + \\ &\quad + \nu\left[a^c_6 + a^{\log}_6\, \ln(u)\right] u^6, \end{aligned} \tag{8}$$

$$D_{\rm 5PN}(u) = 1 - 6\nu\, u^2 - \left(52\nu - 6\nu^2\right) u^3 + d_4\, u^4 + d_5\, u^5, \tag{9}$$

$$\begin{aligned} Q_{\rm 5PNloc}(u, p_{r_*}) &= 2\nu(4 - 3\nu)\, u^2 p^4_{r_*} + \\ &\quad + \left(q_{43} u^3 p^4_{r_*} + q_{62} u^2\, p^6_{r_*} + \mathcal{O}[u p^8_{r_*}]\right) + \\ &\quad + \left(q_{44{\rm loc}} u^4 p^4_{r_*} + q_{63{\rm loc}} u^3 p^6_{r_*} + q_{82{\rm loc}} u^2 p^8_{r_*} + \mathcal{O}[u p^{10}_{r_*}]\right), \end{aligned} \tag{10}$$

with $B_{5\mathrm{PN}} \equiv D_{5\mathrm{PN}}/A_{5\mathrm{PN}}$ and $u \equiv 1/r$. The explicit values of the 4PN and 5PN coefficients [1] can be found in Ref. [135] and will be reported in Chapter 6.

In all iterations of `TEOBResumS`, before the version presented in Chapter 6, the A potential is taken effectively at 5th PN order, with a_6^c being an effective parameter informed by NR simulations. The series is then resummed as

$$A_{\mathrm{orb}}(r) = \mathrm{P}^1_5\big[A^{\mathrm{eff}}_{5\mathrm{PN}}(r; a_6^c)\big]. \tag{11}$$

The D and Q potentials are instead included at 3PN order, with D being inversely resummed, as

$$\begin{aligned} D_{\mathrm{orb}}(r) &= \mathrm{P}^0_3\big[D_{3\mathrm{PN}}(r)\big], \\ Q_{\mathrm{orb}}(r, p_{r_*}) &= Q_{3\mathrm{PN}}(r, p_{r_*}). \end{aligned} \tag{12}$$

The version of `TEOBResumS` that will be introduced in Chapter 6 will instead make use of the recently computed 5PN series, using

$$\begin{aligned} A_{\mathrm{orb}}(r) &= \mathrm{P}^3_3\big[A^{\mathrm{eff}}_{5\mathrm{PN}}(r; a_6^c)\big], \\ D_{\mathrm{orb}}(r) &= \mathrm{P}^3_2\big[D_{5\mathrm{PN}}(r)\big], \\ Q_{\mathrm{orb}}(r, p_{r_*}) &= Q_{5\mathrm{PNloc}}(r, p_{r_*}). \end{aligned} \tag{13}$$

Note that the explicit value of the effective parameter a_6^c will be different, as it must be re-tuned every time a part of the model is changed.

3.4.2 Spin contributions

Let us first define the projections of the spins along the direction of the orbital angular as $S_i \equiv \boldsymbol{L} \cdot \boldsymbol{S_i}$. The dimensionless spin variables we will use are $\chi_i \equiv S_i/m_i^2$ and $\tilde{a}_i \equiv S_i/(m_i M)$.

[1] Note that the Q expression starts at 3PN.

The spin-spin terms contributing to the EOB Hamiltonian are known up to 4PN, which is next-to-next-to-leading order (NNLO) [223]. In `TEOBResumS`, all the spin-spin contributions are included in the centrifugal radius r_c [190], defined as

$$r_c^2 \equiv r^2 + \tilde{a}_0^2\left(1+\frac{2}{r}\right) + \frac{\delta a_{\rm NLO}^2}{r} + \frac{\delta a_{\rm NNLO}^2}{r^2}, \tag{14}$$

where $\tilde{a}_0 \equiv \tilde{a}_1 + \tilde{a}_2$ and the next-to-leading (NLO) term reads

$$\delta a_{\rm NLO}^2 = -\frac{9}{8}\tilde{a}_0^2 - \frac{1}{8}(1+4\nu)\tilde{a}_{12}^2 + \frac{5}{4}X_{12}\tilde{a}_0\tilde{a}_{12}, \tag{15}$$

with $X_{12} = \sqrt{1-4\nu}$ and $\tilde{a}_{12} \equiv \tilde{a}_1 - \tilde{a}_2$. The explicit values of the NNLO term $\delta a_{\rm NNLO}^2$ can be obtained from Ref. [223] and will again be reported in Chapter 6.

Historically, within `TEOBResumS`, the centrifugal radius is used at NLO. The newer version of the model described in Chapter 6 will use the NNLO extension, though in a factorized form.

The centrifugal radius enters the metric functions definitions [190, 224] as follows:

$$\begin{aligned} A(r;\chi_i) &= \frac{1+2u_c}{1+2u}A_{\rm orb}(r_c), \\ D(r;\chi_i) &= D_{\rm orb}(r_c), \\ B(r;\chi_i) &= \frac{r^2}{r_c^2}\frac{D(r;\chi_i)}{A(r;\chi_i)}, \end{aligned} \tag{16}$$

where we defined $u_c \equiv 1/r_c$. It also substitutes the redial separation r that appears in the effective Hamiltonian [Eq. (7)], which will read

$$\hat{H}_{\rm eff}^{\rm orb} = \sqrt{p_{r_*}^2 + A(r)\left[1 + \frac{p_\varphi^2}{r_c^2} + Q(r,p_{r_*})\right]}. \tag{17}$$

The spin-orbit contributions are instead added to the effective Hamiltonian as

$$\hat{H}_{\rm eff} = \hat{H}_{\rm eff}^{\rm orb} + p_\varphi\left(G_s\hat{S} + G_{S_*}\hat{S}_*\right), \tag{18}$$

where

$$\hat{S} \equiv \frac{S_1 + S_2}{M^2}, \tag{19}$$

$$\hat{S}_* \equiv \frac{1}{M^2}\left(\frac{m_2}{m_1}S_1 + \frac{m_1}{m_2}S_2\right). \tag{20}$$

We defined the *gyro-gravitomagnetic functions* G_S and G_{S_*}, that determine the strength of the spin-orbit coupling. We take them in Damour-Jaranowski-Schäfer (DJS) gauge [225], in which they are only functions of r and $p_{r_*}^2$ (and not p_φ). They are factorized as

$$\begin{aligned} G_S &= G_S^0\, \hat{G}_S, \\ G_{S_*} &= G_{S_*}^0\, \hat{G}_{S_*}, \end{aligned} \tag{21}$$

where

$$\begin{aligned} G_S^0 &= 2uu_c^2, \\ G_{S_*}^0 &= \frac{3}{2}u_c^3, \end{aligned} \tag{22}$$

and $(\hat{G}_S, \hat{G}_{S_*})$ are PN correcting factors known at 4.5 PN [154, 138], corresponding to (next-to)^3-leading order (N^{3}LO). In `TEOBResumS`, they are generally inverse-resummed and expressed as functions of u_c, so that they read

$$\begin{aligned} \hat{G}_S = \Big[1 &+ \left(c_{10}u_c + c_{02}p_{r_*}^2\right) + \\ &+ \left(c_{20}u_c^2 + c_{12}u_c p_{r_*}^2 + c_{04}p_{r_*}^4\right) + \\ &+ \left(c_{30}u_c^3 + c_{22}p_{r_*}^2 u_c^2 + c_{14}u_c p_{r_*}^4 + c_{06}p_{r_*}^6\right)\Big]^{-1}, \end{aligned} \tag{23}$$

$$\begin{aligned} \hat{G}_{S_*} = \Big[1 &+ \left(c_{10}^* u_c + c_{02}^* p_{r_*}^2\right) + \\ &+ \left(c_{20}^* u_c^2 + c_{12}^* u_c p_{r_*}^2 + c_{04}^* p_{r_*}^4\right) + \\ &+ \left(c_{30}^* u_c^3 + c_{22}^* p_{r_*}^2 u_c^2 + c_{14}^* u_c p_{r_*}^4 + c_{06}^* p_{r_*}^6\right) + c_{40}^* u_c^4\Big]^{-1}, \end{aligned} \tag{24}$$

where

$$
\begin{aligned}
c_{10} &= \frac{5}{16}\nu, & c^*_{10} &= \frac{3}{4}+\frac{1}{2}\nu,\\
c_{20} &= \frac{51}{8}\nu+\frac{41}{256}\nu^2, & c^*_{20} &= \frac{27}{16}+\frac{29}{4}\nu+\frac{3}{8}\nu^2,\\
c_{12} &= 12\nu-\frac{49}{128}\nu^2, & c^*_{12} &= 4+11\nu-\frac{7}{8}\nu^2,\\
c_{02} &= \frac{27}{16}\nu, & c^*_{02} &= \frac{5}{4}+\frac{3}{2}\nu,\\
c_{04} &= -\frac{5}{16}\nu+\frac{169}{256}\nu^2, & c^*_{04} &= \frac{5}{48}+\frac{25}{12}\nu+\frac{3}{8}\nu^2,
\end{aligned}
\tag{25}
$$

and the N^{3}LO coefficients are computed in Refs. [154] and will be made explicit in Chapter 6.

We can note how Eq. (24) also contains a term that would appear at (next-to)^4-leading order, c^*_{40}. In order to understand why that is, we must note that in the test-mass limit $\hat{G}_{S_*}$ does not reduce to the case of a spinning particle orbiting around a Schwarzschild BH. In fact, the circular value of $\hat{G}_{S_*}$ in the test-mass limit reads

$$
\begin{aligned}
\hat{G}^{\rm circ}_{S_*}\Big|_{\nu=0} &= \frac{2}{1+\frac{1}{\sqrt{1-3u_c}}} =\\
&= \left(1+\frac{3}{4}u_c+\frac{27}{16}u_c^2+\frac{135}{32}u_c^3+\frac{2835}{256}u_c^4+\mathcal{O}[u_c^5]\right)^{-1}.
\end{aligned}
\tag{26}
$$

Since the exact expression, in DJS gauge, had a singularity at the (r_c-corrected) light ring, it was decided to expand it in series and use its 4PN form (even when working at a lower order for the generic-masses terms).

In both versions of `TEOBResumS` discussed in this thesis (unless otherwise specified), the gyro-gravitomagnetic functions are taken at effective N^{3}LO, that is using the analytical expression at NNLO (apart from the test-mass terms coming from $\hat{G}_{S_*}$)

and adding an effective N^{3}LO coefficient, c_3, which is the second parameter fitted to NR simulations. In practice, this means expressing $\hat{G}_S$ and $\hat{G}_{S_*}$ using the coefficients of Eq. (25), with the addition of

$$c_{30} = \nu c_3, \qquad c^*_{30} = \frac{135}{32} + \nu c_3, \qquad c^*_{40} = \frac{2835}{256}. \tag{27}$$

Also in this case, the explicit value of c_3 will depend on the specific `TEOBResumS` iteration.

3.4.3 Radiation reaction and waveform

The Hamiltonian determines the conservative portion of the dynamics and will be the part we will focus on in the following Chapters. In addition to the Hamiltonian, in order to solve the complete Hamilton's equations, we need a prescription for the radiation reaction fluxes $\hat{\mathcal{F}}_\varphi$ and $\hat{\mathcal{F}}_r$.

In the quasi-circular scenario, `TEOBResumS` sets $\hat{\mathcal{F}}_r = 0$. The angular momentum flux is instead separated into two contributions. The first is the angular momentum carried away by GWs that can be measured at "infinite" distance, while the second is constituted by the GWs that enter the BH event horizons, so that

$$\hat{\mathcal{F}}_\varphi = \hat{\mathcal{F}}^\infty_\varphi + \hat{\mathcal{F}}^{\rm H}_\varphi. \tag{28}$$

The horizon flux is implemented in `TEOBResumS` using an approach first introduced in Ref. [226]. The flux at infinity is instead related to the multipolar waveform strain, which is decomposed into spherical harmonics with spin-weight $s = -2$ as

$$h_+ - {\rm i} h_\times = \sum_{\ell=2}^{\ell_{max}} \sum_{m=1}^{\ell} h_{\ell m} \, {}_{-2}Y_{\ell m}(\theta, \phi), \tag{29}$$

so that the total flux reads

$$\hat{\mathcal{F}}_\varphi^\infty = \sum_{\ell=2}^{\ell_{max}} \sum_{m=1}^{\ell} F_{\ell m} = \frac{2}{16\pi G} \sum_{\l=2}^{\ell_{max}} \sum_{m=1}^{\ell} \left| R\, \dot{h}_{\ell m} \right|^2 , \tag{30}$$

where $F_{\ell m} = F_{\ell |m|}$ is the sum of the two equal contributions related to $+m$ and $-m$.

The (ℓ, m) multipolar waveform is factorized as [227, 211, 219]

$$h_{\ell m} = h_{\ell m}^{(N,\epsilon)}\ \hat{h}_{\ell m}^{(\epsilon)} \hat{h}_{\ell m}^{\rm NQC}, \tag{31}$$

in which $\epsilon = \mathrm{mod}(\ell\ +\ m)$ denotes the parity of the multipolar waveform. $h_{\ell m}^{(N,\epsilon)}$ represents the Newtonian contribution, $\hat{h}_{\ell m}^{(\epsilon)}$ is a PN correction factor and $\hat{h}_{\ell m}^{\rm NQC}$ is a next-to-quasi-circular (NQC) term informed by NR simulations, that ensures the smooth transition between the inspiral and merger waveforms. The PN correction factor $\hat{h}_{\ell m}^{(\epsilon)}$ is built as

$$\hat{h}_{\ell m}^{(\epsilon)} = \hat{S}_{\rm eff}^{(\epsilon)}\ T_{\ell m}\ e^{{\rm i}\,\delta_{\ell m}}\ (\rho_{\ell m})^\ell, \tag{32}$$

where $\hat{S}_{\rm eff}^{(\epsilon)}$ is an effective source term and $T_{\ell m}$ is the tail factor, that takes into account the "leading logarithms" arising from the back-scattering of the propagating GWs against the background gravitational field. The residual PN series $\delta_{\ell m}$ and $\rho_{\ell m}$ are then resummed in a multipole-dependent way described in Ref. [196].

Ref. [170] introduced a first extension of `TEOBResumS` to eccentric systems, by implementing the radiation reaction fluxes along generic orbits derived in Ref. [228]. The circular Newtonian prefactor of the angular momentum flux $\hat{\mathcal{F}}_\varphi$ is corrected by a generic-orbit term as

$$\hat{\mathcal{F}}_\varphi^{\infty,{\rm N}} = \hat{\mathcal{F}}_\varphi^{\infty,{\rm N_{circ}}}\, \hat{f}_\varphi^{\rm N_{non-circ}},$$

where the explicit form of $\hat{f}_\varphi^{\rm N_{non-circ}}$ can be found in Eq. (7) of Ref. [170]. The same is done for the emitted waveform, in which the circular Newtonian prefactor $h_{\ell m}^{(N,\epsilon)}$ is replaced by its

general expression obtained computing the time-derivatives of the Newtonian mass and current multipoles. Moreover, the radial momentum flux $\hat{\mathcal{F}}_r$ is no longer considered null, but instead reads

$$\hat{\mathcal{F}}_r = \frac{32}{3} p_{r_*} u^4 P_2^0 \left[\hat{f}_r^{\rm 2PN} \right], \tag{33}$$

where the generic-orbits 2PN flux of Ref. [228] is inverse-resummed. This minimal extension of `TEOBResumS` will be the one used in Chapter 5 to generate waveforms for BBH scatterings and dynamical captures.

This generic-orbits version of `TEOBResumS` was then improved in Ref. [171], which constituted the first attempt at building a coherent model for quasi-circular, eccentric and hyperbolic systems. First, Ref. [171] proposed to multiply the generic-orbit prefactor $\hat{f}_\varphi^{\rm N_{non-circ}}$ only to the $(\ell, m) = (2, 2)$ contribution to the angular momentum flux, as in

$$\hat{\mathcal{F}}_\varphi^{\infty,{\rm N}} = \sum_{\ell=2}^{\ell_{max}} \sum_{m=1}^{\ell} \hat{\mathcal{F}}_{\ell m}^{\rm N_{circ}} \hat{f}_{\ell m}^{\rm N_{non-circ}}, \tag{34}$$

where $\hat{f}_{22}^{\rm N_{non-circ}} = \hat{f}_\varphi^{\rm N_{non-circ}}$ and $\hat{f}_{\ell m}^{\rm N_{non-circ}} = 1$ otherwise. Second, the residual 2PN correction to the radial momentum flux, $\hat{f}_r^{\rm 2PN}$, was reduced to its low-eccentricity approximation

$$\begin{aligned} \hat{f}_r^{\rm 2PN} = 1 &- \left(\frac{573}{280} + \frac{118}{35}\nu \right) u + \\ &+ \left(-\frac{33919}{2160} + \frac{6493}{560}\nu + \frac{1311}{280}\nu^2 \right) u^2, \end{aligned} \tag{35}$$

so to improve the quasi-circular behaviour of the model. Finally, the generic-orbits correction to the waveform introduced in Ref. [170] is now multiplied to a sigmoid function that progressively switches off this factor near merger and simultaneously switches on NR-informed NQC corrections. This last description of the `TEOBResumS` waveform and radiation reaction along generic orbits is the one that will be used in Chapter 6.

4 Comparing effective-one-body Hamiltonians

Parameter estimation of GW data extracts information on the masses, spins and tidal parameters of the source objects by comparing the detector data with a large number of template waveforms. Different approximants generate different waveforms and may in principle lead to discrepancies in the recovery of the binary parameters. Errors and biases due to mistakes in waveform modeling are commonly referred as waveform systematics.

EOB-based models are the most accurate semi-analytical models used in GW data analysis. Their accuracy is generally measured by using their unfaithfulness with respect to NR simulations. The 2 state-of-the art EOB-NR models for circular binaries, `TEOBResumS` [166, 196] and `SEOBNRv4` [204, 167], both deliver waveforms that are faithful to NR simulations at the 1% level (or less) [204, 166]. This threshold is considered satisfactory for current GW detectors but will need to be lowered by roughly two orders of magnitude for the next generation of detectors [229]. With improved sensitivities and higher signal-to-noise ratios (SNRs), smaller discrepancies between waveform approximants will be magnified and could induce biases in the estimated parameters. The study of waveform systematics hence becomes very important in order to understand up to which level we can trust results obtained with different theoretical models.

For EOB-based models, the systematics can lie both in the incompleteness of the analytical information used to build them and in the resummation choices made by their developers. In the following, we will focus on the modeling differences in the dynamics of the spin-aligned models `TEOBResumS` and `SEOBNRv4`.

The contents of this section were originally published as "P. Rettegno et al., *Phys. Rev. D* **101** 104027 (2020)" [230].

4.1 Hamiltonian of a spinning particle on a Kerr background

Both EOB models use as starting point the Hamiltonian of a test spinning object around a background spinning BH (described by a Kerr metric). However, the constructions of the two spinning EOB models were rooted in different ways of considering the extreme-mass-ratio ($m_2 \ll m_1$, i.e. $\nu \to 0$) limit defining the undeformed, background Kerr Hamiltonian. The `TEOBResumS` construction was initially based on Ref. [225] which considered the extreme-mass-ratio limit of a system of two spinning BHs, while the `SEOBNRv4` construction was initially based on Refs. [198, 197, 199], which considered the extreme-mass-ratio limit describing a test particle endowed with an *unlimited* spin moving in a Kerr metric. The difference between the two ways of considering the limit is that, as the spin of a small BH of mass $m_2 \ll m_1$ is physically bounded by the inequality $\chi_2 \leq 1$, i.e. $S_2 \leq m_2^2$, the former way of thinking about the limit leads to an Hamiltonian describing a non-spinning test particle around a Kerr BH. Technically, when considering the general Hamiltonian described in Eq.(57) below, the spin combination $\hat{S}_*$ defined in Eq.(53) goes to zero proportionally to ν in this way of considering the extreme-mass-ratio limit. By contrast, in the second way of considering the extreme-mass-ratio limit, in which one formally considers overspinning test objects having $\chi_2 \gg 1$, but a fixed value of $\tilde{a}_2 = S_2/(m_2 M)$, the spin combination $\hat{S}_*$ does not go to zero as $\nu \to 0$. This motivated Ref.[197, 199] to pay particular attention to the part of the spin-orbit sector linked to the coupling of $\hat{S}_*$, i.e. to the second gyro-gravitomagnetic factor G_{S_*} in Eq.(73) below. On the other hand, the construction of the `TEOBResumS` model paid particular attention to the first gyro-gravitomagnetic factor G_S, and, following the construction of the first spinning EOB model [27], to ways of incorporating

spin-spin effects through the definition of a suitable background Kerr spin variable $\tilde{a}_0$ (see below).

In this section, we indicate with M the mass of the Kerr BH and with μ the mass of the particle. Their spins are addressed as $S_{\rm Kerr}$ and S_* respectively, with dimensionless spin variables that read $\hat{a} \equiv S_{\rm Kerr}/M^2$ and $\tilde{a}_* \equiv S_*/(\mu M)$. We restrict ourselves to equatorial orbits ($\theta = \pi/2$) and parallel spins, using dimensionless phase space variables.

The Kerr metric in Boyer-Lindquist coordinates and restricted to the equatorial plane reads

$$\begin{aligned} ds^2 = &- \frac{\Lambda}{\Delta^K \Sigma} dt^2 + \frac{\Delta^K}{\Sigma} dr^2 \\ &+ \frac{1}{\Lambda}\left(-\frac{4r^2\hat{a}^2}{\Delta^K\Sigma} + \Sigma\right) d\varphi^2 - \frac{2r\hat{a}}{\Delta^K\Sigma} dt d\varphi, \end{aligned} \tag{36}$$

where

$$\Sigma \equiv r^2, \tag{37}$$

$$\Delta^K \equiv r^2\left(1 - \frac{2}{r}\right) + \hat{a}^2, \tag{38}$$

$$\Lambda \equiv (r^2 + \hat{a}^2)^2 - \hat{a}^2 \Delta^K. \tag{39}$$

From the relativistic mass-shell condition $g^{\mu\nu} p_\mu p_\nu = -1$, one obtains the Hamiltonian of a non-spinning particle on a Kerr background, $\hat{H}_0^K \equiv -p_0$, as

$$\hat{H}_0^K = \alpha \sqrt{1 + \gamma^{ij}\, p_i\, p_j} + \beta^i\, p_i, \tag{40}$$

with standard lapse-shift decomposition of the metric

$$\alpha = \frac{1}{\sqrt{-g^{tt}}}, \tag{41}$$

$$\beta^i = \frac{g^{ti}}{g^{tt}}, \tag{42}$$

$$\gamma^{ij} = g^{ij} - \frac{g^{ti} g^{tj}}{g^{tt}}. \tag{43}$$

The same Hamiltonian can be written equivalently as

$$\hat{H}_0^K = \sqrt{A^K \left(1 + \frac{p_\varphi^2}{(r_c^K)^2} + \frac{p_r^2}{B^K}\right)} + G_S^K \hat{a}\, p_\varphi, \tag{44}$$

where we introduced the centrifugal radius

$$\left(r_c^K\right)^2 = \frac{\Lambda}{\Sigma} = \frac{(r^2+\hat{a}^2)^2 - \hat{a}^2\Delta^K}{r^2} = r^2 + \hat{a}^2\left(1+\frac{2}{r}\right), \tag{45}$$

and the functions (A^K, B^K, r_c^K, G_S^K) are expressed in terms of the Kerr metric functions as

$$A^K = \frac{\Delta^K \Sigma}{\Lambda} = \left(1 - 2u_c^K\right)\frac{1+2u_c^K}{1+2u}, \tag{46}$$

$$B^K = \frac{\Sigma}{\Delta^K} = \frac{(u_c^K)^2}{u^2}\frac{1}{A^K}, \tag{47}$$

$$G_S^K = \frac{2r\hat{a}}{\Lambda} = 2\,u\,(u_c^K)^2, \tag{48}$$

where $u_c^K \equiv 1/r_c^K$. These two different formulations of the Kerr Hamiltonian are at the core of the differences between the two EOB-NR models dynamics. We will expand our discussion on this topic in the following sections.

When we consider a (over)spinning particle, an additional spin-orbit coupling term $G_{S_*}^K \tilde{a}_* p_\varphi$ is present, so that the Kerr Hamiltonian in the extreme mass-ratio limit [198, 190] reads

$$\hat{H}^K = \sqrt{A^K \left(1 + \frac{p_\varphi^2}{(r_c^K)^2} + \frac{p_r^2}{B^K}\right)} + \left(G_S^K \hat{a} + G_{S_*}^K \tilde{a}_*\right) p_\varphi. \tag{49}$$

The expression of $G_{S_*}^K$ is not trivial (see Ref. [197]). The re-derivation of Ref. [231] showed that for the equatorial, parallel-

spin, case it can be written as (see Eq. (2.21) therein)

$$G_{S_*}^K = \frac{1}{\left(r_c^K\right)^2}\Bigg\{ \frac{\sqrt{A^K}}{\sqrt{Q^K}}\left[1 - \frac{\left(r_c^K\right)'}{\sqrt{B^K}}\right] + \\ + \frac{r_c^K}{2\left(1+\sqrt{Q^K}\right)}\frac{\left(A^K\right)'}{\sqrt{A^K B^K}}\Bigg\}, \tag{50}$$

where the radial derivatives are indicated as $(\cdot)' \equiv \partial_r(\cdot)$ and

$$\begin{aligned} Q^K &\equiv 1 + \gamma^{ij}\, p_i\, p_j \\ &= 1 + p_\varphi^2 (u_c^K)^2 + \frac{p_r^2}{B^K}. \end{aligned} \tag{51}$$

One can check that Eq. (50) is consistent with Eq. (3.18) Ref. [197] once specified to equatorial orbits.

4.2 The Hamiltonian of `TEOBResumS`

In the following, we will consider a binary system with masses m_i and spin vectors $\boldsymbol{S_i}$, with $i = 1, 2$. The projections of the spins along the direction of the orbital angular momentum are denoted by $S_i \equiv \boldsymbol{L}\cdot\boldsymbol{S_i}$. We denote the total mass by $M \equiv m_1 + m_2$ and the reduced mass as $\mu \equiv (m_1 m_2)/M$. We adopt the convention that $m_1 \geq m_2$. We hence define the mass ratio $q = m_1/m_2 \geq 1$ and symmetric mass ratio $\nu \equiv \mu/M = (m_1 m_2)/(m_1+m_2)^2$. The mass fractions are expressed as $X_i \equiv m_i/M$. The dimensionless spin variables we use are $\chi_i \equiv S_i/m_i^2$ and $\tilde{a}_i \equiv S_i/(m_i M) = X_i\chi_i$, together with their combinations

$$\hat{S} \equiv \frac{S_1 + S_2}{M^2}, \tag{52}$$

$$\hat{S}_* \equiv \frac{1}{M^2}\left(\frac{m_2}{m_1}S_1 + \frac{m_1}{m_2}S_2\right), \tag{53}$$

and

$$\tilde{a}_0 \equiv \tilde{a}_1 + \tilde{a}_2 = \hat{S} + \hat{S}_*, \tag{54}$$

$$\tilde{a}_{12} \equiv \tilde{a}_1 - \tilde{a}_2 = \frac{\hat{S} - \hat{S}_*}{X_{12}}, \tag{55}$$

where $X_{12} \equiv X_1 - X_2$. Like the case of a spinning particle on Kerr seen above, for spin-aligned binaries the four-dimensional phase space is described by $(\varphi, P_\varphi, R, P_{r_*})$ where φ is the orbital phase, P_φ the orbital angular momentum, R the radial separation and $P_{R_*} \equiv \sqrt{A/B} P_R$ the conjugate radial momentum with respect to the tortoise radial coordinate. Dimensionless phase space variables are $r \equiv R/M$, $p_{r_*} \equiv P_{r_*}/\mu$ and $p_\varphi \equiv P_\varphi/(\mu M)$, while dimensionless time is denoted as $t \equiv T/M$.

The `TEOBResumS` model [166] stems from the (equatorial) Hamiltonian introduced in Ref. [190]. An important element of the latter is the centrifugal radius that is used to incorporate, in a resummed way, spin-spin effects within the Hamiltonian. The EOB Hamiltonian reads

$$\hat{H}_{\rm EOB} \equiv \frac{H_{\rm EOB}}{\mu} = \frac{1}{\nu}\sqrt{1 + 2\nu\left(\hat{H}_{\rm eff} - 1\right)}. \tag{56}$$

The effective Hamiltonian $\hat{H}_{\rm eff} \equiv H_{\rm eff}/\mu$ is constructed so as to closely mimic the structure of the (spinning) test-particle one described in Eq. (49) and is written as

$$\hat{H}_{\rm eff} = \hat{H}^{\rm orb}_{\rm eff} + \left(G_S \hat{S} + G_{S_*} \hat{S}_*\right) p_\varphi, \tag{57}$$

where $\hat{S}$ and $\hat{S}_*$ reduce to the spin of the primary object and of the particle respectively when $m_1 \gg m_2$.

4.2.1 Orbital Hamiltonian

The orbital effective Hamiltonian in Eq. (57) reads

$$\hat{H}^{\rm eff}_{\rm orb} = \sqrt{A\left(1 + \frac{p^2_\varphi}{r^2_c} + 2\nu(4 - 3\nu)\frac{p^4_{r_*}}{r^2_c}\right) + p^2_{r_*}}, \tag{58}$$

where r_c is the EOB centrifugal radius that takes into account spin-spin interactions (see below) and the A function is written as

$$A = A_{\rm orb}\left(u_c\right)\frac{1+2u_c}{1+2u}, \tag{59}$$

where

$$A_{\rm orb}\left(u_c\right) = P^1_5\left[A^{\rm 5PN}_{\rm orb}\right]\left(u_c\right), \tag{60}$$

is the orbital potential resummed with a $(1,5)$ Padé approximant. The PN expanded orbital potential, at 5PN formal accuracy, reads

$$\begin{aligned} A^{\rm PN}_{\rm orb}(u) = 1 - 2u + 2\nu u^3 + \left(\frac{94}{3} - \frac{41\pi^2}{32}\right)\nu u^4 + \\ + \left(a^c_5 + a^{\log}_5 \log u\right) u^5 + \nu\left(a^c_6 + a^{\log}_6 \log u\right) u^6. \end{aligned} \tag{61}$$

The 4PN and the logarithmic 5PN term are analytically known,

$$\begin{aligned} a^c_5 &= \left(\frac{2275\pi^2}{512} - \frac{4237}{60} + \frac{128}{5}\gamma_{\rm E} + \frac{256}{5}\log 2\right)\nu + \\ &\quad + \left(\frac{41\pi^2}{32} - \frac{221}{6}\right)\nu^2, \\ a^{\log}_5 &= \frac{64}{5}\nu, \\ a^{\log}_6 &= -\frac{7004}{105}\nu - \frac{144}{5}\nu^2, \end{aligned} \tag{62}$$

where $\gamma_{\rm E} = 0.57721\ldots$ is Euler's constant and the (effective) 5PN term a^c_6 is informed by NR simulations [191, 192, 166] (see Sec. 4.2.3 below).

All terms proportional to even powers of the spins are incorporated in the EOB centrifugal radius r_c. This function is understood as a *deformation* of the Kerr one, Eq. (45), which reads

$$r_c^2 \equiv r^2 + \tilde{a}_0^2\left(1 + \frac{2}{r}\right) + \frac{\delta a^2}{r}, \tag{63}$$

where the dimensionless Kerr spin is replaced by the dimensionless effective spin $\tilde{a}_0$. The function $\delta\tilde{a}^2$ is introduced here to incorporate spin-spin terms beyond LO. The BBH sector of `TEOBResumS` only includes next-to-leading order (NLO) spin-spin terms, so that this function explicitly reads [194]

$$\delta a^2 \equiv -\frac{1}{8}\left\{9\,\tilde{a}_0^2 + (1+4\nu)\,\tilde{a}_{12}^2 - 10X_{12}\,\tilde{a}_0\,\tilde{a}_{12}\right\}. \tag{64}$$

The other metric potential B is obtained through the D function, whose PN expression is

$$D_{\rm orb}^{\rm PN}(u) = 1 - 6\nu u^2 - 2\,(26-3\nu)\,\nu u^3. \tag{65}$$

Within `TEOBResumS`, this is resummed as

$$D \equiv AB = \frac{r^2}{r_c^2} D_{\rm orb}(u_c), \tag{66}$$

with

$$D_{\rm orb}\,(u_c) = P_3^0\left[D_{\rm orb}^{\rm 5PN}\right](u_c) \tag{67}$$

being the inverse resummation of its PN series.

4.2.2 Spin-orbit Hamiltonian

The spin-orbit contributions are encoded into the gyro-gravitomagnetic functions (G_S, G_{S_*}) of Eq. (49). In `TEOBResumS` they are written in factorized form

$$G_S = G_S^0\;\hat{G}_S, \tag{68}$$

$$G_{S_*} = G_{S_*}^0 \hat{G}_{S_*}, \tag{69}$$

where

$$G_S^0 = 2uu_c^2 \tag{70}$$

is the Kerr spin orbit coupling structure, in which r_c^K is replaced by the one defined in Eq. (63) above. $G^0_{S_*}$ is the leading PN correction (that can be also obtained by Taylor-expanding Eq. (50)) where u is replaced by u_c and reads

$$G^0_{S_*} = \frac{3}{2} u_c^3. \tag{71}$$

In this respect, one should be reminded that Ref. [190] chose, for simplicity, to only use *part of* the analytical information encoded into the Hamiltonian of a spinning particle, Eq. (50), i.e. restricting it to the case of a Schwarzschild background and expanding it up to (next-to)^3-leading order (N^{3}LO). We stress this was a choice prompted both by the desire of constructing a rather simple model using the Damour-Jaranowski-Schäfer (DJS) gauge [225], where all dependence on the angular momentum p_φ is removed from (G_S, G_{S_*}), and by the idea that, in the physically relevant case of BBH systems, the G_{S_*}-type coupling is always secondary with respect to the G_S-type one because it contains an extra factor ν (with $\nu \leq 1/4$ in all cases). In the DJS gauge [2], the Hamiltonian of a spinning particle (either Schwarzschild or Kerr) becomes singular at light ring. So, the only way of incorporating some of this analytical information is by PN-expanding the corresponding G_{S_*}, that is then eventually resummed after in a different way. Note however that the *full* spinning-particle information can be incorporated also in a special flavor of `TEOBResumS`, notably in factorized form. To do so, however, a different spin gauge should be chosen.

Finally, $\hat{G}_S$ and $\hat{G}_{S_*}$ are PN correcting factors that in `TEOBResumS`

[2]The DJS gauge has the disadvantage of introducing formal (and fictitious [232]) singularities at the light ring, but it has many other useful properties: (i) it minimizes the effect of non-circularities during the late inspiral and the premerger phase; (ii) it allows, in principle, a clean separation between spin-orbit (odd in spin) and spin-spin (even in spin) effects.

are inverse-resummed as

$$\hat{G}_S = \big(1 + c_{10}u_c + c_{20}u_c^2 + c_{30}u_c^3 + c_{02}p_{r_*}^2 + \\ + c_{12}u_c p_{r_*}^2 + c_{04}p_{r_*}^4\big)^{-1}, \tag{72}$$

$$\hat{G}_{S_*} = \big(1 + c_{10}^* u_c + c_{20}^* u_c^2 + c_{30}^* u_c^3 + c_{40}^* u_c^4 + c_{02}^* p_{r_*}^2 + \\ + c_{12}^* u_c p_{r_*}^2 + c_{04}^* p_{r_*}^4\big)^{-1}. \tag{73}$$

All coefficients are fully known analytically, with their complete ν dependence, except for (c_{30}^*, c_{40}^*), which are those corresponding to the PN expansion of the spin-orbit sector of the Hamiltonian of a spinning particle on a Schwarzschild background [190]. In addition, the ν-dependence of c_{30} and c_{30}^* is informed by NR simulations. More precisely, we use $c_{30} \equiv \nu c_3$ and $c_{30}^* = 135/32 + \nu c_3$, where $135/32$ is the spinning-particle value and c_3 is an NR-tuned effective N^{3}LO parameter. The numerical values of the other coefficients in the DJS gauge are listed in Appendix B of Ref. [230].

4.2.3 Numerical-relativity informed functions

The dynamics of `TEOBResumS` depends on two free functions (or flexibility parameters), a_6^c and c_3, that are determined by comparison with NR simulations. The orbital Hamiltonian is NR-informed through a_6^c, that explicitly reads [191, 192, 166]

$$a_6^c = 3097.3\ \nu^2 - 1330.6\ \nu + 81.38\,. \tag{74}$$

The spin-orbit sector is instead calibrated using

$$c_3 = p_0 \frac{1 + n_1\tilde{a}_0 + n_2\tilde{a}_0^2}{1 + d_1\tilde{a}_0} + \\ + \big(p_1\nu + p_2\nu^2 + p_3\nu^3\big)\tilde{a}_0 X_{12} + p_4\tilde{a}_{12}\nu^2, \tag{75}$$

with [3]

$$
\begin{aligned}
p_0 &= 43.371638, & p_1 &= 929.579,\\
n_1 &= -1.174839, & p_2 &= -9178.87,\\
n_2 &= 0.354064, & p_3 &= 23632.3,\\
d_1 &= -0.151961, & p_4 &= -104.891.
\end{aligned} \tag{76}
$$

Similar to what will be seen to occur also for `SEOBNRv4`, the spin-dependence of the NR-informed parameters violates the clear distinction between spin-orbit and spin-spin Hamiltonians. In this case, c_3 introduces even-in-spin terms in $G_{S_*}\hat{S}_*$.

4.3 The Hamiltonian of `SEOBNRv4`

The Hamiltonian used in the `SEOBNRv4` [204] model was structurally introduced in Ref. [197] for the case of generally oriented spins. In order to compare it to the `TEOBResumS` one, here we only focus on the spin-aligned case (the generic scenario is discussed in Appendix A of Ref. [230].

The `SEOBNRv4` Hamiltonian is obtained as the result of a certain deformation of the Hamiltonian of a spinning particle on a Kerr background. First, the dimensionless BH spin $\hat{a}$ is replaced by the effective spin $\hat{S}$ (instead of $\tilde{a}_0 = \hat{S} + \hat{S}_*$ used in `TEOBResumS`). Second, the functions $(\Delta^K, \Sigma, \Lambda)$ entering the Kerr metric, Eq. (36), are deformed by adding ν-dependent PN information. These functions are resummed so as to obtain a robust behavior in the strong-field regime. Finally, one adds to the latter Hamiltonian additional terms that are obtained by similarly deforming the spin-orbit coupling function of a spinning particle on a Kerr BH.

We now denote the EOB Hamiltonian as

$$
\hat{H}_{\rm EOB} \equiv \frac{1}{\nu}\sqrt{1 + 2\nu\left(\hat{H}^{\rm SEOB}_{\rm eff} - 1\right)}, \tag{77}
$$

[3] In the equal-mass case, since the last term is not symmetric under the exchange of χ_1 and χ_2, c_3 is computed adopting the convention $|\chi_1| > |\chi_2|$.

with $\hat{H}^{\rm SEOB}_{\rm eff}$ replacing the generic $\hat{H}_{\rm eff}$ of Eq. (56) and where, following Refs. [197, 199], we define the effective EOB Hamiltonian as

$$\hat{H}^{\rm SEOB}_{\rm eff} = \hat{H}_{\rm NS} + \hat{H}_{\rm SO} + \hat{H}^{\rm eff}_{\rm SS}. \tag{78}$$

Here, $\hat{H}_{\rm NS}$ denotes the (deformed) Hamiltonian of a non-spinning particle; $\hat{H}_{\rm SO}$ indicates the ν-deformed spin-orbit coupling of the spinning particle and $\hat{H}^{\rm eff}_{\rm SS}$ refers to an additional spin-spin contribution. In this respect one has to be aware that *part of* the spin-orbit and spin-spin interaction is also incorporated in $\hat{H}_{\rm NS}$, as it is inherited by the structure of the Hamiltonian of a test-particle moving in a Kerr metric.

The aim of this section is to illustrate that it is possible to recast the spin-aligned Hamiltonian of `SEOBNRv4` in a way that is formally close to the one of `TEOBResumS` as defined in Eq. (57), modulo the additional spin-spin contribution. The final result will be an expression of the form

$$\hat{H}^{\rm SEOB}_{\rm eff} = \hat{\mathbb{H}}^{\rm eff}_{\rm orb} + \left(\bar{G}_S \hat{S} + \bar{G}_{S_*} \hat{S}_*\right) p_\varphi + \hat{H}^{\rm eff}_{\rm SS} \ , \tag{79}$$

where: (i) the orbital Hamiltonian $\hat{\mathbb{H}}^{\rm eff}_{\rm orb}$ is formally analogous to $\hat{H}^{\rm eff}_{\rm orb}$, although the metric functions and the centrifugal radius are replaced by different analytical expressions; (ii) similarly, the spin-orbit sector (i.e., odd-in-spins) will resemble the `TEOBResumS` one, with the gyro-gravitomagnetic functions $(\bar{G}_S, \bar{G}_{S_*})$ replacing (G_S, G_{S_*}) being different both in the gauge choice and the resummation approach. By contrast, the even-in-spin terms, that in `TEOBResumS` are entirely contained in $\hat{H}^{\rm eff}_{\rm orb}$, are partly incorporated within $\mathbb{H}^{\rm eff}_{\rm orb}$ and partly in $\hat{H}^{\rm eff}_{\rm SS}$, as detailed below.

4.3.1 Rewriting of $\hat{H}_{\rm NS}$: the centrifugal radius $\bar{r}_c$

Following Ref. [197], $\hat{H}_{\rm NS}$ is written following the structure of Eq. (44) and reads

$$\hat{H}_{\rm NS} = \alpha \sqrt{1 + \gamma^{ij}\, p_i\, p_j + Q_4(p)} + \beta^i\, p_i, \tag{80}$$

where $Q_4(p)$ is a PN term quartic in the momenta that will be defined below and vanishes in the Kerr limit. The functions $(\alpha, \beta_i, \gamma^{ij})$ have the same structure of Eqs. (41)–(43), but different explicit form, since the components of the ν-deformed metric introduced in Ref. [199], for equatorial orbits, are

$$g^{tt} = -\frac{\Lambda_t}{\Delta_t \Sigma}, \tag{81}$$

$$g^{rr} = \frac{\Delta_r}{\Sigma}, \tag{82}$$

$$g^{\theta\theta} = \frac{1}{\Sigma}, \tag{83}$$

$$g^{\varphi\varphi} = \frac{1}{\Lambda_t}\left(-\frac{\widetilde{\omega}_{fd}^2}{\Delta_t \Sigma} + \Sigma\right), \tag{84}$$

$$g^{t\varphi} = -\frac{\widetilde{\omega}_{fd}}{\Delta_t \Sigma}, \tag{85}$$

where

$$\Delta_t = r^2\, \Delta_u, \tag{86}$$

$$\Delta_r = \Delta_t\, \mathbb{D}^{-1}, \tag{87}$$

$$\Lambda_t = \left(r^2 + \hat{S}^2\right)^2 - \hat{S}^2 \Delta_t, \tag{88}$$

$$\Sigma = r^2, \tag{89}$$

$$\widetilde{\omega}_{fd} = 2\, \hat{S}\, r, \tag{90}$$

which mimic the Kerr functions[4] and the Kerr BH spin $\hat{a}$ is replaced by the effective spin $\hat{S}$. Note that the function Δ^K appears in both the g^{tt} and the g^{rr} components of the Kerr metric. This implies that, in Kerr, Δ^K is also part of the B

[4]In general, $\widetilde{\omega}_{fd}$ reads

$$\widetilde{\omega}_{fd} = 2\, \hat{S}\, r + \nu\, \omega_{fd}^0\, \hat{S} + \nu\, \omega_{fd}^1\, \hat{S}\, r. \tag{91}$$

With respect to Eq. (36) of Ref. [199], we already gauge-fixed the two frame-dragging parameters to zero, i.e. $\omega_{fd}^0 = \omega_{fd}^1 = 0$.

function. In EOB models the connection between the metric potentials is more complicated because of the presence of the D function. Hence, Δ^K was replaced by Δ_t in the g^{tt} metric component and by Δ_r that appears in g^{rr}. The ν-deformation is implemented as follows. At 4PN accuracy, we define the function

$$\Delta_t^{\rm 4PN} \equiv r^2 A_{\rm orb}^{\rm 4PN}(u) + \hat{S}^2, \tag{92}$$

where the terms $1-2u$ appearing in the Kerr function Δ^K is replaced by the PN-expanded EOB orbital potential at 4PN accuracy, as obtained from Eq. (61) dropping the 5PN, effective, correction. In `SEOBNRv4`, the resummation procedure is implemented on the Δ_u function, that at 4PN reads

$$\Delta_u^{\rm 4PN} \equiv u^2 \Delta_t^{\rm 4PN} = A_{\rm orb}^{\rm 4PN}(u) + u^2 \hat{S}^2. \tag{93}$$

Two Kerr-like horizons $u_\pm$ are imposed and the residual function is then resummed using a global logarithmic function as

$$\begin{aligned}\Delta_u = \hat{S}^2 \left(u-u_+\right)\left(u-u_-\right) \times \\ \times \left[1 + \nu\Delta_0 + \log\left(1 + \sum_{i=1}^{5} \Delta_i u^i\right)\right].\end{aligned} \tag{94}$$

Here (Δ_0, Δ_i) are ν-dependent coefficients that are obtained imposing that the PN-expansion of Eq. (94) coincides with the one of Eq. (93), see Ref. [200]. The two horizons are placed at

$$r_\pm \equiv \frac{1}{u_\pm} = \left(1 \pm \sqrt{1-\hat{S}^2}\right)(1 - K\nu), \tag{95}$$

where K is a free parameter in the model that is calibrated to NR simulations [204]. Note that also that the various functions (Δ_0, Δ_i) depend on this parameter and can be found in Appendix A of Ref. [206]. We also list them for completeness in our Appendix C of Ref. [230].

Finally, the D function is also resummed using a global overall logarithm instead of the Padé approximant used in `TEOBResumS`. It reads

$$\mathbb{D} = \left[1 + \log\left(1 + 6\nu u^2 + 2\left(26 - 3\nu\right)\nu u^3\right)\right]^{-1}. \tag{96}$$

We can then rewrite Eq. (80) in the following form

$$\hat{H}_{\rm NS} = \hat{\mathbb{H}}^{\rm eff}_{\rm orb} + \bar{G}^0_S\, \hat{S}\, p_\varphi, \tag{97}$$

in which we defined the Kerr-like gyro-gravitomagnetic function $\bar{G}^0_S$ as

$$\bar{G}^0_S \equiv \frac{\tilde{\omega}_{fd}}{\Lambda_t \hat{S}} = 2\, u\, \bar{u}_c^2. \tag{98}$$

Moreover, the effective *orbital* Hamiltonian $\hat{\mathbb{H}}^{\rm eff}_{\rm orb}$ reads

$$\hat{\mathbb{H}}^{\rm eff}_{\rm orb} = \sqrt{\mathbb{A}\left(1 + p_\varphi^2 \bar{u}_c^2 + 2\nu(4-3\nu)\, u^2 \bar{p}^4_{r_*}\right) + \bar{p}^2_{r_*}}, \tag{99}$$

where we expanded $Q_4(p) \equiv 2\nu(4-3\nu)u^2\bar{p}^4_{r_*}$ and we now define the momentum conjugate to the tortoise radial coordinate as $\bar{p}_{r_*} \equiv \sqrt{\mathbb{A}/\mathbb{B}}\; p_r$. The functions $(\mathbb{A}, \mathbb{B}, \mathbb{Q})$ are expressed in terms of the ν-deformed metric functions as

$$\mathbb{A} \equiv \frac{\Delta_t \Sigma}{\Lambda_t} = \frac{\bar{u}_c^2}{u^2}\Delta_u, \tag{100}$$

$$\mathbb{B} \equiv \frac{\Sigma}{\Delta_r} = \frac{\mathbb{D}}{\Delta_u}, \tag{101}$$

$$\mathbb{Q} \equiv 1 + \gamma^{ij}\, p_i\, p_j = 1 + p_\varphi^2 \bar{u}_c^2 + \frac{\bar{p}^2_{r_*}}{\mathbb{A}}. \tag{102}$$

The functions $(\mathbb{A}, \mathbb{B}, \mathbb{D}, \mathbb{Q})$ are analogous to (A, B, D, Q) used within `TEOBResumS` and, although different, they reduce to the same corresponding Kerr functions in the $\nu \to 0$ limit. In Eq. (99) we also introduced $\bar{u}_c \equiv 1/\bar{r}_c$, where $\bar{r}_c$ is a *new* centrifugal radius. This function is a ν-deformation of the Kerr r^K_c,

but differs from the `TEOBResumS` one, r_c, and explicitly reads

$$\bar{r}_c^2 \equiv \frac{\Lambda_t}{\Sigma} = \frac{(r^2+\hat{S}^2)^2}{r^2} - \hat{S}^2\Delta_u. \tag{103}$$

Writing an *orbital* Hamiltonian for `SEOBNRv4`, $\hat{\mathbb{H}}^{\rm eff}_{\rm orb}$, that mimics $\hat{H}^{\rm eff}_{\rm orb}$ makes it clearer where the differences between the models arise, though the two expressions look formally the same. The functions (A, r_c) and $(\mathbb{A}, \bar{r}_c)$ are different from one another, even if they correctly reproduce the corresponding Kerr functions when $\nu \to 0$. To understand how this is possible, let us go back to the definitions of the centrifugal radius r_c^K and of the potential A^K for the Kerr metric, Eqs. (45) and (46) respectively. These can be written in two, analytically equivalent, forms, namely

$$\left[r_c^K\right]^2 \equiv \frac{(r^2+\hat{a}^2)^2}{r^2} - \hat{a}^2\Delta^K \tag{104a}$$

$$= r^2 + \hat{a}^2\left(1+\frac{2}{r}\right), \tag{104b}$$

and

$$A^K \equiv \frac{\left(u_c^K\right)^2}{u^2}\Delta^K \tag{105a}$$

$$= \left(1-2u_c^K\right)\frac{1+2u_c^K}{1+2u}. \tag{105b}$$

In `SEOBNRv4` one obtains $\bar{r}_c$ and $\mathbb{A}$ using Eqs. (104a) and (105a), without expanding the expression of Δ^K, and then substituting $\hat{a} \to \hat{S}$ and $\Delta^K \to \Delta_u$. On the other hand, in `TEOBResumS` r_c and A are obtained through Eqs. (104b) and (105b), where the expressions have been simplified and bear no memory of the original function Δ^K that appears in the Kerr metric. Then, one substitutes $\hat{a} \to \tilde{a}_0$ and $(1-2u_c^K) \to A_{\rm orb}$. In conclusion, as well as different spin variable and resummation choices, $\bar{r}_c$ differs from r_c because it contains includes additional ν-dependent

corrections that come from Δ_u. Hence, although the two function share the same $\nu = 0$ limit, the spin-square contributions that they incorporate differ already at linear order in ν.

4.3.2 $\hat{H}_{\rm SO}$ and the spin-orbit sector

Let us turn now to rewriting $\hat{H}_{\rm SO}$ using a different notation consistent with the orbital part. Our starting point is $\hat{H}_{\rm SO}$ as given by Eq. (4.18) of Ref. [197] (and re-written in Appendix A of Ref. [230]). Once restricted to spin-aligned systems, this gives [5]

$$\hat{H}_{\rm SO} = \frac{e^{2\tilde{\nu}-\tilde{\mu}}}{\widetilde{B}^2\sqrt{\mathbb{Q}}}\left\{e^{\tilde{\mu}+\tilde{\nu}} - \tilde{J}\widetilde{B}\,' + \frac{1+2\sqrt{\mathbb{Q}}}{1+\sqrt{\mathbb{Q}}}\tilde{J}\widetilde{B}\,\tilde{\nu}\,'\right\}p_\varphi \hat{\mathbb{S}}_*, \tag{106}$$

where the functions of Ref. [199] are connected to the metric ones as

$$e^{2\tilde{\mu}} = \ \Sigma \ = r^2, \qquad e^{2\tilde{\nu}} = \frac{\Delta_t \Sigma}{\Lambda_t} = \mathbb{A}, \tag{107}$$

$$\widetilde{B} = \sqrt{\Delta_t} = \sqrt{\mathbb{A}}\,\bar{r}_c, \qquad \tilde{J} = \sqrt{\Delta_r} = \frac{r}{\sqrt{\mathbb{B}}}, \tag{108}$$

and the prime indicates derivative with respect to r. In addition, the ν-dependent PN results for the spin-orbit coupling functions are included in Eq. (106) through a (gauge-dependent) mapping [199] between the spin variables that naturally enter the PN-expanded effective Hamiltonian, $(\hat{S}, \hat{S}_*)$, that are used in `TEOBResumS`, and the effective spin variables $(\hat{\mathbb{S}}, \hat{\mathbb{S}}_*)$ that appear in `SEOBNRv4`. These spin quantities are intended to be the spin of an effective particle, $\hat{\mathbb{S}}_*$, moving around an effective Kerr BH whose spin is $\hat{\mathbb{S}}$. Following Ref. [199], such spin mapping is

[5] Note that our notation differs from Ref. [199]. We define their ν as $\tilde{\nu}$, not to confuse it with the symmetric mass ratio. Also, we use explicitly $\widetilde{B}_r = \widetilde{B}\,' - \widetilde{B}/\tilde{J}$ and $\mu_r = \mu\,' - 1/\tilde{J}$.

defined as

$$\hat{\mathbb{S}} = \hat{S} + \frac{1}{c^2}\Delta_\sigma^{(1)} + \frac{1}{c^4}\Delta_\sigma^{(2)}, \tag{109}$$

$$\hat{\mathbb{S}}_* = \hat{S}_* + \frac{1}{c^2}\Delta_{\sigma^*}^{(1)} + \frac{1}{c^4}\Delta_{\sigma^*}^{(2)} + \frac{1}{c^6}\Delta_{\sigma^*}^{(3)}, \tag{110}$$

where the functions $(\Delta_\sigma^{(i)}, \Delta_{\sigma^*}^{(i)})$ are gauge-dependent function that are chosen so to incorporate the high-order ν-dependent PN information. Ref. [199] fixes the gauge imposing that $\Delta_\sigma^{(1)} = \Delta_\sigma^{(2)} = 0$, so that

$$\hat{\mathbb{S}} \equiv \hat{S}. \tag{111}$$

On the other hand, the functions $\Delta_{\sigma^*}^{(1)}$ and $\Delta_{\sigma^*}^{(2)}$ are fixed in such a way that, once the SEOB Hamiltonian is PN-expanded, the spin-orbit PN contributions up to NNLO are correctly recovered. Moreover, the spin-orbit sector is NR-informed by an additional N^{3}LO effective correction of the form

$$\Delta_{\sigma^*}^{(3)} = \frac{d_{\rm SO}\,\nu}{r^3}\hat{S}, \tag{112}$$

whose explicit expression can be found below.

Using the definitions of Eqs. (107) and (108), $\hat{H}_{\rm SO}$ can be rewritten as

$$\hat{H}_{\rm SO} = \mathbb{G}_{\mathbb{S}_*}\, p_\varphi\, \hat{\mathbb{S}}_*, \tag{113}$$

where we defined

$$\mathbb{G}_{\mathbb{S}_*} \equiv \frac{1}{(\bar{r}_c)^2}\left\{\frac{\sqrt{\mathbb{A}}}{\sqrt{\mathbb{Q}}}\left[1 - \frac{(\bar{r}_c)'}{\sqrt{\mathbb{B}}}\right] + \frac{\bar{r}_c}{2\left(1+\sqrt{\mathbb{Q}}\right)}\frac{\mathbb{A}'}{\sqrt{\mathbb{A}\mathbb{B}}}\right\}, \tag{114}$$

that formally coincides with Eq. (50), having replaced the Kerr functions (A^K, B^K, Q^K, r_c^K) with $(\mathbb{A}, \mathbb{B}, \mathbb{Q}, \bar{r}_c)$.

We found it convenient to write the complete spin-orbit content of `SEOBNRv4` in a form that is close to the one of `TEOBResumS`, so to similarly define two gyro-gravitomagnetic functions. To do so, we define the complete spin-orbit sector of $\hat{H}_{\rm eff}^{\rm SEOB}$ as

$$\hat{\mathbb{H}}_{\rm SO} = \left(\bar{G}_S^0 \hat{S} + \mathbb{G}_{\mathbb{S}_*}\hat{\mathbb{S}}_*\right) p_\varphi. \tag{115}$$

Since $\hat{\mathbb{S}}_*$ is a linear combination of $(\hat{S}, \hat{S}_*)$, one sees that the above function can be written precisely as the corresponding function in `TEOBResumS`, though the gyro-gravitomagnetic functions will eventually be different. We see that the $\Delta^{(i)}_{\sigma^*}$ that appear in Eq. (110) are functions of (r, p_{r_*}, p_φ), with some additional gauge-freedom that can be fixed at will (see below). These latter formally read

$$\Delta^{(1)}_{\sigma^*} = c_u u + c_{\mathbb{Q}}\left(\mathbb{Q}-1\right) + c_{p_r^2}\frac{p_r^2}{\mathbb{B}}, \tag{116}$$

$$\Delta^{(2)}_{\sigma^*} = c_{u^2}\, u^2 + c_{\mathbb{Q}^2}\left(\mathbb{Q}-1\right)^2 + c_{u\mathbb{Q}}\, u\left(\mathbb{Q}-1\right) + \\ + c_{p_r^4}\frac{p_r^4}{\mathbb{B}^2} + c_{up_r^2}\, u\frac{p_r^2}{\mathbb{B}} + c_{p_r^2\mathbb{Q}}\frac{p_r^2}{\mathbb{B}}(\mathbb{Q}-1). \tag{117}$$

The explicit expression of the c_X coefficients can be obtained comparing Eqs. (116) and (117) to Eqs. (51) and (52) of Ref. [199] and are recalled in Appendix D of Ref. [230]. All these coefficients are linear functions of $(\hat{S}, \hat{S}_*)$. Thus, we can write $\Delta^{(1)}_{\sigma^*} = c^{(1)}_S \hat{S} + c^{(1)}_{S_*}\hat{S}_*$ and $\Delta^{(2)}_{\sigma^*} = c^{(2)}_S \hat{S} + c^{(2)}_{S_*}\hat{S}_*$, and, substituting them into Eq. (115), we obtain

$$\hat{\mathbb{H}}_{\rm SO} \equiv \left(\bar{G}_S \hat{S} + \bar{G}_{S_*}\hat{S}_*\right) p_\varphi, \tag{118}$$

where we defined two *new* gyro-gravitomagnetic functions

$$\bar{G}_S \equiv \bar{G}^0_S + \left(c^{(1)}_S + c^{(2)}_S\right)\mathbb{G}_{\mathbb{S}_*}, \tag{119}$$

$$\bar{G}_{S_*} \equiv \left(1 + c^{(1)}_{S_*} + c^{(2)}_{S_*}\right)\mathbb{G}_{\mathbb{S}_*}. \tag{120}$$

The explicit forms of $\left[c^{(i)}_S, c^{(i)}_{S*}\right]$ are also reported in Appendix D of Ref. [230]. In inspecting those expressions, one should be aware that the two models adopt two different gauges in the spin-orbit sector. On the one hand, `TEOBResumS` is written in the DJS gauge [225, 233] that is designed to cancel all the dependence on $\boldsymbol{p}^2$ in the gyro-gravitomagnetic functions. On the other hand,

within SEOBNRv4 one makes the minimal gauge choice and sets all gauge parameters to be zero. More details can be found in Appendix E of Ref. [230].

4.3.3 $\hat{H}^{\rm eff}_{\rm SS}$ and the spin-spin sector

Moving finally to the spin-spin sector, we define $\hat{H}^{\rm eff}_{\rm SS}$ as

$$\hat{H}^{\rm eff}_{\rm SS} = \hat{H}_{\rm SS} - \frac{1}{2}u^3\big(\hat{\mathbb{S}}_*\big)^2 + \frac{d_{\rm SS}\,\nu}{r^4}\left(X_1^4\chi_1^2 + X_2^4\chi_2^2\right). \tag{121}$$

The first term in the r.h.s. of the above equation, for equatorial orbits (see Eq. (4.19) of Ref. [197] or Appendix A of Ref. [230] for generic ones) explicitly reads

$$\begin{aligned}\hat{H}_{\rm SS} = \omega\,\hat{\mathbb{S}}_* + \frac{e^{-3\tilde{\mu}-\tilde{\nu}}\,\tilde{J}}{2\widetilde{B}\sqrt{\mathbb{Q}}\left(1+\sqrt{\mathbb{Q}}\right)}\times \\ \times\left\{e^{2\tilde{\mu}+2\tilde{\nu}}p_\varphi^2 + e^{2\tilde{\mu}}\sqrt{\mathbb{Q}}\left(1+\sqrt{\mathbb{Q}}\right)\widetilde{B}^2 - \tilde{J}^2p_r^2\widetilde{B}^2\right\}\omega'\,\hat{\mathbb{S}}_*,\end{aligned} \tag{122}$$

where

$$\omega \equiv \frac{\tilde{\omega}_{fd}}{\Lambda_t} = \bar{G}^0_S\,\hat{S}. \tag{123}$$

Using Eqs. (107), (108) and (123), $\hat{H}_{\rm SS}$ can be rewritten as

$$\begin{aligned}\hat{H}_{\rm SS} = \left\{\bar{G}^0_S + \frac{\bar{r}_c}{2\sqrt{\mathbb{B}}}\left[1 - \frac{1}{\sqrt{\mathbb{Q}}\left(1+\sqrt{\mathbb{Q}}\right)}\times\right.\right. \\ \left.\left.\times\left(p_\varphi^2\bar{u}_c^2 - \frac{p_{r_*}^2}{\mathbb{A}}\right)\right]\left(\bar{G}^0_S\right)'\right\}\hat{S}\;\hat{\mathbb{S}}_*.\end{aligned} \tag{124}$$

The second term in the r.h.s. of Eq. (121) was introduced in Ref. [197] [see Eqs. (5.59), (5.60) and (5.70) therein and related discussion] to correctly account for the LO spin-spin coupling. One easily checks that PN-expanding the whole $\hat{H}^{\rm eff}_{\rm SS}$ together

with $\hat{\mathbb{H}}^{\rm eff}_{\rm orb}$ is necessary to correctly recover the LO spin-spin contribution in the full Hamiltonian, $\hat{H}^{\rm LO}_{\rm SS} = -u^3(\hat{S} + \hat{S}_*)^2/2 = -\tilde{a}_0^2/2$. This constitutes the main structural difference between `TEOBResumS` and `SEOBNRv4` in the spin-spin sector. In fact, in the former even-in-spin terms are fully resummed through r_c, while in the latter these terms are partially resummed within $\bar{r}_c$ and partly added to the Hamiltonian as they are.

We also note in passing that, by expanding $\mathbb{H}^{\rm eff}_{\rm orb}$, one also finds the Kerr-like quartic-in-spin term $\hat{S}^4/2$. This term takes into account only a fraction of the analytically known LO quartic-in-spin Hamiltonian. By contrast, it was shown in Ref. [194] that this is completely incorporated in the `TEOBResumS` Hamiltonian because of the use of effective spin $\tilde{a}_0$ within r_c.

Finally, Eq. (121) also features the presence of an effective NLO spin-spin correction, with the adjustable parameter $d_{\rm SS}$ that will be discussed below.

4.3.4 Numerical relativity calibrated functions

As briefly mentioned above, the `SEOBNRv4` analytic structure is completed by 3 functions that are calibrated to NR simulations. These functions are: (i) K, that enters Δ_u; (ii) $d_{\rm SO}$, that is found in the definition of the effective spin variable $\hat{\mathbb{S}}_*$; and (iii) $d_{\rm SS}$ that affects the spin-spin coupling. The NR-calibrated expression of K was obtained in Ref. [204] and reads

$$K = K|_{\chi=0} + K|_{\chi\neq 0}, \tag{125}$$

where we introduced the functions

$$\begin{aligned} K|_{\chi=0} &= 267.788247\nu^3 - 126.686734\nu^2 + 10.257281\nu + \\ &\quad + 1.733598, \end{aligned} \tag{126}$$

$$\begin{aligned} K|_{\chi\neq 0} &= -59.165806\,\chi^3\nu^3 - 0.426958\,\chi^3\nu + 1.436589\,\chi^3 + \\ &\quad + 31.17459\,\chi^2\nu^3 + 6.164663\,\chi^2\nu^2 - 1.380863\,\chi^2 + \\ &\quad - 27.520106\,\chi\nu^3 + 17.373601\,\chi\nu^2 + 2.268313\,\chi\nu + \\ &\quad - 1.62045\,\chi, \end{aligned} \tag{127}$$

where

$$\chi \equiv \chi_S + X_{12}\frac{\chi_A}{1-2\nu} = \frac{\hat{S}}{X_1^2 + X_2^2}, \tag{128}$$

with $\chi_S = (\chi_1 + \chi_2)/2$ and $\chi_A = (\chi_1 - \chi_2)/2$. The spin-orbit sector presents an additional N^{3}LO effective correction that reads

$$\begin{aligned} d_{\rm SO} &= 147.481449\,\chi^3\nu^2 - 568.651115\chi^3\nu + \\ &\quad + 66.198703\,\chi^3 - 343.313058\,\chi^2\nu + \\ &\quad + 2495.293427\,\chi\nu^2 - 44.532373\,. \end{aligned} \tag{129}$$

Finally, the NLO effective spin-spin correction that enters $\hat{H}^{\rm eff}_{\rm SS}$ is NR-calibrated through the parameter

$$\begin{aligned} d_{\rm SS} &= 528.511252\,\chi^3\nu^2 - 41.000256\,\chi^3\nu + \\ &\quad + 1161.780126\,\chi^2\nu^3 - 326.324859\,\chi^2\nu^2 + \\ &\quad + 37.196389\,\chi\nu + 706.958312\,\nu^3 + \\ &\quad - 36.027203\,\nu + 6.068071. \end{aligned} \tag{130}$$

As all these coefficients depend on multiple powers of the individual spins, a clear distinction between the spin-orbit and spin-orbit sectors is impossible.

4.4 Select comparisons

We have seen that the `TEOBResumS` and `SEOBNRv4` Hamiltonians are constructed rather differently. They differ in the amount

of analytical information that is included, the spin-gauge, the resummation procedures and the way they are informed (or calibrated) to NR simulations. Still, both models deliver waveforms that are *faithful* with state-of-the-art NR simulations at 1% level or better [204, 166]. This is possible because, on top of the tunable functions that enter the dynamics of the two models, (a_6^c, c_3) and $(K, d_{\rm SO}, d_{\rm SS})$ the waveforms are also NR-completed through merger and ringdown in some way. The aim of this section is to attempt to quantify the differences entailed by the two NR-informed Hamiltonians. To do so, we focus on the gauge-invariant relation between energy and angular momentum (or orbital frequency) and we calculate them both in the adiabatic approximation as well as non-adiabatically, switching on some analytical radiation reaction to account for the angular momentum losses.

4.4.1 Adiabatic dynamics

Our interest is to make some comparative statements between the dynamics of the two models. Since the models are calibrated to NR, and moreover are expressed in different gauges, direct comparisons between the analytical expressions discussed above are not informative. On the contrary, comparisons between gauge-invariant quantities are meaningful and we start by considering the *adiabatic* approximation to the dynamics, i.e. a sequence of circular orbits. We hence set $p_{r_*} = 0$ and compute, at each given radius, the circular angular momentum $p_\varphi^{\rm circ}$ solving $\partial \hat{H}_{\rm eff}(r, p_\varphi)/\partial r|_{p_\varphi = p_\varphi^{\rm circ}} = 0$. We can then compare the rescaled binding energy of a system $\hat{E}_b \equiv (E - M)/\mu$ of the two models, when plotted as a function of the angular momentum p_φ or of the dimensionless orbital frequency $\Omega \equiv M\Omega_{\rm phys} = \partial \hat{H}_{\rm EOB}/\partial p_\varphi$.

The results of these comparisons are shown in Fig. 1. From simplicity, in the following we will often denote `TEOBResumS` as

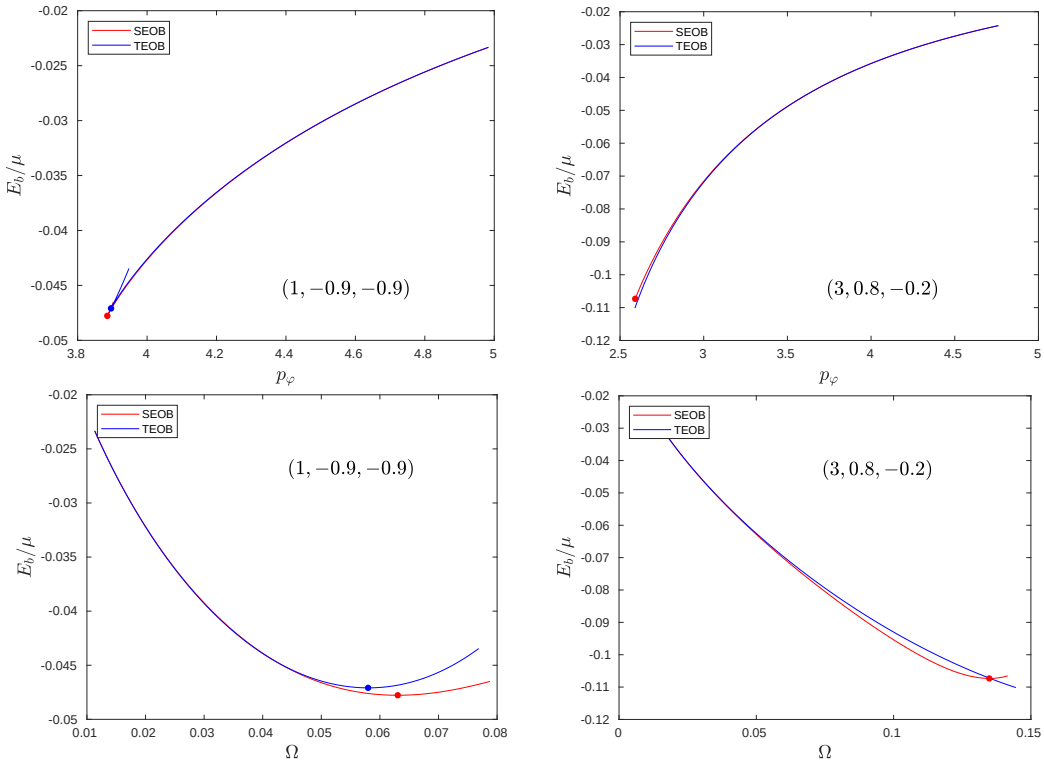

Figure 1: Gauge-invariant relation between E_b and p_φ and Ω in the adiabatic case. We show two selected configurations: $(q, \chi_1, \chi_2) = (1, -0.9, -0.9)$ and $(3, 0.8, -0.2)$ The markers correspond to the LSO position (not present in `TEOBResumS` for large aligned spins).

TEOB and `SEOBNRv4` as SEOB. The markers highlight the location of the last stable orbit (LSO), which corresponds to the inflection point of the Hamiltonian and is thus found imposing $\partial \hat{H}_{\rm eff}/\partial r = \partial^2 \hat{H}_{\rm eff}/\partial r^2 = 0$. As expected, the binding energies are similar but not exactly overlapping. It is difficult to quantify the effects of this difference, but it is probably tapered in the full models, when taking into account the respective radiation reactions. In the next section, we will compare binding energy in the non-adiabatic scenario, adding the same radiation reaction to both models.

The general characteristics of the dynamics can be also sum-

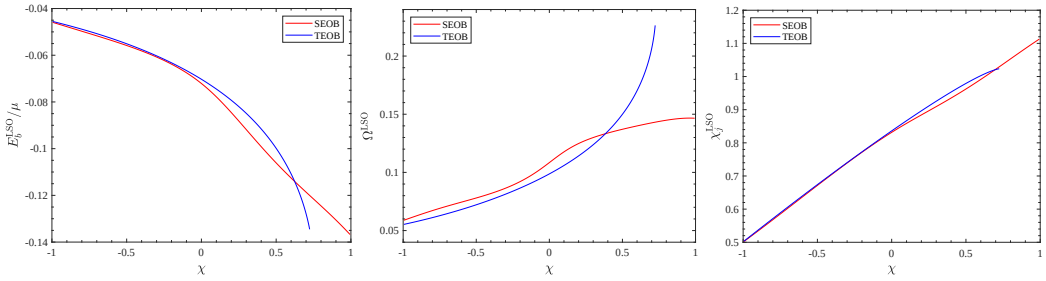

Figure 2: Gauge-invariant quantities computed at the LSO for equal-mass, equal-spin systems versus $\chi = \chi_1 = \chi_2$. Note that the `TEOBResumS` Hamiltonian does not have an LSO after $\chi \approx 0.7$ and thus the corresponding curves terminate there.

marized by inspecting various gauge-invariant quantities at the LSO, i.e. binding energy, orbital frequency and the dimensionless Kerr parameter

$$\chi_J \equiv \frac{1}{\nu} \frac{j_{\rm tot}}{\hat{H}^2_{\rm EOB}}, \tag{131}$$

where $j_{\rm tot}$ is total angular momentum and reads

$$j_{\rm tot} = p_\varphi + \frac{X_1}{X_2}\chi_1 + \frac{X_2}{X_1}\chi_2 \,. \tag{132}$$

This is done in Fig. 2, that refers to the equal-mass, equal-spin case. On the x-axis we put $\chi = \chi_1 = \chi_2$. Note that the curve for `TEOBResumS` stops at $\tilde{a} \approx 0.7$ because the LSO does not exist for higher spins. We will comment more on this aspect in the conclusions. It is interesting to note that for large, positive spins `TEOBResumS` predicts values of the LSO frequency larger than the `SEOBNRv4` ones.

The last piece of information that can be extracted from the two Hamiltonians in the adiabatic case concerns the spin-orbit and spin-spin contributions. In fact, if we consider small spins,

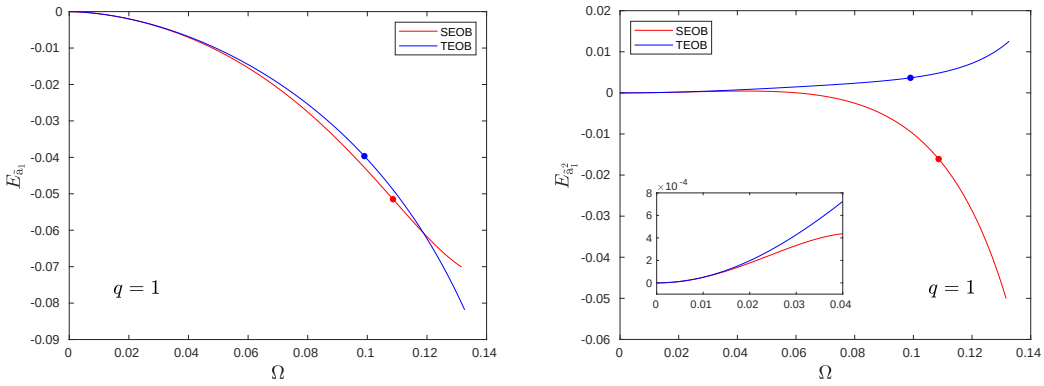

Figure 3: Linear and quadratic-in-spin Hamiltonian contributions in the equal-mass case. $E_{\tilde{a}_1}$ qualitatively agrees between the two models. The quadratic-in-spin behaviour is instead completely different, although it is similar in the PN regime. We remind the reader that for these systems $E_{\tilde{a}_1} = E_{\tilde{a}_2}$ and $E_{\tilde{a}_1^2} = E_{\tilde{a}_2^2}$, while $E_{\tilde{a}_1\tilde{a}_2}$, though not shown, displays a similar behavior to $E_{\tilde{a}_1^2}$. The markers highlight the non-spinning LSO position.

$\tilde{a}_i \ll 1$, we can expand the Hamiltonian as

$$\begin{aligned}\hat{H}_{\rm EOB}\left(\nu, \tilde{a}_1, \tilde{a}_2\right) \sim\ & E_0(\nu) + E_{\tilde{a}_1}(\nu)\,\tilde{a}_1 + E_{\tilde{a}_2}(\nu)\,\tilde{a}_2 + \\ & + E_{\tilde{a}_1^2}(\nu)\,\tilde{a}_1^2 + E_{\tilde{a}_1\tilde{a}_2}(\nu)\,\tilde{a}_1\tilde{a}_2 + \\ & + E_{\tilde{a}_2^2}(\nu)\,\tilde{a}_2^2 + \mathcal{O}[\tilde{a}_i^3]. \end{aligned} \tag{133}$$

In this situation, the E_X functions are well defined and depend on the mass ratio and dynamical variables but not on the spin values. These functions hence encode the way the linear and quadratic-in-spin terms are described in the two models. We can obtain each contribution analytically differentiating $\hat{H}_{\rm EOB}$, e.g. $E_{\tilde{a}_1} = (\partial \hat{H}_{\rm EOB}/\partial \tilde{a}_1)|_{\tilde{a}_i=0}$. For simplicity, we instead compute them numerically, considering very small (positive or negative) spins and suitably summing/subtracting the corresponding energies so to obtain the coefficients. For example, $E_{\tilde{a}_1} = \left[\hat{H}_{\rm EOB}|_{(\tilde{a}_1=a,\,\tilde{a}_2=0)} - \hat{H}_{\rm EOB}|_{(\tilde{a}_1=-a,\,\tilde{a}_2=0)}\right]/(2a)$, with $a \sim 10^{-4}$.

Note that in the adiabatic case, using p_φ as a variable is problematic, as it presents a cusp at the LSO, when the stable

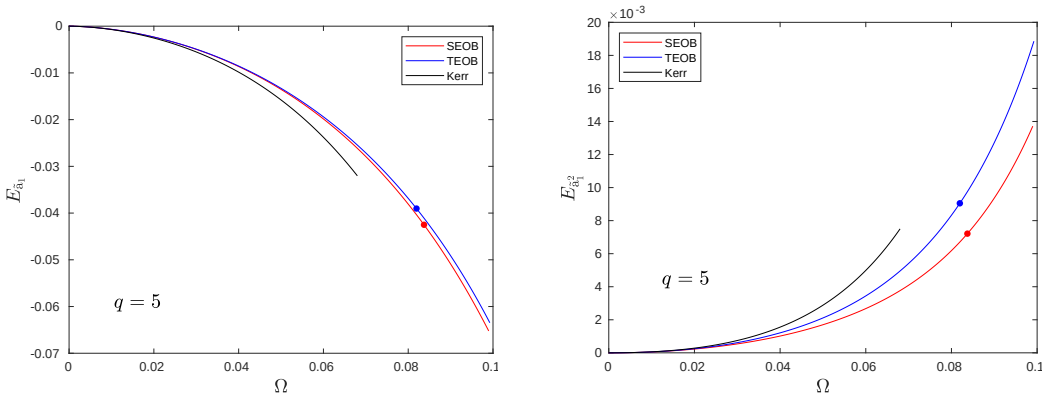

Figure 4: Same as Fig. 3 for systems of $q = 5$. We also added the Kerr corresponding functions up to the Schwarzschild LSO. In this case, all three curves agree qualitatively.

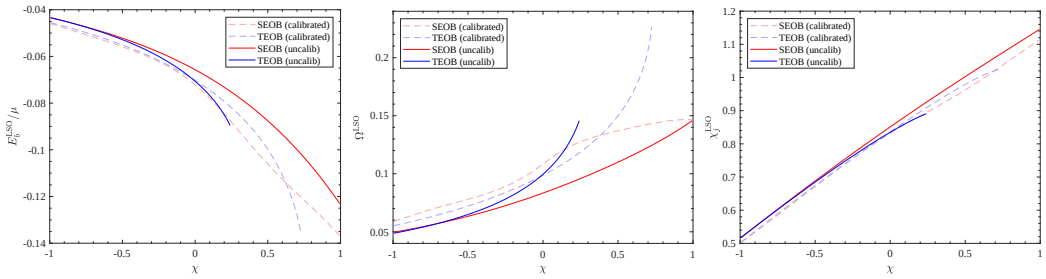

Figure 5: Same as Fig. 2 using models without NR information, i.e. setting all calibration coefficients to zero. The NR-informed `TEOBResumS` and `SEOBNRv4` are indicated with dashed lines. Without calibration, `TEOBResumS` does not have an LSO after $\chi \approx 0.3$.

and unstable orbits branches meet. Moreover, the spin-squared contributions are singular at the same point when plotted versus the angular momentum. Conversely, the orbital frequency is continuous and well-behaved near the LSO, making it more useful for comparisons. The results for equal-mass systems are exhibited in Fig. 3.

The figure illustrates that $E_{\tilde{a}_1}$ is reasonably consistent between the two models, although it has a slightly different behavior after the non-spinning LSO. $E_{\tilde{a}_1^2}$, instead, is completely different. The two curves behave similarly in the PN regime (for

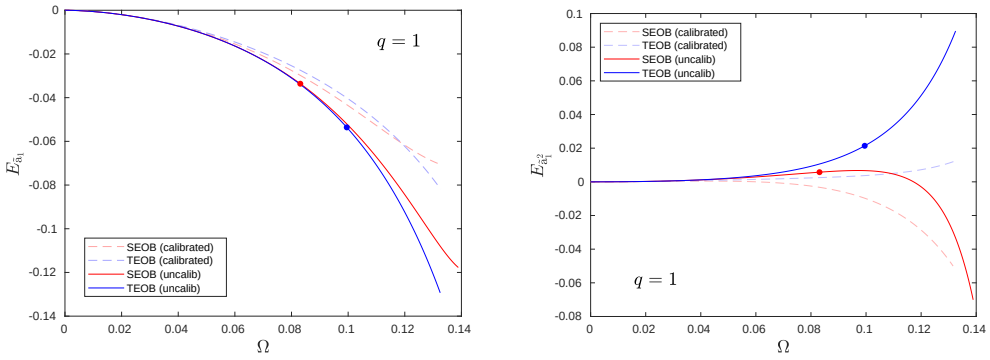

Figure 6: Comparison of $E_{\tilde{a}_1}$ and $E_{\tilde{a}_1^2}$ for `TEOBResumS` and `SEOBNRv4` without NR calibration. The dashed lines correspond to the curves of Fig. 3. It is possible to notice how the non-calibrated curves are closer and have a more similar behavior up the LSO. Moreover, we can see that both the spin-orbit and spin-spin interactions are tempered by the use of NR information.

small values of Ω) but quickly start to disagree and even change sign well before the LSO. Some difference was to be expected due to the different included PN information and way to include spin-spin terms within the EOB framework.

Since these functions are universal, we can extract the linear-in-spin contribution for any value of the spins as $E_{\tilde{a}_1}\tilde{a}_1 + E_{\tilde{a}_2}\tilde{a}_2$, even if for large spins the expansion of Eq. (133) is no longer valid and higher order contributions become non-negligible. Thus, we expect that these differences will be more pronounced for large aligned spins, when the LSO occurs at higher frequencies.

As a consistency test, we show in Fig. 4 the same comparison for $q = 5$, together with the Kerr corresponding curves. As expected, since the two models share the same $\nu \to 0$ and PN limits, in this case the curves have a similar behavior and are close to the Kerr functions.

As we briefly mentioned in the previous sections, the NR-informed parameters introduce a complicated spin-dependence in both models. In order to remove these effects, we compare in Fig. 5 the LSO quantities for `TEOBResumS` and `SEOBNRv4`, after eliminating the NR-calibration, i.e. we impose $a_6^c = c_3 = 0$

and $K = d_{\rm SS} = d_{\rm SO} = 0$ respectively. Two features become evident: (i) `TEOBResumS` does not display an LSO for $\chi \geq 0.3$; (ii) `SEOBNRv4` has a behavior that is Kerr-like and does not display a change of concavity.

We conclude this section by showing in Fig. 6 the comparisons between $E_{\tilde{a}_1}$ and $E_{\tilde{a}_1^2}$. We can see that that the main effect of using NR information is a decrease in the importance of the spin terms. However, NR-calibrated terms also change the behavior of the spin interaction. Without these, the `TEOBResumS` and `SEOBNRv4` curves are closer and $E_{\tilde{a}_1^2}$ is positive for both models up to the LSO.

4.4.2 Non adiabatic dynamics

Let us now complement the above section with similar comparisons based on *non-adiabatic* evolutions, so to get up to merger. To do so, for both Hamiltonians we write Hamilton's equations with the *same* radiation reaction $\mathcal{F}_\varphi$. For consistency between `TEOBResumS` and `SEOBNRv4`, we use the formal expression of $\mathcal{F}_\varphi$ discussed in Ref. [166], where however the argument x is taken to be $x = \Omega^2 (\Omega|_{p_r=0})^{-4/3}$. We stress that this choices does not correspond to neither the `TEOBResumS` nor the `SEOBNRv4` one. The purpose of this section is to purely explore the structure of the Hamiltonians in the strong field, and compare them. It is intended that the full energetics obtained from this dynamics is not expected to be fully compatible with the corresponding NR one, like it is for the NR-completed model [191]. Similarly, we don't improve the inspiral EOB analytical waveform with a NR-improved description of the merger (i.e., next-to-quasi-circular corrections) nor ringdown, but we adopt it as is. However, since its amplitude has a peak that is known to be close (both in location and amplitude) to the actual merger point obtained by NR simulations, we use it as an *approximate* merger point

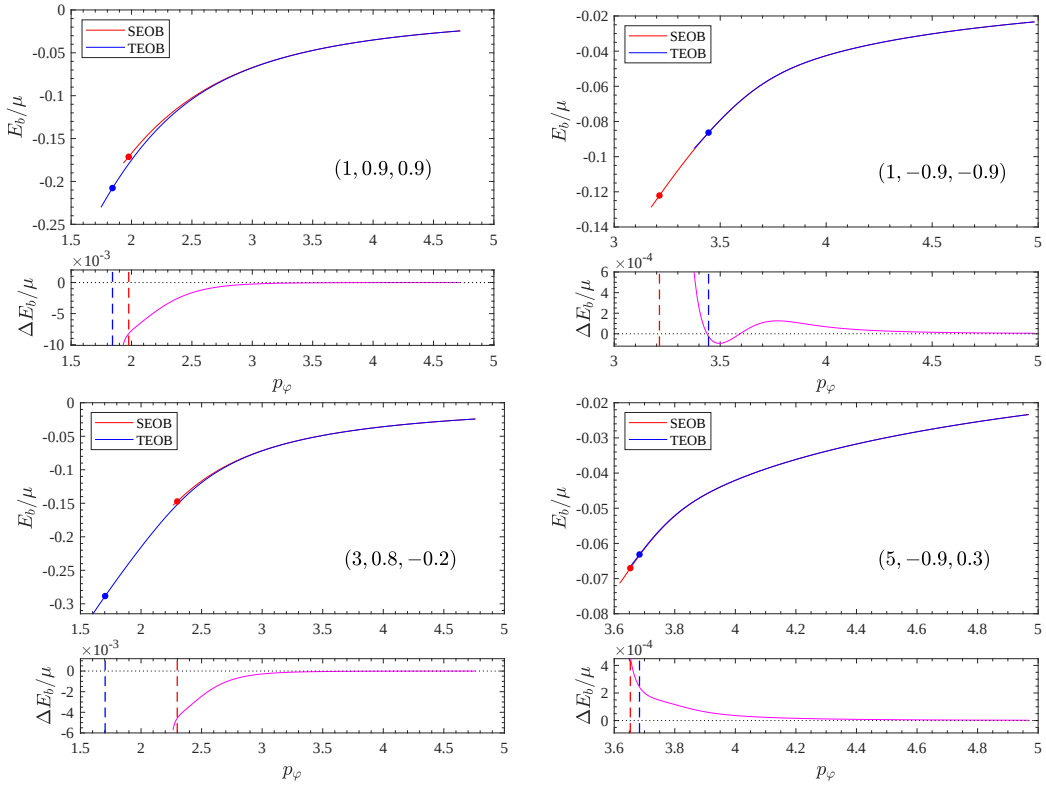

Figure 7: Non-adiabatic evolution: gauge-invariant relation between binding energy E_b/μ and orbital angular momentum p_φ obtained using the two different `TEOBResumS` and `SEOBNRv4` Hamiltonians, but the same radiation reaction. The chosen configurations are the same of Fig. 2. The markers highlight the position of the peak of the $(2,2)$ mode. The lower panel shows the difference $\Delta E_b/\mu = (E_b^{\rm TEOB} - E_b^{\rm SEOB})/\mu$.

(note that this is the choice usually adopted in the analytical description of coalescing and merging BNS). Such approximate merger location will be useful below. Fig. 7 compares the relation $E_b(p_\varphi)$ of the two models for a few configurations. The approximate merger point (as defined above) for each model is shown as a colored marker. One sees that, on randomly chosen configurations, the global differences are non negligible. In particular, they are larger than the expected uncertainty on the corresponding NR curves ($\sim 10^{-4}$). Moreover, the position of

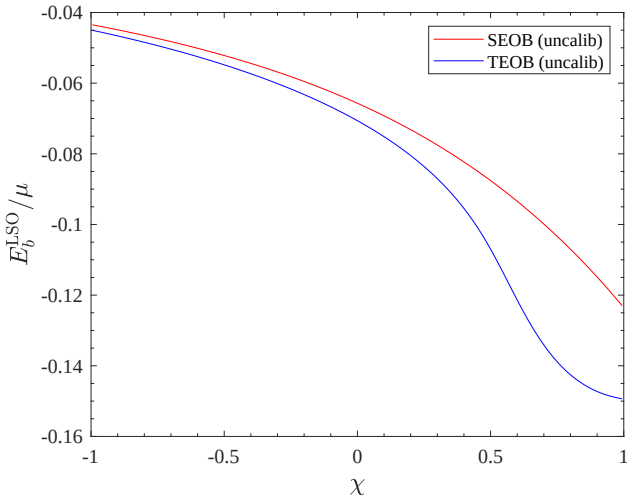

Figure 8: Rescaled binding energy $\hat{E}_b \equiv E_b/\mu$ at the LSO for equal-mass, equal-spin systems. This is obtained with the non-calibrated Hamiltonians of `SEOBNRv4` and `TEOBResumS`, where the latter includes a new G_{S_*} with the complete spinning particle information. Note that this new flavor of `TEOBResumS` presents an LSO for all values of the spin $\chi = \chi_1 = \chi_2$.

the $(2, 2)$ peak is often very different, with `TEOBResumS` merging later for large aligned spins and sooner for anti-aligned ones.

4.4.3 Specific modifications

We have seen that, due to the several structural differences between the two models, it is difficult to understand clearly what special physical element is responsible for some specific dynamical behavior. Generally speaking one sees that the two models implement a fundamentally different description of the spin-spin interaction and this eventually reflects on all diagnostics that we have analyzed.

To shed more light on the impact of the various analytical structure, we focus here on a specific analytical element. From this point of view, we want to stress that most of the spinning-particle information that is encoded in $G^K_{S_*}$ is missing in `TEOBResumS`, that is thus analytically *less complete* than

SEOBNRv4. One should however be aware that nothing prevents us from the possibility of injecting the same information into an alternative TEOBResumS Hamiltonian that, however, maintains the same global structure as the current one. In particular, the features that we want to preserve are: (i) the use of r_c with $\tilde{a}_0$ for spin-spin interaction and (ii) the use of factorized (and then resummed) (G_S, G_{S_*}) function. In particular, one would like to keep for G_{S_*} a factorized expression of the form

$$G_{S_*} = G^0_{S_*} \hat{G}_{S_*}, \tag{134}$$

where now $G^0_{S_*}$ reduces to $G^K_{S_*}$, Eq. (50), when $\nu = 0$ and *not* just to the first term of the PN expansion, $3/2\, u^3$. To achieve this, one cannot work in the DJS gauge, but in a different gauge such that the standard PN-expanded G_{S_*} coincides with the Taylor expansion of $G^K_{S_*}$ when $\nu = 0$. One finds that this gauge is defined by the condition that all the ν-dependent terms that depend on the radial momentum disappear. The corresponding choice of the gauge parameters is reported at the end of Appendix E of Ref. [230]. A new spin-orbit sector that fully incorporates the spinning particle information can be obtained as follows: (i) one factorizes out from $g^{\rm eff}_{S_*}$ the $r^3 G^K_{S*}$ terms up to NNLO; (ii) $G^0_{S_*}$ is taken to have the same functional form of $G^K_{S_*}$ where, however, the various Kerr functions (r^K_c, A^K, B^K, Q^K) are replaced by the EOB ones, (r_c, A, B, Q), with their complete ν-dependence. Similarly, the Kerr spin is replaced by the $\tilde{a}_0$ effective spin variable. The functions A and B are then resummed using the usual TEOBResumS prescriptions; finally, the new functions $(\hat{G}_S, \hat{G}_{S_*})$, that explicitly depend on ν, and are both in the form $1 + \ldots$, are also resummed using their inverse Taylor representation, analogously to what is done in the DJS gauge. We found that incorporating the (ν-deformed) spinning-particle information within this new flavor of TEOBResumS fixes one of the long standing issues of the model in DJS gauge, i.e. the fact

that the LSO does not exist for large, positive spins ≥ 0.7, as recalled in the text and as pointed out in Ref. [224]. For this study, we also kept r_c at LO, i.e. setting $\delta a^2 = 0$ in Eq.(63), so to use the same amount of PN information as `SEOBNRv4`. Figure 8 shows the binding energy at the LSO obtained with this new model: one sees that the LSO always exists also for quasi-extremal, positive spins. We could also verify that, once implemented in the time-domain code to provide the full transition from early inspiral to plunge, merger and ringdown, the Hamiltonian in the new gauge maintains the same robustness and flexibility that was typical of the DJS gauge one. We also found that, analogously to this case, an effective spin-orbit parameter is necessary to get a good phasing agreement with NR simulations.

4.5 Summary

We performed a comprehensive analytic comparison between the Hamiltonians of the two state-of-the-art EOB waveform models for coalescing BBHs, `TEOBResumS` and `SEOBNRv4`. In particular, we have illustrated that the `SEOBNRv4` Hamiltonian can be *formally* written similarly to the `TEOBResumS` one, though with different potentials. We report the main differences in Table 1. Generally speaking, this allowed us to illustrate that the most important structural differences between the two models lie in the way the ν-deformation is implemented in the spin sector.

More precisely:

(i) *Centrifugal radius and spin-spin sector.* We have pointed out that in the orbital part of the `SEOBNRv4` Hamiltonian it is possible to identify a *centrifugal radius* function $\bar{r}_c$ [Eq. (103)], similarly to r_c within `TEOBResumS` [Eq. (63)]. This function incorporates, in resummed form, some of the even-in-spin contribution, as in the case of a non-spinning

Table 1: We here summarize the main structural differences between the conservative dynamics of `TEOBResumS` and `SEOBNRv4`. We remind the reader that the complete dynamics differ also in the way NR information is incorporated.

TEOBResumS	**SEOBNRv4**
Deformed Hamiltonian structures: $1-2u_c^K \to A_{\rm orb}$ [Eq. (60)]	Deformed metric structures: $\Delta^K \to \Delta_u$ [Eq. (94)]
Event horizon not always present	Imposed two Kerr-like horizons [Eq. (94)]
A and D potentials resummed using Padé approximants [Eqs. (60) and (67)]	Δ_u and $\mathbb{D}$ potentials resummed through logarithms [Eqs. (94) and (96)]
Effective spin variable: $\hat{a} \to \tilde{a}_0 = X_1\chi_1 + X_2\chi_2$ [Eq. (63)]	Effective spin variable: $\hat{a} \to \hat{S} = X_1^2\chi_1 + X_2^2\chi_2$ [Eqs. (86)-(90)]
Only leading PN correction in spin-orbit sector [Eq. (71)]	Conserved spinning-particle structure in G_{s_*} [Eq. (98)]
Spin-spin resummed through: $u_c^K \to u_c$ [Eqs. (58) and (63)]	Spin-spin terms added to the Hamiltonian [Eq. (79)]

particle on Kerr. However, $\bar{r}_c$ and r_c are very different functions, notably because of the choice of the effective spin quantity. In particular, in `TEOBResumS` the use of $\tilde{a}_0$ allows one to automatically incorporate within r_c the LO quadratic-in-spin (as well as quartic-in-spin) terms. This is not the case for `SEOBNRv4`, that uses $\hat{S}$, so that a compensation term in the effective Hamiltonian, $\hat{H}^{\rm eff}_{SS}$ [Eq. (121)] has to be introduced. Another important difference comes from the fact that the resummation choices of `SEOBNRv4` include in $\bar{r}_c$ the ν-dependent terms of Δ_u which are not present in `TEOBResumS`.

(ii) *Spin-orbit sector.* We attempted to provide a one to one comparison between the spin-orbit sectors of the two models, rewriting the corresponding part of the `SEOBNRv4` Hamiltonian like the `TEOBResumS` one. We identified the two gyrogravitomagnetic functions $(\bar{G}_S, \bar{G}_{S_*})$, Eqs. (68) and (69), in the former that correspond to (G_S, G_{S_*}), Eqs. (119) and (120), in the latter. These functions differ both in the gauge choice and in the analytical content. We have explicitly showed that in `SEOBNRv4`, the spin-orbit Hamiltonian can be obtained starting from the expression of Ref. [231] and *ν-deforming* it in some way, replacing the Kerr functions (r_c^K, A^K, B^K, Q^K) with $(\bar{r}_c, \mathbb{A}, \mathbb{B}, \mathbb{Q})$, that incorporate additional ν-dependent effects. The main difference here is that within `SEOBNRv4` the $G^K_{S_*}$ function contains the full spinning-particle information, while this is approximated to (N^{3}LO) in `TEOBResumS`.

We also made some quantitative comparisons between the two models. We compared the gauge-invariant relations between energy, angular momentum and orbital frequency, both for adiabatic and nonadiabatic dynamics. In doing so, we compared and contrasted the linear-in-spin and quadratic-in-spin contri-

butions of the two Hamiltonians. We found relevant qualitative and quantitative differences, especially in the spin-spin sector. The discrepancies are mitigated by the calibration to NR simulations. This is not surprising, since we expect the use of numerical information to drive the generated waveforms towards the "exact" GR result.

We finally demonstrated how the inclusion of different analytical information can impact the model. One should note that similar results could be obtained by changing one of the resummation schemes and all these aspects enter into the analysis of waveform systematics. Fortunately, NR information helps mitigating these effects, but a deep understanding of the underlying analytical structures is fundamental in order to push EOB-NR models to their accuracy limits.

5 EOB waveforms for dynamical captures

In dense stellar regions, such as galactic nuclei and globular clusters, BHs can become gravitationally bound as they lose energy to gravitational radiation during a close passage [234, 235]. Such dynamically captured pairs may lead to highly eccentric mergers with a phenomenology that is radically different from quasi-circular inspirals [236, 237]. The future detection of these mergers [238, 239] can provide invaluable insights on astrophysical BHs. Due to the special waveform morphology, these systems might be either missed or incorrectly analyzed using standard quasi-circular templates [240, 241, 209, 242, 243].

Physically faithful waveform models to systematically study the phenomenology of dynamical captures do not currently exist. Similarly, NR studies of BBH mergers from dynamical capture conducted thus far are only few [240, 244, 245, 246]. EOB-based models are a suitable candidate to fill this gap, since they solve the system dynamics instead of having a prescription to generate the waveform itself [247].

In the following, we will describe the application of a state-of-the-art EOB model to the generation of multipolar merger-ringdown waveform from dynamical capture BH mergers with arbitrary mass-ratios and nonprecessing spins. The model relies on analytical descriptions of the radiation reaction and waveform along generic orbits proposed in Ref. [170]. However, it is currently impossible to make precise quantitative statements on the actual faithfulness of the analytical waveforms because of the lack of systematic predictions from NR simulations of dynamical capture coalescing binaries.

The contents of this section were originally published as "A. Nagar et al., *Phys. Rev. D* **103** 064013 (2021)" [248].

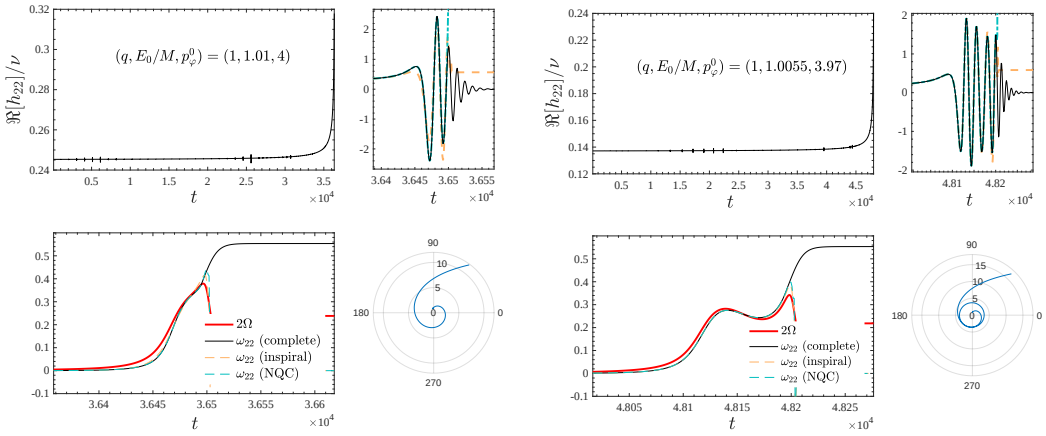

Figure 9: Waveform phenomenology for $q = 1$: selected configuration to illustrate two distinct single-burst phenomenologies: a direct plunge (left panel) and a configuration with a quasi-circular orbit preceding the plunge (right panel). Each configuration is characterized by initial data $(q, E_0/M, p^0_\varphi)$. The top row of each panel shows the real part of the $\ell = m = 2$ waveform, completed with merger and ringdown (black line), with close ups onto the final merger part. The left-bottom panel exhibits the gravitational wave frequency, while the right-bottom the last part of the relative separation $r(\varphi)$. The panels also show: (i) the purely analytical EOB (inspiral) waveform and frequency (orange line); (ii) the waveform completed by NR-informed next-to-quasi-circular corrections (NQC, blue line). Note that the analytical EOB waveform accounts for the GW emission up to the largest peak of the orbital frequency Ω (red line). It is only after that this point is reached that the postmerger-ringdown description is attached, analogously to the quasi-circular case [190, 192, 166, 195, 196].

5.1 Dynamical capture phenomenology

Let us give a general overview of the properties of the relative dynamics and waveforms from dynamical capture as predicted by our EOB model. Note that we will discuss the scattering scenario in Sec. 5.2 below. To simplify the discussion, we start by considering the $q = 1$, non-spinning case. To setup initial data, we consider values of the angular momentum p_φ sufficiently larger than the value at the LSO, $p^{\rm LSO}_\varphi$ so as to allow for the peak

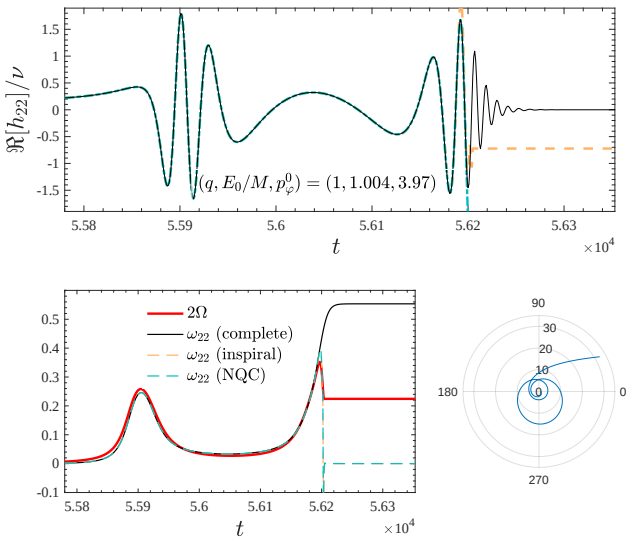

Figure 10: Same as Fig. 9, but to illustrate a waveform with a double burst phenomenology, that corresponds to a close encounter then followed by plunge, merger and ringdown.

of the potential energy to be larger than one [6]. For each value of p_φ we select values of the energy between $(E_{\rm min}, E_{\rm max})$ as mentioned above. At a qualitative level, for a given value of p^0_φ, as the energy is decreased from $\hat{E}_{\rm max} \equiv E_{\rm max}/M$, the system passes through the following stages: (i) direct capture/plunge; (ii) one, or more, close encounters before merger; (iii) close passage and scattering. In practice, the detailed behavior as energy is decreased is more complicated, because, as $\hat{E}_0 \equiv E_0/M \to 1$ the system moves from scattering configurations to (many) close encounters that eventually end up with gravitational capture. More details on this phenomenology will be given below.

To start with, Figures 9 and 10 show three waveforms with nearly the same value of the angular momentum where the energy is progressively decreased. The configurations were selected so that one can appreciate the transition from immediate scat-

[6]For the non-spinning case, from the conservative EOB Hamiltonian one obtains $p^{\rm LSO}_\varphi(\nu) = 3.4643 - 0.774482\nu - 0.692\nu^2$.

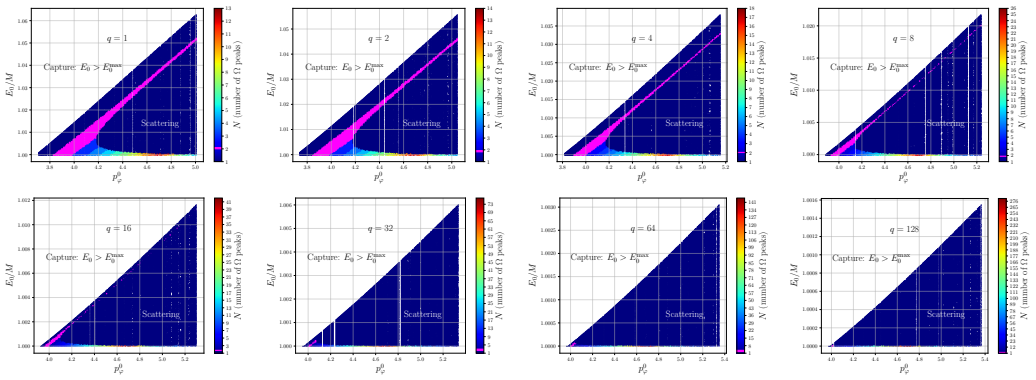

Figure 11: Analysis of the parameter space of hyperbolic encounters of non-spinning BBHs parameterized in terms of initial data $(q, E_0/M, p_\varphi^0)$. The number of multiple encounters ($N \geq 2$) increases with q, while the corresponding area on the parameter space gets smaller and smaller. Note the separation, given by the colored area, between configurations that scatter and configurations that eventually merge.

tering (left panel of Fig. 9) to a quasi-circular capture (right panel of Fig. 9), where the system does a full quasi-circular orbit before plunging, and the case when there is a close encounter followed by capture and merger, Fig. 10. For each configuration, we show: (i) the real part of the waveform; (ii) the gravitational wave frequency ω_{22} together with twice the orbital frequency 2Ω; and (iii) the orbit $r(\varphi)$ of the relative separation. For completeness, in both the waveform and frequency panels we include three curves: (i) the simple, analytical, EOB waveform, with the general Newtonian prefactor as explained in Ref. [170] (dashed, orange); (ii) the waveform corrected by additional next-to-quasi-circular (NQC) factors, that are informed by quasi-circular NR simulations following now standard procedures (light blue, dash-dotted) and the waveform completed with the, similarly NR-informed, ringdown. More precisely, the ringdown is attached at $t = 2M$ after the peak of the $\ell = m = 2$ analytic waveform, according to the standard procedure implemented in the

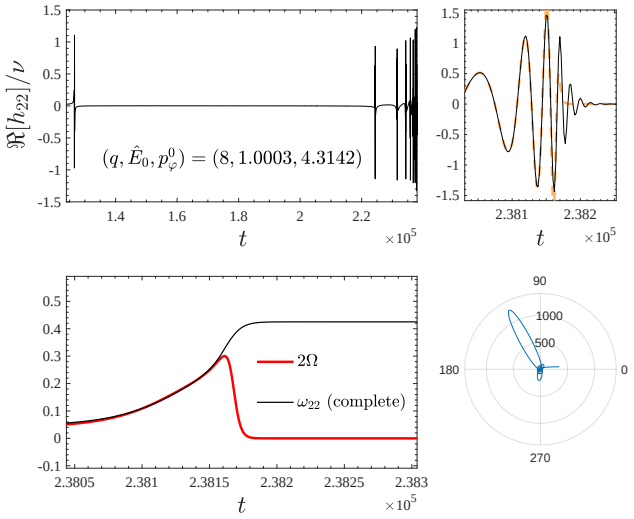

Figure 12: Extreme configuration with $(q, E_0/M, p^0_\varphi) = (8, 1.0003, 4.3142)$ that undergoes eight periastron passages before merger. Note, after the first encounter, the very eccentric orbit, with apastron that reaches $r \simeq 1200$ (bottom left panel). Top right panel: close up on the final plunge, merger and ringdown part of the waveform. For completeness we also incorporate the purely analytical waveform (orange).

various flavors of `TEOBResumS` [196, 170]. To characterize the dynamics, it is useful to look at the morphology of the orbital frequency. In the case of immediate plunge, $\Omega = \dot{\varphi}$ has a single peak, corresponding to the crossing of the EOB effective light-ring. When the energy is lowered (see right panel of Fig. 9), the frequency progressively flattens and an *earlier peak* appears well before the merger one. This "precursor" peak corresponds to a periastron passage with $r_{\rm periastron} \simeq 3.47$; after this, r increases again and eventually the system plunges, with a second peak in Ω. As the energy is further lowered (see Fig. 10), the first peak, that corresponds to the first close passage, becomes clearly distinguishable and separate from the one corresponding to merger. Inspecting the right panel of Fig. 9, one then understands that the divide between having an immediate plunge and a close encounter followed by a plunge is determined by the

condition $\dot{\Omega} = \ddot{\Omega} = 0$, i.e. the orbital frequency should have an inflection point at some time. Inspecting the left panel of Fig. 9, one understands how the late, inspiral-like, part of the orbit is fully mirrored by an entire GW cycles in the purely analytical waveform *before* the ringdown signal actually occurs. Similarly, in the right panel of the figure one finds that the waveform mirrors the quasi-circular dynamics giving four, entire, GW cycles before merger and ringdown.

On the basis of the morphological analysis of above, a simple way to characterize the parameter space of dynamical capture is to focus on the orbital frequency as function of time, $\Omega(t)$, and count how many peaks are present. A single peak may correspond to either immediate plunge or scattering. More generally, when many peaks are present, each peak corresponds to a periastron passage. So, the number of peaks of $\Omega(t)$ is a simple observable, function of $(q, E_0/M, p^0_\varphi)$ that could be used to characterize the parameter space of dynamical capture BBHs [7].

We then consider different mass ratios, $q = \{1, 2, 4, 8, 16, 32, 64, 128\}$ to provide a comprehensive mapping of the parameter space. For each value of the angular momentum, we lower the energy and count the number of peaks of Ω. The result of this analysis is reported in Fig. 11. The colors characterize how many periastron passages the system has undergone before merging. Focusing first on the $q = 1$ case (top-left panel of the figure), one sees that when the energy is decreased from $\hat{E}_{\rm max}$ there are different islands of initial parameters that correspond to progressively more complicated physical behaviors. The plot is split in two by an area that corresponds to the frequency developing two peaks before merger (magenta line). As mentioned above, the upper

[7] An equivalent observable is given by the number of peaks of the gravitational wave frequency, any isolated peak corresponding to a periastron passage. Using the GW frequency has the advantage that the analysis we are discussing here can be directly extended to NR simulations, using then the same peak number as function of initial ADM energy and angular momentum to fully characterize the parameter space.

boundary of this region is defined by those values of $(E_0/M, p^0_\varphi)$ such that $\dot{\Omega} = \ddot{\Omega} = 0$ at some time. Now, the $N = 1$ part of the parameter space *above* the magenta region corresponds to direct plunge, with a waveform phenomenology similar to the one in the left panel of Fig. 9. By contrast, the $N = 1$ part on the right and below the magenta region corresponds to scattering events instead of capture. For a given value of E_0, configurations in the first $N = 1$ region have smaller angular momentum and larger radial momentum, so that the capture is favored. On the contrary, in the second $N = 1$ region it is the angular momentum that dominates, and thus, after a close encounter, the two objects separate again instead of merging. When the initial energy is lowered further, getting close to the stability region, the system attempts to stabilize again and the number of periastron passages before merger increases progressively also for large values of p^0_φ. The phenomenology remains qualitatively the same *also* when the mass ratio is increased, but the region with $N = 2$ becomes narrower and narrower as q increases, notably for $q \geq 32$, when the divide between $N = 1$ configuration is barely visible on the plots (we shall quantify this behavior better below). By contrast, for energies just slightly larger than the (adiabatic) stability limit, the number of possible encounters can grow considerably, up to several tens, although limited to a region of p^0_φ much smaller than in the equal-mass case. We qualitatively interpret this behavior as mirroring the effect that radiation reaction, that is proportional to ν, becomes less and less efficient as ν is decreased and so the system can persist in a metastable state much longer.

In order to give an explicit example of the complicated phenomenology of a capture that occurs after many close encounters, let us consider a configuration with
$(q, E_0/M, p^0_\varphi) = (8, 1.00026983016, 4.3141870095)$, that is exhibited in Fig. 12. The top row of the figure shows the real part

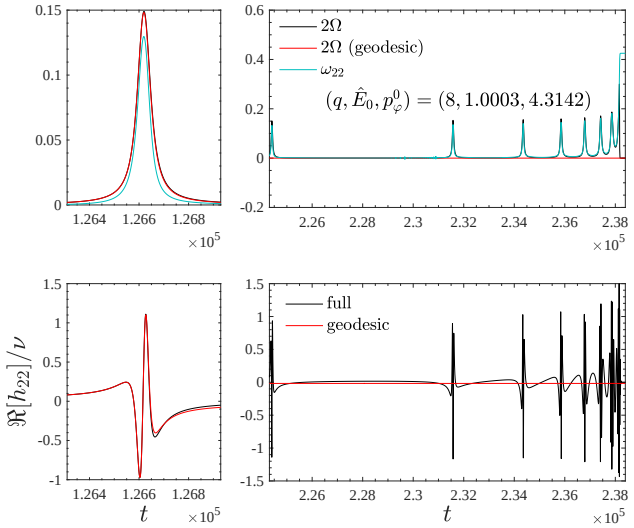

Figure 13: Importance of radiation reaction to determine the multiple-encounters behavior of Fig. 12, with the same initial conditions $(q, E_0/M, p^0_\varphi) = (8, 1.0003, 4.3142)$ considered there. The black lines correspond to the full dynamics with radiation reaction, while the red ones correspond to the conservative dynamics alone. The left panel compares the waveforms during the first periastron passage, while the the right one shows the subsequent encounters and final merger.

of the waveform, each burst corresponding to a close passage. Analogously to what done in Fig. 9, the close up of the waveform around merger (top-right panel) also includes the analytical EOB waveform (orange). The bottom row exhibits the time evolution of the frequency around merger as well as the relative trajectory. After the first encounter, the system undergoes an extremely elliptic orbit, with apastron reaching $r \simeq 1200$, before being captured again. This behavior is determined by the action of radiation reaction around the first close encounter: in that situation the system emits a burst of radiation that eventually makes the orbit close again instead of scattering away. We prove this by setting up the EOB dynamics with the same initial data, but switching off radiation reaction, i.e. both $\hat{\mathcal{F}}_\varphi = \hat{\mathcal{F}}_r = 0$ in the model of Ref. [170]. Figure 13 compares the orbital fre-

quency and waveform of Fig. 12 with the waveform obtained from the conservative dynamics only. The location of the first burst, that corresponds to the first encounter, is essentially the same for both configurations, highlighting that the effect of radiation reaction is practically negligible up to that point. The differences in the waveform (and thus dynamics) occur later, consistently with the fact mentioned above that the effect of radiation reaction is localized around the periastron passage. In the top panel of the figure we also compare the full GW frequency, ω_{22} with twice the orbital frequency Ω, to highlight that $\omega_{22} \neq 2\Omega$ because of the various noncircular effects occurring near the periastron. From this example one also argues that the span of the capture region in the parameter space depends on the details of the model for radiation reaction and may thus change if an improved version of the latter is implemented within the model. We will comment more on the issue of *analytical uncertainty* of the model, and the related importance of NR simulations as a benchmark, in Sec. 5.2 below.

Finally, to put on a more quantitative ground the specific qualitative observations made so far, we compute, for each value $q = \{1, 2, 4, 8, 16, 32, 64, 128\}$ the fraction Y_N of events with N encounters (where the N-th encounter corresponds to merger in case of final capture). Figure 14 exhibits this quantity versus $\nu = q/(1+q)^2$. Configurations with two encounters are always the most frequent ones, although their fraction quickly decreases below 10% for $q > 4$ ($\nu < 0.16$).

5.1.1 Spin

Let us turn now to discussing the effect of the spins (anti)aligned with the angular momentum. At a qualitative level, the waveform phenomenology is analogous to the non-spinning case considered above, though with some quantitative differences due

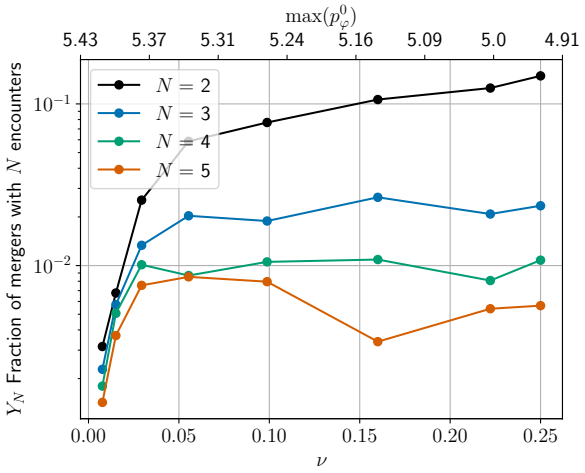

Figure 14: Fraction of BBH configurations (including also scattering events) that end up with N encounters (where the N-th encounter corresponds to merger) for non-spinning binaries. Configurations with $N = 2$ are the most frequent ones, although their frequency quickly decreases below 10% as $q > 4$ ($\nu < 0.16$).

to the spin-orbit and spin-spin interactions. We shall focus first on a special example to highlight the phenomenology. As mentioned above, due to the large initial separation the setup of initial data is insensitive to spin effects, so that the system can be consistently started with the same initial data setup for non-spinning binaries discussed above. In order to single out the effects of spins, we consider the same initial configuration $(q, E_0/M, p_\varphi^0) = (1, 1.0055, 3.97)$ as above, with the following three choices for spins: $\chi_1 = \chi_2 = +0.50$; $\chi_1 = \chi_2 = -0.50$; $\chi_1 = +0.50$ and $\chi_2 = -0.50$. The corresponding waveforms are exhibited in Fig. 15. One clearly sees the following facts. When the BHs are spinning in opposite directions, the waveform is essentially equivalent to the non-spinning one. This is due to the well known cancellation of the spin-orbit interaction in the equal mass case, with the little differences in the waveforms

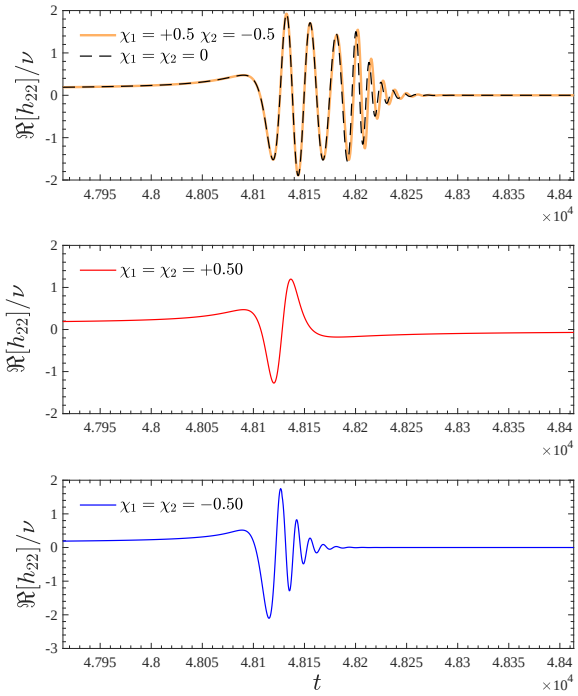

Figure 15: Effect of the spins on the $(q, E_0/M, p^0_\varphi) = (1, 1.0055, 3.97)$ configuration discussed above. Top panel: when χ_1 and χ_2 are anti-aligned among themselves, the spin-orbit interaction cancels out and the waveform is almost equivalent to the non-spinning one. Middle panel: the repulsive character of spin-orbit interaction for spins aligned with the angular momentum is such to have a scattering instead of a dynamical capture. Bottom panel: when spins are anti-aligned with the angular momentum, the system plunges faster, with a short burst of radiation corresponding to the final capture.

predominantly due to spin-spin effects [8]. To appreciate this at the level of dynamics, Fig. 16 shows that the potential energy $H^0_{\rm EOB}/M$ (i.e. Eq. (2) with $p_{r_*} = 0$) for $(\chi_1, \chi_2) = (+0.50, -0.50)$ is visually indistinguishable from the non-spinning one. When the spins are both aligned with the orbital angular momentum, the centrifugal barrier is higher than in the non-spinning case (compare black and red lines in Fig. 16, and thus the system undergoes a scattering instead of a capture. The corresponding,

[8]For completeness, some of the waveform differences also come from the merger-ringdown modelization, that is spin-dependent.

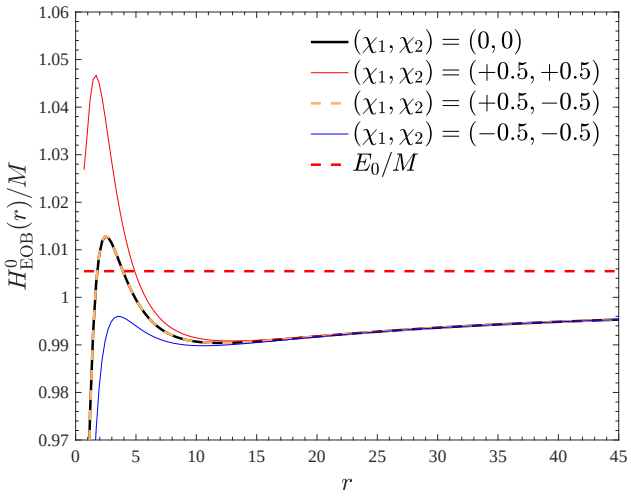

Figure 16: Potential energy $H_0^{\rm EOB}(r)/M$ for the four configurations shown in Fig. 15, that share the same $p_\varphi^0 = 3.97$ but have different values of the spins. The horizontal line corresponds to $E_0/M = 1.0055$. The larger centrifugal barrier present when $\chi_1 = \chi_2 = +0.5$ is responsible of the scattering behavior in the middle panel of Fig. 15. In addition, the case $(\chi_1, \chi_2) = (+0.50, -0.50)$ is extremely close to $(\chi_1, \chi_2) = 0$ because of spin-orbit coupling cancellation, consistently with the waveform shown in the top panel of Fig. 15.

burst-like, waveform is shown in the middle panel of Fig. 15. Finally, when spins are both anti-aligned with the orbital angular momentum, the spin-orbit interaction makes the attraction stronger than the non-spinning case (i.e. the potential barrier is much lower, see blue curve in Fig. 16) and the system plunges faster, with a signal whose pre-ringdown phase is much shorter than the non-spinning case.

5.1.2 Higher modes

Higher modes are incorporated in both the latest quasi-circular and eccentric realizations of `TEOBResumS` [195, 196, 170]. In the non-spinning case, all modes up to $\ell = m = 5$ included are robustly completed by the NR-informed, quasi-circular, merger and ringdown part [195]. By contrast, in the spinning case, due

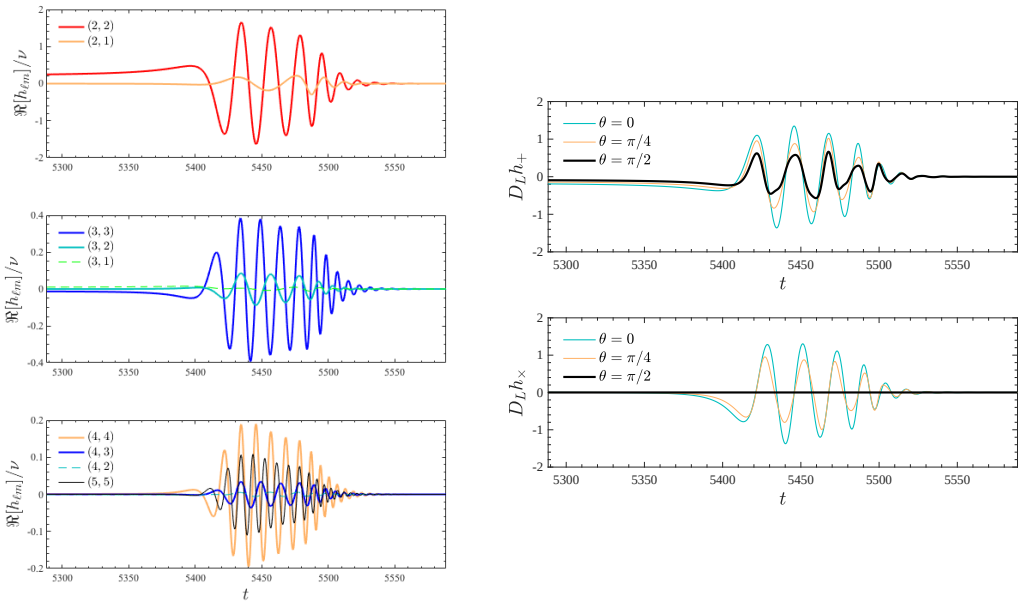

Figure 17: Calculation of higher modes for a non-spinning configuration with $(q, E_0/M, p_\varphi^0) = (3.5, 1.0067, 4.1361)$. The phenomenology is qualitatively analogous to the $(q, E_0/M, p_\varphi^0) = (1, 1.0055, 3.97)$ case shown in Fig. 9 above. $D_L h_+$ and $D_L h_\times$ waveform polarizations for $(q, E_0/M, p_\varphi^0) = (3.5, 1.0067, 4.1361)$ at various inclinations: $\theta = 0$ (face on), $\theta = \pi/4$ and $\theta = \pi/2$ (edge on).

to numerical noise in the NR data, it was not possible to model the postmerger-ringdown part in modes modes like $(3, 1)$, $(4, 2)$ and $(4, 1)$ (see [196]). Figure 17 shows, in the first three rows, several multipoles for $(q, E_0/M, p_\varphi^0) = (3.5, 1.0067, 4.1361)$. For this choice of initial conditions, the system undergoes a quasi-circular orbit before plunge and merger, analogously to the corresponding $q = 1$ case shown above in the middle panel of Fig. 9. One can appreciate that all modes can be obtained robustly with the standard ringdown matching procedure discussed in Refs. [195, 196]. For visual completeness, the last two rows of the figure also show the corresponding two polarizations $(h_+, h_\times)$

for various inclinations.

5.2 EOB/NR scattering angle: the equal-mass case

So far, we have investigated the analytical predictions of our EOB model for dynamical capture under the assumption that it provides a reasonably faithful representation of true signals. Evidently, given the many approximations adopted to construct the model, a proof of this statement can only come from a systematic analysis of NR simulations of dynamical captures. Unfortunately, such NR simulations are currently not available. Despite this, we can actually test our model using some NR computation of the scattering angle previously published in Ref. [247]. The scattering angle, χ, is the natural, gauge-invariant, observable that is used to characterize hyperbolic encounters. Reference [247] provided the first measurement of χ from NR simulations and its comparison with an EOB prediction. The work of Ref. [247] was a very preliminary investigation of a new territory and thus was limited to only $q = 1$ binaries. Moreover, the EOB calculation of scattering angles of Ref. [247] was not EOB-self consistent, since it was relying on energy and angular momentum losses computed from NR simulations. In this respect, Ref. [247] allowed for a detailed analysis of the properties of the EOB Hamiltonian, but not of the full dynamical model. Now, thanks to the improved radiation reaction of Ref. [170], reliable in the strong field, we can finally go beyond the approach of [247] and explore the reliability of the *full* model in hyperbolic encounters. This will allow us to put on a more solid ground the results discussed above. Reference [247] considered 10 configurations, specified by Arnowitt-Deser-Misner (ADM) energy and angular momentum, of $q = 1$ non-spinning BH binaries. Each configuration was then evolved numerically. The initial data were chosen so as to always have a scattering and not a capture.

Table 2: EOB scattering angle and comparison with the NR data of Ref. [247]. These results correspond to the standard configuration of the model, i.e. with 3PN-accurate D and Q functions. From left to right, the columns report: the configuration number; the minimum EOB radial separation; the NR initial energy E^0/M and angular momentum J^0/M^2; the NR and EOB energy losses; the NR and EOB angular momentum losses; the NR and EOB scattering angles and their fractional difference $\hat{\Delta}\chi \equiv |\chi^{\rm NR} - \chi^{\rm EOB}|/\chi^{\rm NR}$. Angles are measured in degrees. Note that, within the EOB, configuration #1 does not scatter, but plunges instead.

#	$r_{\rm min}$	E^0/M	J^0/M^2	$\Delta E^{\rm NR}/M$	$\Delta E^{\rm EOB}/M$	$\Delta J^{\rm NR}/M^2$	$\Delta J^{\rm EOB}/M^2$	$\chi^{\rm NR}$	$\chi^{\rm EOB}$	$\hat{\Delta}\chi[\%]$
1	...	1.0225555(50)	1.099652(36)	0.01946(17)	0.032553	0.17007(89)	0.363750	305.8 (2.6)	...	...
2	3.70	1.0225722(50)	1.122598(37)	0.01407(10)	0.014083	0.1380(14)	0.134495	253.0(1.4)	279.35	10.4
3	4.03	1.0225791(50)	1.145523(38)	0.010734(75)	0.00951037	0.1164(14)	0.101919	222.9(1.7)	234.22	5.1
4	4.85	1.0225870(50)	1.214273(40)	0.005644(38)	0.0041582	0.076920(80)	0.0588254	172.0(1.4)	174.23	1.3
5	5.34	1.0225870(50)	1.260098(41)	0.003995(27)	0.00272826	0.06163(53)	0.045189	152.0(1.3)	153.01	0.7
6	6.49	1.0225884(50)	1.374658(45)	0.001980(13)	0.001172	0.04022(53)	0.027481	120.7(1.5)	120.79	0.07
7	7.59	1.0225924(50)	1.489217(48)	0.0011337(90)	0.0005951	0.029533(53)	0.018992	101.6(1.7)	101.51	0.09
8	8.66	1.0225931(50)	1.603774(52)	0.007108(77)	0.000332568	0.02325(47)	0.0141277	88.3(1.8)	88.19	0.12
9	9.72	1.0225938(50)	1.718331(55)	0.0004753(75)	0.00019778	0.01914(76)	0.0110359	78.4(1.8)	78.28	0.15
10	10.78	1.0225932(50)	1.832883(58)	0.0003338(77)	0.0001226	0.0162(11)	0.008928	70.7(1.9)	70.54	0.23

Details of the NR simulations are reported in Table I of [247]. The values of the dimensionless initial ADM energy E^0/M and dimensionless initial angular momentum J^0/M^2 (with the relative errors) are reported in the third and fourth columns of Table 2. The ninth column of the table collects the values of the NR scattering angle, with their uncertainty, as published in Ref. [247]. As above, the initial EOB separation is chosen to be $r_0 = 10000$. The EOB values of the scattering angles are listed in the tenth column of the table, while the last one lists fractional NR/EOB difference, $\hat{\Delta}\chi \equiv |\chi^{\rm NR} - \chi^{\rm EOB}|/\chi^{\rm NR}$. A few comments are in order: (i) the EOB/NR agreement between scattering angles is of the order of or below 1% fractional difference except for three outliers that correspond, not surprisingly, to the smallest values of the impact parameter, although such fractional difference is within the NR uncertainty; (ii) for the first three configurations, the EOB model systematically overestimates the scattering angle, indicating that the system tends to be trapped and eventually plunge, instead of scatter away. This is indeed what happens for configuration #1, where the system does a first close encounter, followed by a second one and the plunge.

Qualitatively speaking, this behavior is just mirroring the fact that the gravitational attraction as modeled within the EOB model is *stronger* than the actual NR prediction. At a more quantitative level, it is difficult to precisely quantify to which extent this is due to the conservative or nonconservative part of the dynamics. For what concerns the GW losses, columns 5-8 of Table 2 compare the total fraction of energy and angular momentum emitted in the NR simulation with the same quantity computed within the EOB formalism. This is what is accounted by the analytical fluxes entering the r.h.s. of Hamilton's equation. The analytical fluxes are found to always underestimate the numerical ones (sometimes also by $\sim 50\%$), except for con-

figuration #2. Despite this, the estimate of the scattering angle comes out consistent at a few percent level up to configuration #4, thus suggesting the crucial importance of the conservative part of the dynamics. We shall come back to this point in the next section.

5.2.1 Impact of beyond 3PN corrections in the Q and D EOB potentials

To have a deeper understanding of the results obtained above, let us first remember that Ref. [247] showed that the best EOB/NR agreement was obtained by using a D function at (incomplete) 4PN, that was taking into account only the linear-in-ν contributions available at the time [249]. Now that the 4PN knowledge of the Hamiltonian is complete [250, 251], the 5PN information is complete except for two undetermined numerical parameters, $\bar{d}_5^{\nu^2}$ and $a_6^{\nu^2}$, and similarly the 6PN is known except for four undetermined numerical parameters, $(q_{45}^{\nu^2}, \bar{d}_6^{\nu^2}, a_7^{\nu^2}, a_7^{\nu^3})$ [136, 137], it is worth to revive and improve the comparison of Ref. [247]. Note however that we do this here using the full model with radiation reaction and taking into account the contributions to either the D and the Q functions (while Ref. [247] was just using the 3PN-accurate Q). In principle, we should also explore, within the present context, the effect of higher PN corrections to the A function. However, we decided not to do so now for the following two reasons. On the one hand, the analytically known numerical value of the 5PN correction to the potential a_6^c is such that the usual $(1,5)$ Padé approximant has a spurious pole, making thus this additional analytical knowledge practically useless within the current EOB context. Exploring different resummation strategies (e.g. changing Padé approximant) would be necessary in order to fruitfully use the analytically known 5PN result. On the other hand, we have verified that even large changes ($\sim 100\%$) of the NR-informed effective 5PN

parameter $a_6^c(\nu)$ obtained in Refs. [195, 196] and used here have little to negligible impact on the calculation of the scattering angle within the EOB model. This is consistent with the fact that the A function rules the azimuthal part of the energy and it is less important in a hyperbolic-like context when the radial part of the Hamiltonian, i.e. $\propto p_{r_*}^2$ becomes predominant. To avoid additional complications we thus prefer to keep working with the NR-informed expression of the A function used in previous work, focusing instead only on the high-PN corrections to the Q and D functions.

Q function Let us start discussing the Q function. To simplify the logic, we keep D fixed at 3PN order and consider only Q at 4PN and at 5PN, though incorporating only local terms. The result of the χ computation is displayed in Table 3. One sees that the 4PN terms bring a small, though significative, contribution to the scattering angle that goes in the direction of reducing the EOB/NR difference. Despite this, the magnitude of the correction is too small to avoid configuration #1 to plunge. By contrast, the effect of the 5PN local-in-time terms goes in the wrong direction and, moreover, is significantly smaller than the numerical uncertainty. At a practical level, and especially in view of the analytic complexity of the Q function at 6PN, we don't think it is worth, for the current study, to push Q at 6PN accuracy and we shall just work, from now on, at 4PN accuracy in Q.

D function Now that we have explored the (ir)relevance of the various PN truncations of the Q function, let us move to exploring the D function. We consider all terms up to 6PN, i.e. separately work with 4PN, 5PN and 6PN truncations, keeping the accuracy of Q fixed at 4PN. Each D function, that comes as a PN-truncated series, is resummed. Let us write here, for

Table 3: Impact of 4PN and 5PN terms in the Q function on the calculation of the scattering angle χ. Angles are measured in degrees.

#	$\chi^{\rm NR}$	$\chi^{\rm EOB}_{Q_{\rm 3PN}}$	$\chi^{\rm EOB}_{Q_{\rm 4PN}}$	$\chi^{\rm EOB}_{Q_{\rm 5PN}}$
1	305.8(2.6)	...	...	...
2	253.0(1.4)	279.35	278.21	278.75
3	222.9(1.7)	234.22	233.27	233.62
4	172.0(1.4)	174.23	173.57	173.72
5	152.0(1.3)	153.01	152.47	152.57
6	120.7(1.5)	120.79	120.44	120.49
7	101.6(1.7)	101.51	101.28	101.29
8	88.3(1.8)	88.19	88.03	88.04
9	78.4(1.8)	78.28	78.16	78.17
10	70.7(1.9)	70.54	70.44	70.45

Table 4: EOB scattering angle obtained using both D and Q functions and 4PN. The EOB/NR agreement is improved with respect to the standard case of Table 2 that adopt 3PN accuracy for these functions. Note that configuration #1 does not plunge anymore.

#	$r_{\rm min}$	$\Delta E^{\rm EOB}/M$	$\Delta J^{\rm EOB}/M^2$	$\chi^{\rm NR}$	$\chi^{\rm EOB}$	$\hat{\Delta}\chi$ [%]
1	3.31	0.022693	0.190585	305.8	381.93	24.89
2	3.71	0.012995	0.126256	253.0	264.21	4.43
3	4.03	0.008920	0.097128	222.9	225.12	0.99
4	4.85	0.003997	0.057269	172.0	170.53	0.85
5	5.34	0.002646	0.044311	152.0	150.60	0.92
6	6.49	0.001151	0.027202	120.7	119.72	0.81
7	7.59	0.000588	0.018878	101.6	100.93	0.66
8	8.66	0.000330	0.014074	88.3	87.85	0.51
9	9.72	0.000196	0.011008	78.4	78.05	0.44
10	10.78	0.000122	0.008912	70.7	70.38	0.45

Table 5: EOB scattering angle computed using Q at 4PN and D at 5PN, though resummed with a $(1,4)$ Padé approximant since P_5^0 develops a spurious pole. The EOB/NR agreement is worsened with respect to Table 4 and configuration #1 plunges again. See text for discussion.

#	$r_{\rm min}$	$\Delta E^{\rm EOB}/M$	$\Delta J^{\rm EOB}/M^2$	$\chi^{\rm NR}$	$\chi^{\rm EOB}$	$\hat{\Delta}\chi$ [%]
1	...	0.031705	0.347309	305.8	...	...
2	3.71	0.013463	0.129751	253.0	270.26	6.82
3	4.03	0.009161	0.099057	222.9	228.48	2.50
4	4.85	0.004054	0.057809	172.0	171.63	0.22
5	5.34	0.002673	0.044589	152.0	151.22	0.51
6	6.49	0.001157	0.027273	120.7	119.92	0.65
7	7.59	0.000590	0.018901	101.6	101.01	0.58
8	8.66	0.000330	0.014083	88.3	87.88	0.47
9	9.72	0.000197	0.011012	78.4	78.07	0.42
10	10.78	0.000122	0.008914	70.7	70.39	0.44

Table 6: EOB scattering angle computed using D function at 6PN and the Q function at 4PN [135, 136]. The 6PN-accurate D function is essential to get an improved EOB/NR agreement for small values of the EOB impact parameter. Note, however, that this also brings slightly larger deviations with respect to the previous cases for intermediate values of $r_{\rm min}$.

#	$r_{\rm min}$	$\Delta E^{\rm EOB}/M$	$\Delta J^{\rm EOB}/M^2$	$\chi^{\rm NR}$	$\chi^{\rm EOB}$	$\hat{\Delta}\chi$ [%]
1	3.33	0.015559	0.141465	305.8	274.68	10.18
2	3.71	0.010137	0.105088	253.0	228.49	9.69
3	4.03	0.007422	0.085263	222.9	204.52	8.24
4	4.85	0.003654	0.054047	172.0	163.99	4.66
5	5.34	0.002490	0.042707	152.0	146.99	3.30
6	6.49	0.001121	0.026816	120.7	118.63	1.71
7	7.59	0.000580	0.018755	101.6	100.51	1.07
8	8.66	0.000327	0.014027	88.3	87.66	0.72
9	9.72	0.000195	0.010987	78.4	77.96	0.56
10	10.78	0.000122	0.008902	70.7	70.33	0.52

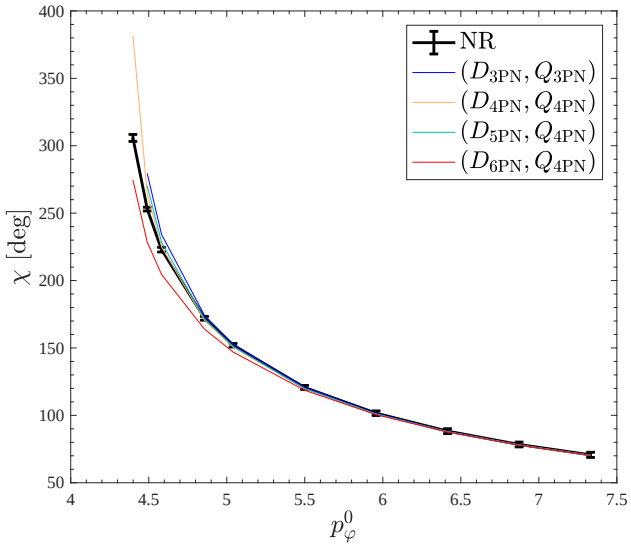

Figure 18: Comparing the NR scattering angles with various EOB predictions using different PN accuracies of the (Q, D) potential. The 6PN-accurate D function allows for the closest EOB/NR agreement for the smallest values of the EOB impact parameter.

completeness, the Taylor expansion of D up to 6PN

$$D^{\mathrm{Taylor}}_{6\mathrm{PN}} = 1 - 6\nu u^2 - (52\nu - 6\nu^2)u^3 + \nu\, d_4 u^4 + \\ + \nu\, d_5 u^5 + \nu\, d_{5.5} u^{11/2} + \nu\, d_6 u^6. \tag{135}$$

The standard resummation procedure for this function is to take a P^0_n approximant of this equation. This approach is now so standard that any analytical result is usually given in terms of the inverse function $\bar{D} \equiv 1/D$ (see e.g. Refs. [134, 135, 136, 137]). The coefficients $(d_4, d_5, d_{5.5}, d_6)$ in Eq. (135) are obtained by just expanding $1/\bar{D}$ as given in the literature. One finds that the 5PN D function resummed taking the $(0, 5)$ Padé approximant has a spurious pole around $u \approx 0.5$ and thus it cannot be used robustly to deliver analytical predictions. That is the reason why we prefer to give the results of Refs. [134, 135, 136, 137] in terms of the D function in Eq. (135) and then, at 5PN accuracy, proceed by resumming it with a $(1, 4)$ Padé approximant,

that is $D_{5\rm PN} = P_4^1 \left[D_{5\rm PN}^{\rm Taylor} \right]$, that is found to have a pole-free behavior. The results of the calculations of the scattering angle with higher PN knowledge in D are listed in Tables 4-6, while a visual representation can be found in Fig. 18. The following conclusions are in order: (i) increasing the analytic information of D to 4PN brings the first, important, qualitative and quantitative improvement, since configuration #1 is found to correctly scatter (though the scattering angle is still significantly larger than the NR one) instead of plunging; (ii) moving to 5PN is a step back, since configuration #1 plunges again. By contrast, (iii), a certain improvement is obtained working at 6PN, retaining all the currently unknown numerical parameters fixed to zero. For the smallest impact parameters, the EOB/NR difference is at most of the order of 10%, an improvement of more than a factor two with respect to the cases discussed above. One also notes, however, that for intermediate values of the EOB impact parameter the EOB/NR agreement is slightly worse than, for instance, the $(D_{4\rm PN}, Q_{4\rm PN})$ case. It should keep in mind that these conclusions rely on *yet incomplete* 5PN and 6PN knowledge and may change once these calculations will be completed.

It is useful to visualize the functional behavior of the resummed D function for the various PN orders considered above, see Fig. 19. The effect of higher PN order is to reduce the magnitude of the D potential for $u \gtrsim 0.15$, i.e. $r \lesssim 7$. This is indeed the regime of radii explored by configurations $\#1 - \#7$. The figure then indicates that the D function that best approximates the NR values of the scattering angle (within the current analytical framework) should be slightly larger than the analytically known 6PN one, starting from $u \approx 0.18$. Still, it has to stay well below the 4PN curve. Although our finding is rather interesting because it demonstrates that, by varying a single analytical element, one can progressively improve

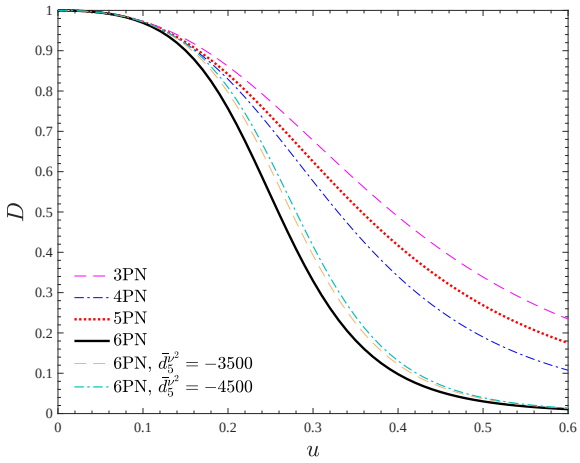

Figure 19: The resummed D function for $q = 1$ at various PN orders. The function gets progressively steeper as the PN order is increased. The orange lines corresponds to the *flexed* 6PN function where we put $d_5^{\nu^2} = -3500$ (dashed) and $d_5^{\nu^2} = -4500$ (dash-dotted). This latter brings the EOB/NR agreement of the order of percent for any configuration considered. See Table 7 and additional discussion in text.

the EOB/NR agreement of the scattering angle, it is not yet satisfactory because the difference is still larger than the NR error bar. It is then reasonable to ask whether it is possible to effectively *flex* the current $D_{\rm 6PN}$ so as to further improve the EOB/NR agreement for the smallest values of $r_{\rm min}$. As noted above $D_{\rm 6PN}$ is analytically known modulo three parameters, $(a_6^{\nu^2}, \bar{d}_5^{\nu^2}, \bar{d}_6^{\nu^2})$. We found that changing only $\bar{d}_5^{\nu^2}$ gives us enough flexibility for our aim. Figure 19 exhibits, with a orange line, the curve corresponding to $\bar{d}_5^{\nu^2} = -3500$. This value of the parameter was determined so to provide an EOB/NR agreement below the percent level for the smallest values of the impact parameter, as shown in Table 7. One should however note that for half of the configurations, the EOB/NR difference is still *larger* than the NR error bar, that is always of the order of percent or smaller. One then verifies that $\bar{d}_5^{\nu^2} = -4500$ allows one to obtain values of $\hat{\Delta}\chi = (2.52, 2.07, 2.57, 1.73, 1.13)\%$

Table 7: Tuned D potential with $\bar{d}_5^{\nu^2} = -3500$. This number is chosen so to have an excellent EOB/NR agreement for configuration #1. Still, for half of the configurations the EOB/NR difference is slightly larger than the NR error bar. See text for additional discussion.

#	$r_{\rm min}$	$\Delta E^{\rm EOB}/M$	$\Delta J^{\rm EOB}/M^2$	$\chi^{\rm NR}$	$\chi^{\rm EOB}$	$\hat{\Delta}\chi[\%]$
1	3.32	0.017860	0.157308	305.8	303.17	0.86
2	3.71	0.011289	0.113663	253.0	243.02	3.9
3	4.03	0.008109	0.090735	222.9	214.15	3.9
4	4.85	0.003853	0.055929	172.0	167.87	2.4
5	5.34	0.002591	0.043749	152.0	149.36	1.7
6	6.49	0.001145	0.027120	120.7	119.50	0.10
7	7.59	0.000587	0.018867	101.6	100.89	0.69
8	8.66	0.000330	0.014075	88.3	87.85	0.51
9	9.72	0.000197	0.011010	78.4	78.06	0.43
10	10.78	0.000122	0.008914	70.7	70.39	0.44

for the first five configurations, and below 1% for the following ones, i.e. $\hat{\Delta}\chi = (0.79, 0.59, 0.45, 0.39, 0.41)\%$. One should note, however, that $\chi^{\rm EOB}_{\#1} = 313.51$, i.e. it is now *larger* than the NR value. The curve with $\bar{d}_5^{\nu^2} = -4500$ is also shown on Fig. 19 for completeness. Evidently, seen the still large errors in the NR computations, that date back to a few years ago, the various approximations involved in our analytical model (notably, the radiation reaction) and various possibilities of tuning free parameters, we do not want to make any strong claim about the physical meaning to the NR-tuning of $\bar{d}_5^{\nu^2}$. Still, our exercise shows that there is a large amount of yet unexplored analytical flexibility within the EOB model that can be constrained using the NR knowledge of the scattering angle, as originally advocated in Ref. [247].

As an additional exploratory study, we show in Fig. 20 how would change the waveform for $(q, E_0/M, p^0_\varphi) = (8, 1.0003, 4.3142)$ of Fig. 12 when we replace $(D_{\rm 3PN}, Q_{\rm 3PN})$ with $(D_{\rm 6PN}, Q_{\rm 4PN})$. The less attractive character of $D_{\rm 6PN}$, as discussed above, re-

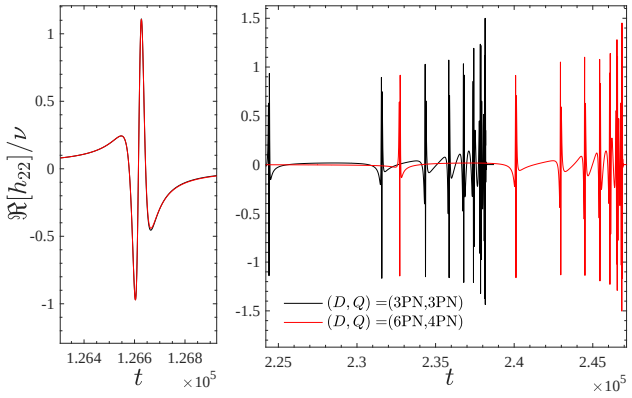

Figure 20: Waveforms for configuration with $(q, E_0/M, p^0_\varphi) = (8, 1.0003, 4.3142)$ considered in Figures. 12 and 13 with (D, Q) at 3PN (resummed) accuracy contrasted with the analytical prediction obtained with D at 6PN and Q at 4PN. The left panel compares the waveforms during the first encounter; the right panel the subsequent periastron passages, up to the final merger. The phenomenology is qualitatively the same, but the less attractive character of $D_{6\mathrm{PN}}$ with respect to $D_{3\mathrm{PN}}$ results in a larger time-lag between one encounter and the other and in a waveform that is globally almost twice longer.

sults in a larger time-lag between the various bursts after the first encounter and the waveform is almost twice longer than with $D_{3\mathrm{PN}}$ case. We conclude that there is a urgent need of specifically tuned NR simulations of dynamical capture BH binaries aiming at understanding to which extent the analytical elements entering our model are trustable and what needs to be changed in order to achieve a level of NR-faithfulness sufficient for parameter-estimation purposes.

5.3 Summary

We presented an extension of `TEOBResumS` able to describe the dynamics of spin-aligned BBH hyperbolic encounters and the emitted gravitational waveform. The dynamics includes radiation reaction and multipolar waveforms for BBH with arbitrary

mass ratio and aligned-spin interactions.

We have extensively explored the parameter space of non-spinning dynamical captures, parameterizing it in terms of initial energy and angular momentum. In particular, we have characterized various regions on the basis of the number of close encounters that happen before merger, that are measured looking at the number of peak of the orbital frequency. We have found that the region of parameter space with two peaks, i.e. an encounter followed by the merger, gets smaller and smaller as the mass ratio increases. By contrast, the number of encounters before merger in the special region close to the stability regime increases with the mass ratio. The dynamical behavior is mirrored in the waveform, that is completed with a merger and ringdown part informed by quasi-circular NR-simulation.

We have briefly explored the effect of spin, in order to get a qualitative idea of the general behavior. When spin are aligned with respect to the orbital angular momentum, a capture that is present in the non-spinning case, may transform in scattering if the spin-orbit interaction is sufficiently strong. By contrast, spins anti-aligned with the orbital angular momentum accelerate the capture process, so that the corresponding waveform eventually ends up with less gravitational wave cycles, and is dominated by the final ringdown part.

Beyond the need, for GW-data purposes, of providing an analytical description of the dynamics and radiation of relativistic hyperbolic encounters, we have refreshed the EOB/NR comparison between scattering angles χ that was pioneered in Ref. [247]. Two are our most relevant findings. On the one hand, working with the D function at 3PN, i.e. exactly with the eccentric EOB model of Ref. [170], we showed that an EOB-self-consistent calculation of the scattering angle (that is, including radiation reaction) is well compatible with the NR results of Ref. [247], although things become quantitatively and qualitatively differ-

ent (i.e. plunge instead of scattering) for the smallest value of the EOB impact parameter. On the other hand, we have systematically explored the impact of 4PN, 5PN and 6PN corrections to the D function. Our most important finding is that the recently computed, 6PN-accurate, D function allows one to obtain an EOB/NR agreement for the scattering angle of a few percent *also* for the configurations with the smallest impact parameter. We thus argue that our model for hyperbolic scattering/dynamical capture is, probably, more accurate using $D_{6\mathrm{PN}}$ instead of $D_{3\mathrm{PN}}$. Due to the absence of additional NR simulations, we take the difference between $D_{3\mathrm{PN}}$ and $D_{6\mathrm{PN}}$ results as a (rather conservative) error bar that might be taken into account, using the current model, in a possible parameter estimation on a GW detection qualitatively and morphologically compatible with a dynamical capture scenario. We have also shown that it is rather easy to additionally tune the $D_{6\mathrm{PN}}$ function so as to further improve the EOB/NR agreement of the scattering angle, at the level of the actual estimate of the uncertainty on the NR scattering angle. This is done by tuning only the uncalculated 5PN numerical parameter $\bar{d}_5^{\nu^2}$. Concretely, our results indicate that, one the one hand, it would be a good idea to incorporate the 6PN-accurate D function in waveform model for quasi-circular coalescing BBHs; on the other hand, it proves that NR simulations of the scattering angle can be used to *inform* the EOB model and thus dedicated NR simulations to systematically and usefully explore the parameter space should be performed at some stage. Similarly, systematic NR surveys of dynamical captures are needed to test our model and to improve the merger-ringdown part, that at the moment is informed by quasi-circular simulations.

6 Impact of high-order analytical information on a generic-orbit EOB model

A lot of effort has been put into the construction of accurate waveform model for *noncircularized* coalescing BBHs [252, 253, 170, 254, 171, 172, 207, 208, 173, 174, 208, 255]. Eccentric waveform models are needed in order to correctly analyse GW signals from non-circular systems detected by current and (especially) future GW detectors [256, 257, 237]. At the same time, hyperbolic models will be useful to discern highly precessing systems from dynamical captures and head-on collisions, as they can have a very similar morphology [209, 242, 243, 258].

As we saw in last section, EOB-NR models are flexible enough to model all these different scenarios. Typically, however, different resummations and NR-informed parameters are implemented, so that the eccentric or hyperbolic model is not as accurate when used to generate quasi-circular waveforms. This is the case for `TEOBResumS`, whose eccentric implementation [170, 171] in the quasicircular limit is considerably *less accurate* (EOB/NR unfaithfulness $\simeq 1\%$) than the native quasi-circular model `TEOBResumS` [196, 178] (EOB/NR unfaithfulness $\simeq 0.1\%$).

We hence try and build an updated `TEOBResumS` designed to deal with any orbital configuration, so that EOB/NR agreement is satisfactory for quasi-circular, eccentric and hyperbolic simulations. In doing so, we will implement newly computed 5PN-accurate information [134, 135] in the EOB potentials (D, Q); contributions up to 4PN (NNLO) in the spin-spin sector [223, 259]; and (next-to)^3-leading order (N^{3}LO) terms in the spin-orbit one [154, 138]. We will also need to change the resummation choices that have been shared by all realizations of `TEOBResumS` up to now.

The contents of this section were originally published as "A. Nagar and P. Rettegno, *Phys. Rev. D* **104** 104004 (2021)" [260].

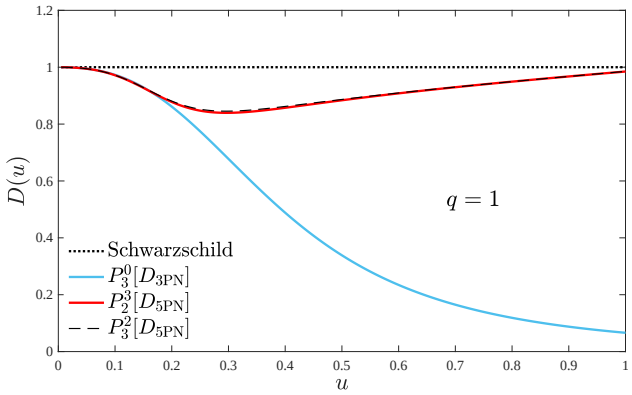

Figure 21: Comparison between different realizations of the D function for $q = 1$: the $P_3^0[D_{3\mathrm{PN}}]$ used in the standard implementation of `TEOBResumS` (blue online). Since the $P_5^0[D_{5\mathrm{PN}}]$ develops a spurious pole for $0 < u < 1$, we plot instead $P_2^3[D_{5\mathrm{PN}}]$ and $P_3^2[D_{5\mathrm{PN}}]$, that are almost identical. However, the latter develops a spurious pole well outside the domain (around $u \sim 8$). Note that both approximants are quantitatively consistent with the Schwarzschild potential, $D = 1$ (dotted line). We choose the $P_2^3[D_{5\mathrm{PN}}]$ Padé approximant to represent the D function.

6.1 EOB dynamics with 5PN terms

6.1.1 The EOB potentials

Within the EOB Hamiltonian, the A and D potentials are resummed PN series. Their Taylor expanded expressions read

$$
\begin{aligned}
A_{5\mathrm{PN}}(u) = 1 - 2u + 2\nu\, u^3 + \nu \left(\frac{94}{3} - \frac{41\pi^2}{32}\right) u^4 + \\
+ \left[\left(\frac{2275\pi^2}{512} - \frac{4237}{60} + \frac{128}{5}\gamma_{\mathrm{E}} + \frac{256}{5}\ln(2)\right)\nu + \right. \\
\left. + \left(\frac{41\pi^2}{32} - \frac{221}{6}\right)\nu^2 + \frac{64}{5}\nu\,\ln(u)\right] u^5 + \\
+ \nu \left[a_6^c + \left(-\frac{7004}{105} - \frac{144}{5}\nu\right)\ln(u)\right] u^6,
\end{aligned}
\tag{136}
$$

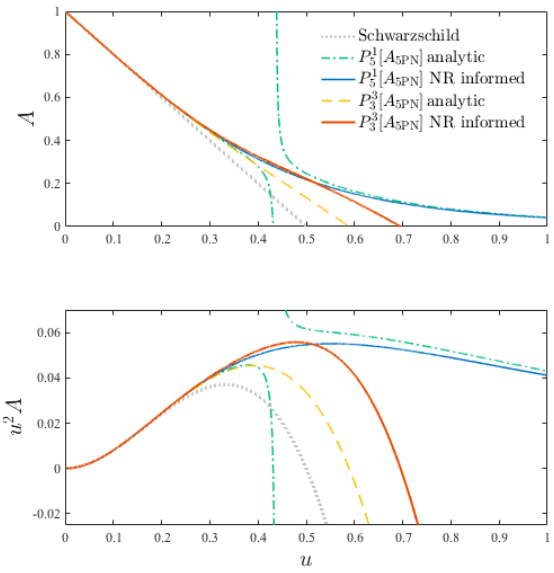

Figure 22: Comparison between different A functions (top panel) and effective photon potentials, u^2A (bottom panel) for $q = 1$. The grey dotted line represents the Schwarzschild equivalent functions. The picture highlights that the commonly used $P^1_5[A]$ approximant develops an unphysical pole when $a^c_6 = a^c_{6\rm anlyt}$ from Eq. (138). One also notices the consistency between the two NR-informed A functions up to the effective light-ring, i.e. the peak of the function u^2A. Note however that the difference between the potentials around $u \simeq 0.4$ is $\sim 10^{-2}$, so that they do actually yield different EOB dynamics.

$$
\begin{aligned}
D_{5\rm PN}(u) = 1 &- 6\nu\, u^2 - \left(52\nu - 6\nu^2\right) u^3 + \\
&+ \left[\left(\frac{533}{45} + \frac{23761\pi^2}{1536} - \frac{1184}{15}\gamma_{\rm E} + \frac{6496}{15}\ln(2) - \frac{2916}{5}\ln(3) \right)\nu + \right. \\
&\left. + \left(-\frac{123\pi^2}{16} + 296 \right)\nu^2 - \frac{592}{15}\nu\ln(u) \right] u^4 + \\
&+ \left[\left(-\frac{294464}{175} + \frac{63707\pi^2}{512} + \frac{2840}{7}\gamma_{\rm E} - \frac{120648}{35}\ln(2) + \frac{19683}{7}\ln(3) \right)\nu + \right. \\
&\quad + \left(-d_5^{\nu^2} - \frac{2216}{105} + \frac{6784}{15}\gamma_{\rm E} + \frac{326656}{21}\ln(2) - \frac{58320}{7}\ln(3) \right)\nu^2 + \\
&\quad \left. + \left(-\frac{1285}{3} + \frac{205\pi^2}{16} \right)\nu^3 + \left(\frac{1420}{7}\nu + \frac{3392}{15}\nu^2 \right)\ln(u) \right] u^5, \quad (137)
\end{aligned}
$$

where $\gamma_E = 0.577216\ldots$ and we kept implicit the coefficient $a_6^c(\nu)$. Its analytically known expression reads [249, 131, 250, 251]

$$
\begin{aligned}
a^c_{6\,\mathrm{anlyt}}(\nu) = &-\frac{1066621}{1575} + \frac{246367\pi^2}{3072} + \\
&- \frac{14008}{105}\gamma_{\mathrm{E}} - \frac{31736}{105}\ln(2) + \frac{243}{7}\ln(3) + \\
&+ \left(\frac{64}{5} - \frac{288}{5}\gamma_{\mathrm{E}} + \frac{928}{35}\ln(2) - \frac{972}{7}\ln(3) + a_6^{\nu^2}\right)\nu + 4\nu^2 .
\end{aligned}
\tag{138}
$$

Note that both Eq. (137) and (138) present two yet undetermined analytical coefficients, $(a_6^{\nu^2}, d_5^{\nu^2})$. For simplicity, in this work we impose $d_5^{\nu^2} = 0$. By contrast, following previous works, we will not use the analytical expression $a^c_{6\,\mathrm{anlyt}}(\nu)$, but rather consider $a_6^c(\nu)$ as an undetermined function of ν that is informed using NR simulations. The differences between the resulting NR-informed A function and the one that uses $a^c_{6\,\mathrm{anlyt}}(\nu)$ will be discussed below. The Q function at 5PN accuracy was obtained in Ref. [135]. For simplicity, here we only consider the *local* part of Q at 5PN [9]. Once p_r is rewritten in terms of p_{r_*}, the function

[9] We have also attempted to incorporate the nonlocal part, but the expression is rather complicated and it seems to degrade the robustness of the model in strong field.

reads

$$
\begin{aligned}
Q_{\rm 5PNloc}(u,p_{r_*}) = {}& 2(4-3\nu)\nu\, u^2 p_{r_*}^4 + \\
&+\left[\left(-\frac{4348}{15}+\frac{496256}{45}\ln(2)-\frac{33048}{5}\ln(3)\right)\nu - 131\nu^2+10\nu^3\right] u^3 p_{r_*}^4 + \\
&+\left[\left(-\frac{827}{3}-\frac{2358912}{25}\ln(2)+\frac{1399437}{50}\ln(3)+\frac{390625}{18}\ln(5)\right)\nu + \right. \\
&\quad \left. -\frac{27}{5}\nu^2+6\nu^3\right] u^2 p_{r_*}^6 + \\
&+\left[\left(-\frac{32957}{10}-\frac{28306944}{25}\ln(2)+\frac{8396622}{25}\ln(3)+\frac{781250}{3}\ln(5)\right)\nu + \right. \\
&\quad \left. -\frac{393}{5}\nu^2+188\nu^3-14\nu^4\right] u^3 p_{r_*}^6 + \\
&+\left[\left(-\frac{6328799}{3150}-\frac{93031\pi^2}{1536}+\frac{3970048}{45}\ln(2)-\frac{264384}{5}\ln(3)\right)\nu + \right. \\
&\quad \left. +\left(-\frac{5075}{3}+\frac{31633\pi^2}{512}\right)\nu^2+\left(792-\frac{615\pi^2}{32}\right)\nu^3\right] u^4 p_{r_*}^4 + \\
&+\left(\frac{6}{7}\nu+\frac{18}{7}\nu^2+\frac{24}{7}\nu^3-6\nu^4\right) u^2 p_{r_*}^8 . \qquad (139)
\end{aligned}
$$

Here we will keep the function Q in its PN-expanded form. By contrast, both the (A,D) functions will be resummed using Padé approximants, although with different choices with respect to previous work. Within the `TEOBResumS` models, the formal 5PN-accurate A function is always resummed via a $(1,5)$ Padé approximant. As we will illustrate below, this approximant develops a spurious pole when $a_6^c = a_{6\rm anlyt}^c$. Since we also want to get a handle on the performance of the pure analytical information, we are forced to change the resummation choice. To do so, we follow the most straightforward approach and use the diagonal Padé approximant, that is

$$
A(u,\nu;a_6^c) = P_3^3[A_{\rm 5PN}(u,\nu;a_6^c)], \qquad (140)
$$

where it is intended that the $\ln(u)$ terms are treated as numerical constants when computing the Padé. x The 3PN-accurate D function, that in `TEOBResumS`, is resummed using a $(0,3)$ approximant. When the same is attempted with the 5PN-accurate function (with $d_5^{\nu^2} = 0$), spurious poles again show up for any value of ν. By contrast, the quasi-diagonal Padé approximants P_2^3 and P_3^2 stabilize the series: they are very similar to each other and generally consistent with the Schwarzschild value, $D_{\rm Schw} = 1$. Figure 21 highlights these facts for the case $q = 1$. Eventually, we choose to resum D as

$$D = P_2^3[D_{\rm 5PN}], \tag{141}$$

because the P_3^2 develops a spurious pole for large (even though unphysical, $u \sim 8$) values of ν. By contrast, for simplicity we use Q in its PN-expanded form.

6.1.2 The spin sector

When taking into account spinning bodies, the radial variable r is replaced, within $\hat{H}_{\rm eff}^{\rm orb}$, by the centrifugal radius r_c that is used to incorporate spin-spin terms [190]. Its explicit expression, that includes spin-spin terms up to NNLO, will be described in detail below.

For what regards the spin-orbit sector, the PN information enters the residual gyro-gravitomagnetic functions $\hat{G}_S$ and $\hat{G}_{S_*}$ (see Sec. 4.2 for details). These PN corrections are formally at N^{3}LO, corresponding to 4.5PN order in the following resummed form

$$\begin{aligned}\hat{G}_S = (1 &+ c_{10}u_c + c_{20}u_c^2 + c_{30}u_c^3 + c_{40}u_c^4 + c_{02}p_{r_*}^2 + c_{12}u_c p_{r_*}^2 + \\ &+ c_{04}p_{r_*}^4 + c_{22}p_{r_*}^2 u_c^2 + c_{14}u_c p_{r_*}^4 + c_{06}p_{r_*}^6)^{-1}, \end{aligned}\tag{142}$$

$$\begin{aligned}\hat{G}_{S_*} = (1 &+ c_{10}^* u_c + c_{20}^* u_c^2 + c_{30}^* u_c^3 + c_{40}^* u_c^4 + c_{02}^* p_{r_*}^2 + c_{12}^* u_c p_{r_*}^2 + \\ &+ c_{04}^* p_{r_*}^4 + c_{22}^* p_{r_*}^2 u_c^2 + c_{14}^* u_c p_{r_*}^4 + c_{06}^* p_{r_*}^6)^{-1}, \end{aligned}\tag{143}$$

where however we also have included two coefficients (c_{40}, c_{40}^*) that belong to the (next-to)^4-leading (N^{4}LO) order. Following previous work, we fix $c_{40} = 0$ and $c_{40}^* = 2835/256$. The second value comes from the expansion of the Hamiltonian of a spinning particle around a spinning BH [190]. Within this gauge, specifying the N^{3}LO spin-orbit contribution is equivalent to specifying 8 numerical coefficients. Here we consider two separate options: (i) on the one hand, we use a N^{3}LO parametrization that is tuned to NR simulations, following the usual procedure adopted within the `TEOBResumS` model; (ii) on the other hand, we also consider an *analytical version* of the N^{3}LO contribution that has been recently obtained with a mixture of several analytical techniques [154, 138].

NR-informed spin-orbit description Following previous work [190], at N^{3}LO order we only consider

$$c_{30} = \nu c_3, \tag{144}$$

$$c_{30}^* = \nu c_3 + \frac{135}{32}, \tag{145}$$

where c_3 is the NR-informed tunable parameter, while all other N^{3}LO coefficients are fixed to zero $c_{22} = c_{14} = c_{06} = c_{22}^* = c_{04}^* = c_{06}^* = 0$. The NR-informed expression of c_3, that will be found to be a function of ν and of the spins, will be discussed in Sec. 6.2.1 below.

Fully analytical spin-orbit description Recently, Refs. [154, 138] used first-order self-force (linear-in-mass-ratio) results to obtain arbitrary-mass-ratio results for the N^{3}LO correction to the spin-orbit sector of the Hamiltonian. The N^{3}LO contribution is given by Eqs.(8) and (9) of Ref. [154]. Once incorporated within the expression of (G_S, G_{S_*}) of Eqs. (142)-(143) above, the explicit ex-

pressions of the N^{3}LO coefficients read

$$c_{30} = \left(\frac{80399}{2304} - \frac{241}{384}\pi^2\right)\nu - \frac{31}{16}\nu^2 + \frac{397}{4096}\nu^3, \tag{146}$$

$$c_{22} = \frac{10563}{128}\nu - \frac{2273}{64}\nu^2 - \frac{2999}{4096}\nu^3, \tag{147}$$

$$c_{14} = -\frac{1421}{256}\nu + \frac{1257}{128}\nu^2 - \frac{2201}{4096}\nu^3, \tag{148}$$

$$c_{06} = -\frac{7}{256}\nu - \frac{9}{128}\nu^2 + \frac{83}{4096}\nu^3, \tag{149}$$

$$c^*_{30} = \frac{135}{32} + \left(\frac{5501}{144} - \frac{41}{48}\pi^2\right)\nu - \frac{5}{32}\nu^2 + \frac{5}{16}\nu^3, \tag{150}$$

$$c^*_{22} = \frac{773}{64} + \frac{2313}{32}\nu - \frac{245}{8}\nu^2 - 2\nu^3, \tag{151}$$

$$c^*_{14} = \frac{35}{48} + \frac{115}{6}\nu + \frac{395}{96}\nu^2 - \frac{9}{16}\nu^3, \tag{152}$$

$$c^*_{06} = -\frac{5}{96} + \frac{5}{16}\nu + \frac{37}{32}\nu^2 - \frac{\nu^3}{16}\ . \tag{153}$$

Spin-spin effects: NNLO accuracy The spin-spin sector incorporates NNLO information [223, 259] within the centrifugal radius r_c, according to the usual scheme typical of the `TEOBResumS` Hamiltonian [190]. In particular, we use here the analytical expressions obtained in Ref. [194] once specified to the BBH case. However, to robustly incorporate NNLO information in strong field, it is necessary to implement it in resummed form. To start with, we formally factorized the centrifugal radius as

$$r_c^2 = (r_c^{\rm LO})^2 \hat{r}_c^2, \tag{154}$$

where the $(r_c^{\rm LO})^2$ is the LO contribution, $\hat{r}_c^2$ the PN corrections up to NNLO. Concretely, we have

$$(r_c^{\rm LO})^2 = r^2 + \tilde{a}_0^2\left(1 + \frac{2}{r}\right)\ , \tag{155}$$

where $\hat{r}_c^2$ explicitly reads

$$\hat{r}_c^2 = 1 + \frac{\delta a^2_{\rm NLO}}{r(r_c^{\rm LO})^2} + \frac{\delta a^2_{\rm NNLO}}{r^2(r_c^{\rm LO})^2}, \tag{156}$$

and we have {see Eqs. (19) and (20) of Ref. [194]}

$$\delta a^2_{\rm NLO} = -\frac{9}{8}\tilde{a}_0^2 - \frac{1}{8}(1+4\nu)\tilde{a}_{12}^2 + \frac{5}{4}X_{12}\tilde{a}_0\tilde{a}_{12}, \tag{157}$$

$$\begin{aligned}\delta a^2_{\rm NNLO} = &-\left(\frac{189}{32}+\frac{417}{32}\nu\right)\tilde{a}_0^2 + \\ &+\left(\frac{11}{32}-\frac{127}{32}\nu+\frac{3}{8}\nu^2\right)\tilde{a}_{12}^2 + \\ &+\left(\frac{89}{16}-\frac{21}{8}\nu\right)X_{12}\tilde{a}_0\tilde{a}_{12}\ ,\end{aligned} \tag{158}$$

where $X_{12} \equiv X_1 - X_2$ and $\tilde{a}_{12} \equiv \tilde{a}_1 - \tilde{a}_2$. Direct inspection of the Taylor-expanded expression of r_c^2 shows its oscillatory behavior when moving from LO to NNLO. This suggests that to fruitfully incorporate the NNLO term, some resummation procedure should be implemented. To do so, we simply note that $\hat{r}_c^2$ given by Eq. (156) has the structure $1 + c_{\rm NLO}\epsilon + c_{\rm NNLO}\epsilon^2$, where ϵ is a formal PN ordering parameter[10], and it can be robustly resummed taking a P_2^0 approximant in ϵ. From now on, it is thus intended that we will work with the Padé resummed quantity $P_2^0[\hat{r}_c^2, \epsilon]$ instead of $\hat{r}_c^2$ in Taylor-expanded form.

6.1.3 Radiation reaction and waveform

The prescription for the radiation reaction force we are using follows Ref. [171] (see also [207]), although minimal details about the structure of $\hat{\mathcal{F}}_\varphi$ were explicitly reported there. We complement here the discussion of [171] for clarity and completeness.

[10]Note that NNLO spin-spin effect correspond to 4PN accuracy, while the LO is 2PN accuracy [223]. So, when LO is factored out one is left with a residual expansion that is 2PN accurate.

The global structure of $\hat{\mathcal{F}}_\varphi^\infty$ is that of the quasi-circular version of `TEOBResumS`, as discussed in Ref. [190]. In particular, its formal expression reads

$$\hat{\mathcal{F}}_\varphi^\infty = -\frac{32}{5}\nu\, r_\omega^4\, \Omega^5 \hat{f}(\Omega), \tag{159}$$

where r_ω is given by Eq. (70) of Ref. [190], $\Omega = \dot{\varphi}$ is the orbital frequency and $\hat{f}(\Omega)$ is the Newton-normalized flux function. For the quasi-circular model $\hat{f}(\Omega)$ is the circular flux function given by the sum of several modes $\hat{f}_{\ell m}$ where the hat indicates that each (ℓ, m) multipole is normalized by the $\ell = m = 2$ Newtonian flux $F_{22}^{\rm Newt} = 32/5\,\nu\,\Omega^{10/3}$. Each circularized multipole is then factorized and resummed according to Ref. [196]. In the most general case of motion along noncircular orbits, each Newton-normalized multipoles acquires a noncircular factor, so that the flux can be formally written as

$$\hat{f}(\Omega) = \sum_{\ell=2}^{8} \sum_{m=-\ell}^{\ell} \hat{f}_{\ell m} \hat{f}_{\ell m}^{\rm non-circular}. \tag{160}$$

Here we will consider only $\hat{f}_{22}^{\rm non-circular} \neq 0$ and use it in its Newtonian approximation, see Ref. [170]. The Newtonian non-circular factor reads

$$\begin{aligned}
\hat{f}_{22}^{\rm non-circular} = \hat{f}_{22}^{\rm Newt_{nc}} = 1 &+ \frac{3}{4}\frac{\ddot{r}^2}{r^2\Omega^4} - \frac{\ddot{\Omega}}{4\Omega^3} + \frac{3\dot{r}\dot{\Omega}}{r\Omega^3} + \\
&+ \frac{4\dot{r}^2}{r^2\Omega^2} + \frac{\ddot{\Omega}\dot{r}^2}{8r^2\Omega^5} + \frac{3}{4}\frac{\dot{r}^3\dot{\Omega}}{r^3\Omega^5} + \frac{3}{4}\frac{\dot{r}^4}{r^4\Omega^4} + \frac{3}{4}\frac{\dot{\Omega}^2}{\Omega^4} + \\
&- \dddot{r}\left(\frac{\dot{r}}{2r^2\Omega^4} + \frac{\dot{\Omega}}{8r\Omega^5}\right) + \ddot{r}\left(-\frac{2}{r\Omega^2} + \frac{\ddot{\Omega}}{8r\Omega^5} + \frac{3}{8}\frac{\dot{r}\dot{\Omega}}{r^2\Omega^5}\right).
\end{aligned} \tag{161}$$

For what concerns the $\ell = m = 2$ waveform, everything follows Ref. [196] except for a change in one of the functions that determine the next-to-quasi-circular (NQC) correction to the amplitude. In particular, it turns out that the function $n_2^{22} =$

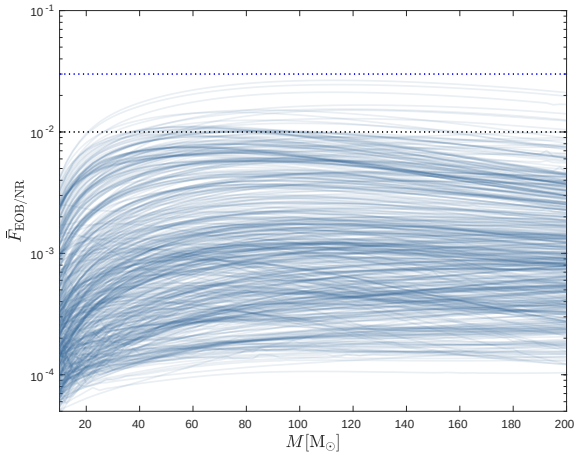

Figure 23: Unfaithfulness $\bar{F}_{\rm EOB/NR}(M)$ between the quasi-circular limit of the general `TEOBResumS` model and the complete SXS catalog of non-eccentric and non-precessing (spin-aligned) waveforms. These results are obtained using the NR-tuned N^{3}LO spin-orbit contribution. The horizontal dotted lines mark the 0.01 (black) and 0.03 (blue) values.

$\underline{\ddot{r}}^{(0)}/(r\Omega^2)$, where $\underline{\ddot{r}}^{(0)}$ is an approximation to the second derivative of the radial separation, given by Eq. (3.37) of Ref. [195], is not robust in strong field in conjunction with the new EOB potentials. As an alternative, we use instead

$$n_2^{22} = n_1^{22}(p_{r_*})^2 \ , \tag{162}$$

where

$$n_1^{22} = \left(\frac{p_{r_*}}{r\Omega}\right)^2 . \tag{163}$$

These choices ensure the construction of the NR-informed amplitude around merger that is robust, although it might sometimes slightly overestimate (by a few percents) the corresponding NR one.

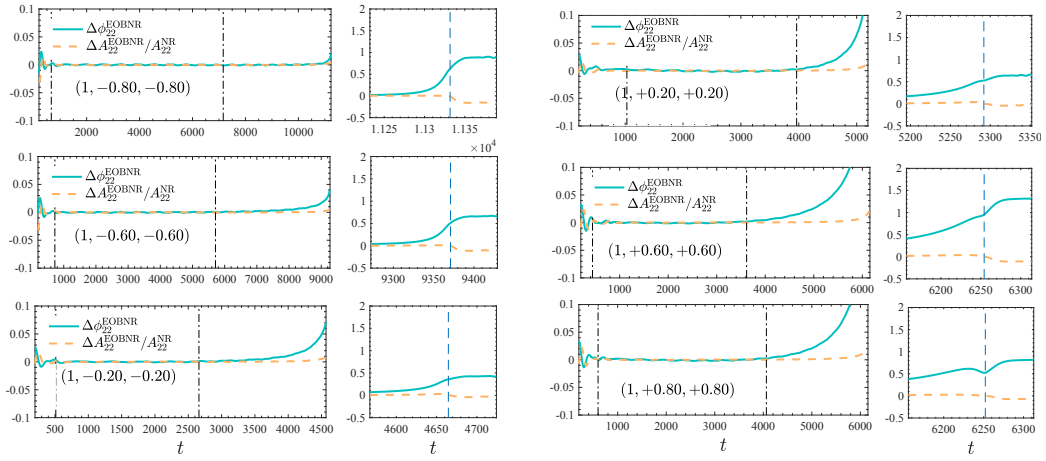

Figure 24: EOB/NR time-domain phase difference $\Delta\phi_{22}^{\rm EOBNR}$ and relative amplitude difference, $\Delta A_{22}^{\rm EOBNR}/A_{22}^{\rm NR}$ for a sample of equal-mass, equal-spin configurations. The model uses here the c_3 parameter from Eq. (165). The dash-dotted vertical lines indicate the alignment region, while the dashed line indicates the merger location. Note that $\bar{F}_{\rm EOBNR}^{\rm max} \lesssim 1\%$ even if the accumulated phase difference ~ 1 rad at merger for some configurations.

6.2 Quasi-circular configurations

6.2.1 EOB dynamics informed by NR simulations

We now proceed in determining new analytical representations of (a_6^c, c_3). The procedure is the same as the one discussed in Ref. [171].

We find a_6^c has a rather simple behavior, that is fitted as

$$a_6^c(\nu) = 599.96\nu^2 - 503.57\nu - 4.6416. \tag{164}$$

It is interesting to note that, although the physics that the model describes is the same of the model of Ref. [171], the differences in the analytical content and in the resummations yield a very simple behavior of $a_6^c(\nu)$. This is in striking contrast with Ref. [171], where it was needed an exponential function to fit (at a lower accuracy level) the single values of a_6^c.

The new functional form of $a_6^c(\nu)$ given by Eq. (164) calls for a similarly new determination of the effective spin-orbit parameter

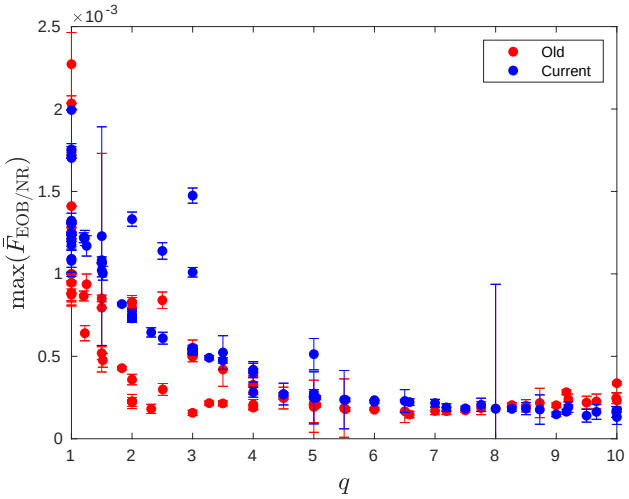

Figure 25: Complement to Fig. 23: $\bar{F}^{\rm max}_{\rm EOB/NR}$ values for all SXS non-spinning configurations. The current iteration of `TEOBResumS` is compared to the quasi-circular model of Ref. [196], with errorbars that represent the values of $\bar{F}^{\rm max}_{\rm NR/NR}$ cited therein (see Tables XVIII-XIX). Note that SXS datasets with the same q have different NR accuracies. The EOB/NR agreement for this subset of data is largely improved with respect to Fig. 3 of Ref. [171] and mostly consistent with the result of the quasi-circular model.

c_3. c_3 is fitted with a global function of the spin variables $\tilde{a}_i$ of the form

$$c_3(\tilde{a}_1,\tilde{a}_2,\nu) = p_0\frac{1+n_1\tilde{a}_0+n_2\tilde{a}_0^2+n_3\tilde{a}_0^3+n_4\tilde{a}_0^4}{1+d_1\tilde{a}_0}+ \\ + p_1\tilde{a}_0\nu\sqrt{1-4\nu}+p_2\left(\tilde{a}_1-\tilde{a}_2\right)\nu^2+p_3\tilde{a}_0\nu^2\sqrt{1-4\nu}, \quad (165)$$

where the functional form is the same of previous works[11]. This term helps in improving the fit flexibility as the mass ratio in-

[11]Note that this function is not symmetric for exchange of $1\leftrightarrow 2$. This can create an ambiguity for $q=1$, so that the value of c_3 for $(1,0.6,0.4)$ is in fact different from the one for $(1,0.4,0.6)$. In fact, our convention and implementations are such that for $q=1$, χ_1 is *always* the largest spin.

creases. The fitting coefficients read

$$\begin{aligned} p_0 &= 35.482253, \\ n_1 &= -1.730483, \\ n_2 &= 1.144438, \\ n_3 &= 0.098420, \\ n_4 &= -0.329288, \\ d_1 &= -0.345207, \\ p_1 &= 244.505, \\ p_2 &= 148.184, \\ p_3 &= -1085.35. \end{aligned} \tag{166}$$

Consistency between EOB potentials Now that we have determined the new expression of $a_6^c(\nu)$ it is instructive to compare different realizations of the potential. The top panel of Fig. 22 shows together different curves for the case $q = 1$: (i) The $P_3^3[A]$ potential with the NR-informed $a_6^c(\nu)$ given by Eq. (164) above; (ii) the $P_5^1[A]$ potential of `TEOBResumS`, where the NR-informed function is given by Eq. (33) of Ref. [196]; (iii) the $P_5^1[A]$ function with $a_6^c = a_{6\mathrm{anlyt}}^c$; (iv) the $P_3^3[A]$ function with $a_6^c = a_{6\mathrm{anlyt}}^c$. In the bottom panel of the figure we show the effective photon potential $u^2 A$. The most interesting outcome is the visual *consistency* between the two NR-informed potentials up to $u \simeq 0.4$. This reflects in two close dynamics, that eventually yield highly faithful EOB/NR phasing for the non-spinning case, as we will see below. The fact is remarkable because *both* the radiation reaction and the (D, Q) potentials are different in the two cases. One should note, however, that the fact that the two potentials are consistent up to $u = 0.4$ *does not mean* that they are equivalent and that the conservative dynamics coincide. In fact, it is known [219] that two A potentials are equivalent when their difference is of the order of 10^{-4}. The two NR-informed poten-

tials differ by just 10^{-2}, so that even if they look close, they are meaningfully different. A similar visual consistency shows up also for the $P_5^1[A]$ analytical function, despite the presence of the spurious pole. By contrast the fully analytical $P_3^3[A]$ is significantly separated from the others. In practical terms, when used in the EOB dynamics, the $P_3^3[A]$ analytical potential will *accelerate* the inspiral with respect to the NR-informed ones, eventually yielding unacceptably large phase differences at merger. If one wished to incorporate this specific resummation, some other element of the model [e.g. radiation reaction or the (D, Q) functions] should be modified to balance its attractive effect. This gives a pedagogical example of the fact that the accessibility of high-order PN information[12] does not necessarily simplify or help the construction of waveform models and it is pragmatically more efficient to resort to NR-informed functions.

Validating the model To evaluate the quality of the EOB waveform we computed the EOB/NR unfaithfulness weighted by the Advanced LIGO noise over all available spin-aligned SXS configurations [113, 116]. Considering two waveforms (h_1, h_2), the unfaithfulness is a function of the total mass M of the binary and is defined as

$$\bar{F}(M) \equiv 1 - F = 1 - \max_{t_0,\phi_0} \frac{\langle h_1, h_2 \rangle}{||h_1||||h_2||}, \tag{167}$$

where (t_0, ϕ_0) are the initial time and phase. We used $||h|| \equiv \sqrt{\langle h, h \rangle}$, and the inner product between two waveforms is defined as $\langle h_1, h_2 \rangle \equiv 4\Re \int_{f_{\rm min}^{\rm NR}(M)}^{\infty} \tilde{h}_1(f)\tilde{h}_2^*(f)/S_n(f)\, df$, where $\tilde{h}(f)$ denotes the Fourier transform of $h(t)$, $S_n(f)$ is the zero-detuned, high-power noise spectral density of Advanced LIGO [261] and $f_{\rm min}^{\rm NR}(M) = \hat{f}_{\rm min}^{\rm NR}/M$ is the initial frequency of the NR waveform at highest resolution, i.e. the frequency measured after

[12] Although incomplete, seen the lack of the yet unknown $(a_6^{\nu^2}, d_5^{\nu^2})$ coefficients.

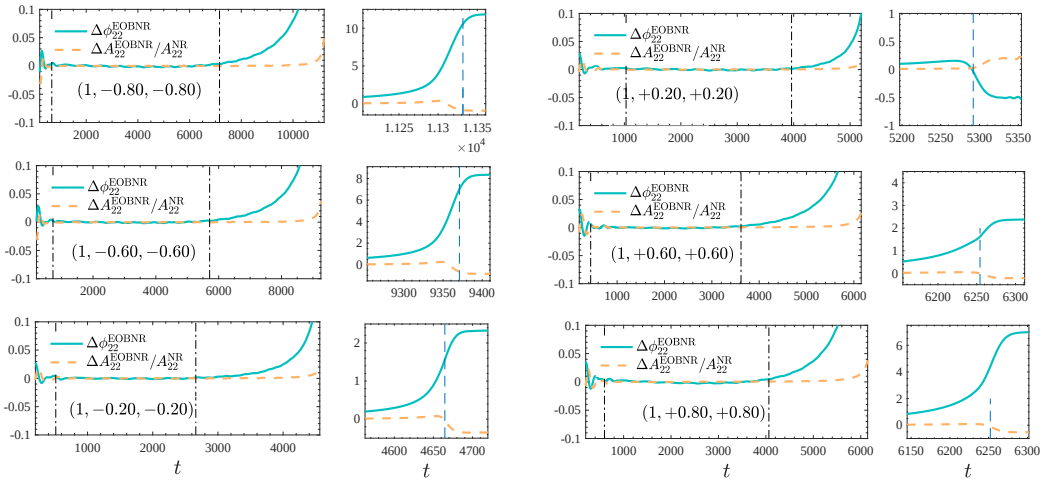

Figure 26: EOB/NR time-domain phase difference $\Delta\phi_{22}^{\rm EOBNR}$ and relative amplitude difference, $\Delta A_{22}^{\rm EOBNR}/A_{22}^{\rm NR}$ for a sample of equal-mass, equal-spin configurations. The model uses here the *analytical description* of N^{3}LO spin-orbit effect, with $c_4 = 0$. The dash-dotted vertical lines indicate the alignment region, while the dashed line indicates the merger location. The large values of $\Delta\phi_{22}^{\rm EOBNR}$ at merger eventually end up with values of $\bar{F}^{\rm max}_{\rm EOBNR}$ even above the 3% level, see Fig. 27 below.

the junk-radiation initial transient. Waveforms are tapered in the time-domain so as to reduce high-frequency oscillations in the corresponding Fourier transforms. The EOB/NR unfaithfulness is addressed as $\bar{F}_{\rm EOB/NR}$. The result of this computation is shown in Fig. 23. We can see that the maximum unfaithfulness is mostly below 0.01 and always below 0.03. In Fig. 24 we also display time-domain phasing comparisons for some selected equal-mass configurations. We can see the phase differences at merger are always between 0.5 and 1 radiant. We will highlight in Fig. 28 below that the higher $\bar{F}_{\rm EOB/NR}$ correspond to configuration with large spin values, aligned with the orbital angular momentum.

Before doing so, it is instructive also to show separately the $\bar{F}^{\rm max}_{\rm EOB/NR}$ restricted to the non-spinning case. The chosen NR waveforms are listed in Tables XVIII-XIX of Ref. [196], with

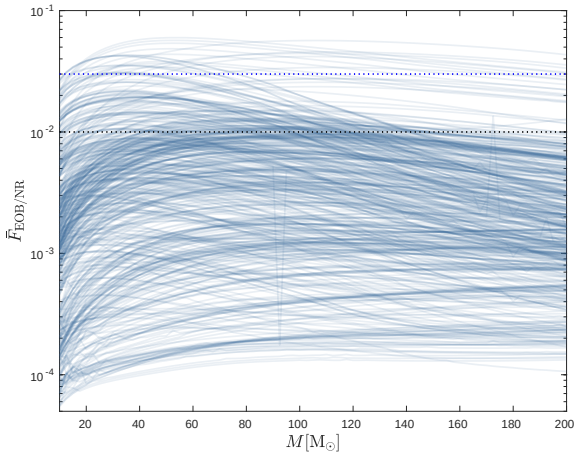

Figure 27: Unfaithfulness $\bar{F}_{\rm EOB/NR}(M)$ between `TEOBResumS` and the complete SXS catalog of non-eccentric non-precessing waveforms obtained using the analytical N^{3}LO spin-orbit contribution. The horizontal dotted lines mark the 0.01 (black) and 0.03 (blue) values.

the exclusion of the 3 BAM [114] ones and 6 precessing configurations that were erroneously included there [13]. To better appreciate the improvement with respect to Ref. [171], Fig. 25 compares the current (non-spinning) $\bar{F}^{\rm max}_{\rm EOB/NR}$ values with those of `TEOBResumS` obtained in Ref. [196]. There is an excellent consistency between the two dataset, although the current model is performing slightly worse up to $q = 4$.

6.2.2 Fully analytical EOB spin-orbit dynamics at N^{3}LO and beyond

Let us finally evaluate the EOB/NR performance using the fully analytical expression for the N^{3}LO spin-orbit contribution. First of all, Fig. 26 displays time-domain phasing comparisons for the same $q = 1$ configurations considered above. The phase differences at merger are rather larger, especially for large values of the individual spins. The EOB/NR unfaithfulness computation

[13] Namely SXS:BBH:0850, SXS:BBH:0858, SXS:BBH:0869, SXS:BBH:2019, SXS:BBH:2025 and SXS:BBH:2030.

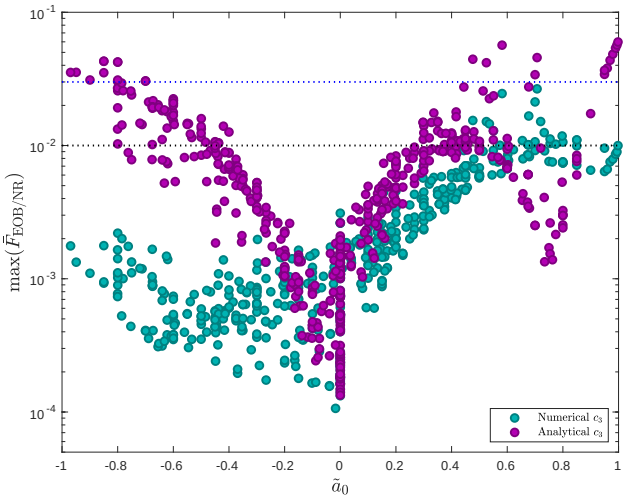

Figure 28: Global picture of the maximum EOB/NR unfaithfulness from Fig. 23 and Fig. 27 using the NR-informed and the analytical N^{3}LO spin-orbit contribution respectively. The black and blue dotted lines mark the 0.01 and 0.03 values respectively. The use of the analytical spin-orbit contribution delivers a NR-faithful model only in a rather limited range of $\tilde{a}_0$.

is reported in Fig. 27: one finds that there are many configuration even above the fiducial threshold of 3%. To have a simple understanding of the inaccurate configurations it is helpful to plot $\bar{F}^{\rm max}_{\rm EOB/NR}$ versus the effective spin $\tilde{a}_0$, Fig. 28. One sees that the EOB/NR agreement degrades progressively as the effective spin increases or decreases. In practice, the analytical model can be considered robustly faithful ($< 1\%$) only for mild values of the effective spin. Note however that there is a region where $\bar{F}^{\rm max}_{\rm EOB/NR} < 1\%$ also for large, positive spins. This corresponds roughly to simulations where $0.6 \lesssim \tilde{a}_0 \lesssim 0.8$ and $q < 5$. For completeness, the same plot also reports (with green markers) the values of $\bar{F}^{\rm max}_{\rm EOB/NR}$ for the NR-informed value of c_3, so to give complementary information to the one of Fig. 23. To conclude, what is striking in this comparison is that, similarly to the case of a^c_6 mentioned above a suitably NR-tuned effective function is pragmatically *more efficient* than the outcome of a high-order analytical calculation.

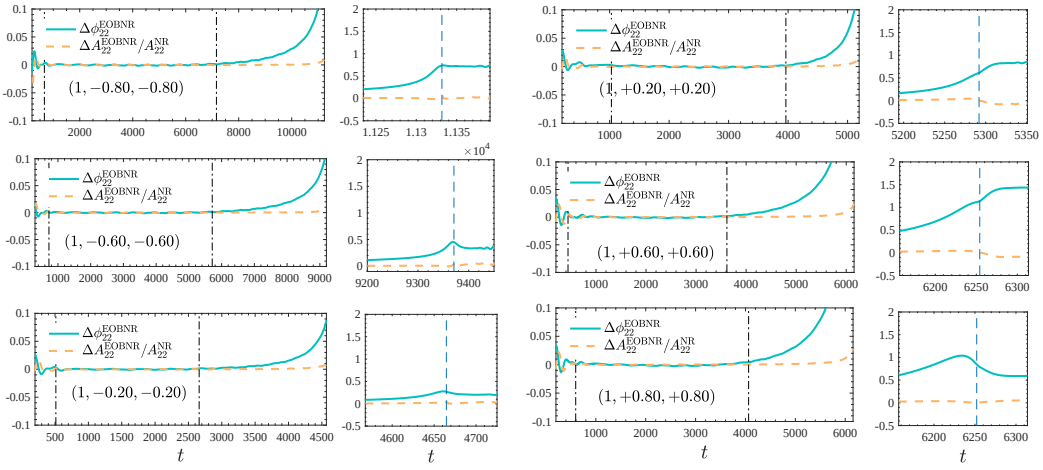

Figure 29: EOB/NR time-domain phase difference $\Delta\phi_{22}^{\rm EOBNR}$ and relative amplitude difference, $\Delta A_{22}^{\rm EOBNR}/A_{22}^{\rm NR}$ for a sample of equal-mass, equal-spin configurations. The model uses here the *analytical description* of N^{3}LO spin-orbit effect augmented by a NR-tuned coefficient c_4 at N^{4}LO, as given by Eq. (168). The dash-dotted vertical lines indicate the alignment region, while the dashed line indicates the merger location. The phase difference at merger is reduced with respect to the $c_4 = 0$ case of Fig. 26, although it is still slightly less good (especially for negative spins) than the simple NR-tuned c_3 case of Fig. 24.

In this respect, we recall that in our definitions of (G_S, G_{S_*}) we introduced two formal N^{4}LO terms, where $c_{40}^* = 2835/256$, fixed to the spinning test-mass value. However, analogously to the case of c_3, we can *flex* these two coefficients as $c_{40} = \nu c_4$ and $c_{40}^* = \nu c_4 + 2835/256$ introducing an effective N^{4}LO parameter that can be tuned to NR simulations analogously to c_3. We show this here explicitly by determining c_4 for the specific case of equal-mass, equal spin binaries and evaluating the resulting performance in terms of phasing. c_4 can be fitted by a quadratic function of $\tilde{a}_0$, yielding the following function

$$c_4 = 39.43\,\tilde{a}_0^2 - 141.77\,\tilde{a}_0 + 65.73. \tag{168}$$

The corresponding time-domain comparison (either phase difference and amplitude difference) are shown in Fig. 29. The

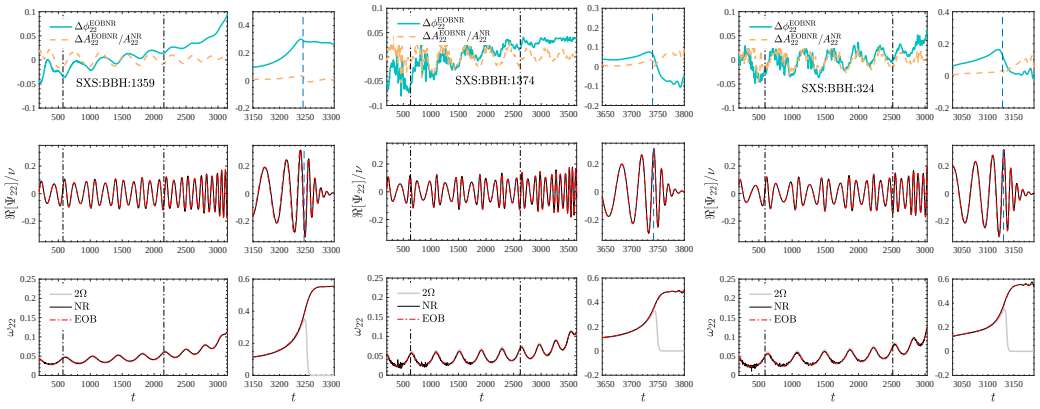

Figure 30: EOB/NR time-domain phasing comparison three meaningful configurations SXS:BBH:1359, SXS:BBH:1374 and SXS:BBH:324. The phasing agreement is largely improved with respect to the corresponding ones shown in Fig. 10 of Ref. [171]. The vertical dash-dotted lines in the left panels indicate the alignment interval, while the merger location is marked by a dashed vertical line in the right panels.

phase difference at merger is notably reduced with respect to the $c_4 = 0$ case of Fig. 26, although it is still slightly less good than the simple NR-tuned c_3 case of Fig. 24. It seems thus that the use of the complete analytical N^{3}LO spin-orbit information within the current model just moves the need of a NR-tuned parameter at the N^{4}LO order with slightly less accuracy and with no real advantage. This suggests that, within the current model, it is more efficient to simply adopt the NR-tuned c_3 parameter.

6.3 Eccentric inspiral configurations

Let us move now to discussing eccentric inspirals. To do so, we precisely repeat here the analysis of Ref. [171], see Secs. IIIC and IIID therein. To start with, Fig. 30 reports the $\ell = m = 2$ time-domain phasing comparison for 3 NR simulation with non-negligible eccentricity: SXS:BBH:1359, that corresponds to a system with $(q, \chi_1, \chi_2) = (1, 0, 0)$ and NR eccentricity at first apastron $e^{\rm NR}_{\omega_a} = 0.112$; SXS:BBH:1374, whose parameters

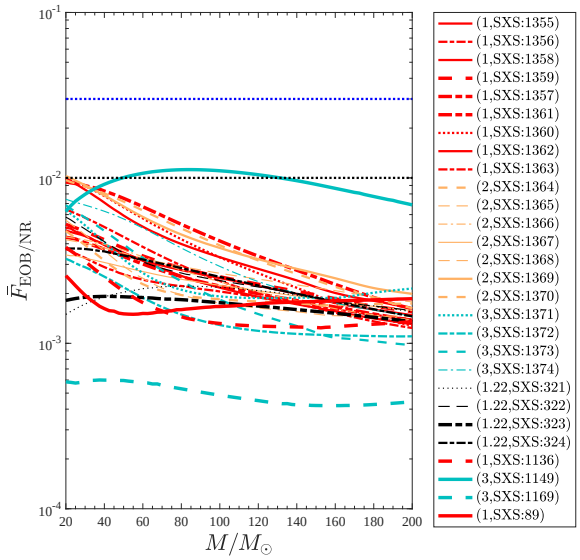

Figure 31: EOB/NR unfaithfulness for the $\ell = m = 2$ mode computed over the eccentric SXS simulations publicly available. The 28 configurations are labeled with their mass ratio and SXS id, while the other parameters can be found in Table III of Ref. [171]. The horizontal lines mark the 0.03 and 0.01 values. All configurations are well below the 1% except for SXS:BBH:1149, corresponding to $(3, +0.70, +0.60)$ with $e^{\rm NR}_{\omega_a} = 0.037$, that is grazing this value. This is consistent with the slight degradation of the model performance for large positive spins, as found in the quasi-circular limit.

are $(3, 0, 0)$ and $e^{\rm NR}_{\omega_a} = 0.208$; and SXS:BBH:324, for which $(q, \chi_1, \chi_2) = (1.22, 0.33, -0.44)$ and $e^{\rm NR}_{\omega_a} = 0.205$. For each configuration, (i) at the top we have the phase difference and the relative amplitude difference; (ii) in the middle we compare the real parts of the waveform; (iii) in the bottom panel we compare the EOB and NR GW frequency, together with twice the orbital frequency Ω. The phasing agreement is largely improved with respect to what shown in Fig. 10 and Fig. 14 of Ref. [171]: the EOB/NR phase difference is rather low and does not vary much during the inspiral and remains of the order of $0.1 - 0.2$ rad up to merger as well.

The global vision of the model performance is given by Fig. 31, that highlights the EOB/NR unfaithfulness versus the total mass

of the system for all publicly available SXS simulations [118, 116]. These contain both spinning and non-spinning systems, with mass ratios between 1 and 3 and eccentricity $e^{\rm NR}_{\omega_a}$ approximately in the range $0.05 - 0.2$. The typical length of such waveforms are 10 to 20 orbits before merger. We find that all configurations are well below 1% except for SXS:BBH:1149, that is grazing this value. This is not surprising since SXS:BBH:1149 has parameter $(3, +0.7, +0.6)$, that give $\tilde{a}_0 = 0.675$, a value that belongs to the region of $\tilde{a}_0$ where it is not possible to obtain a highly NR-faithful modelization already in the quasi-circular case. Despite this, the improvements in the quasi-circular sector reflect all over the $\bar{F}_{\rm EOB/NR}$ behavior of Fig. 31, either for small or for large eccentricities. This is in particular the case for the $q = 1$ configurations, where $\bar{F}_{\rm EOB/NR}$ gets down to $\sim 10^{-3}$. This is a remarkable improvement with respect to the results of Ref. [171], where $\bar{F}_{\rm EOB/NR}$ was grazing the 1% threshold for these configurations (see Fig. 11 therein).

Given the exploratory character of the current study, we have just briefly looked at higher modes. The NR-accurate behavior of all waveform modes during the inspiral is comparable to what discussed in Ref. [171]. By contrast, for what concerns merger and ringdown, although the modes with $m = \ell$ usually (though not always) look generally sane, those with $m \neq \ell$ may develop unphysical behaviors due to the action of NQC corrections, as already noted in Ref. [171]. This problem, that has always been present within `TEOBResumS` [166], is now even amplified because of the existence of an effective horizon corresponding to the fact that the A function has a zero at a finite value of u. The issue of robustly determining NQC corrections for any multipole will require more dedicated investigations, that we will postpone to future work. We only anticipate that it is likely that a deeper understanding of NQC corrections (especially in relation with the dynamics) in the test-mass limit [207] will be required to

overcome what currently seems to be the most evident Achilles' heel of `TEOBResumS`-based waveform models.

6.4 Hyperbolic encounters and scattering angle

To conclude, we present a new calculation of the EOB scattering angle from hyperbolic encounters and compare it with the few NR simulations available, updating the results obtained in the previous section (and Ref. [171]). The changes in the conservative part of the dynamics will impact quantitatively on the scattering angle computation, although the phenomenology remains unchanged. We repeat here the EOB calculation of the scattering angle χ for the 10 configurations simulated in NR [247] that are discussed in Table 2. The EOB outcome, together with the original NR values, $(\chi^{\rm EOB}, \chi^{\rm NR})$ is listed in Table 8. The table also reports the GW energy, ΔE, and angular momentum, ΔJ, losses for both the NR simulations and the EOB dynamics [14]. It is evident the remarkable improvement with respect to the results of Ref. [171]. In particular, the strong-field configuration #1, shows an EOB/NR disagreement of only about 4%, *four times smaller* than the one Ref. [171]. On top of validating the model for extreme orbital configurations, this finding is also a reliable cross check of the consistency and robustness of our procedure to obtain $a_6^c(\nu)$: although the function was determined using quasi-circular configurations, its impact looks to be essentially correct *also* for scattering configuration. This makes us confident that our NR-informed analytical choices do represent a reliable, though certainly effective, representation of the strong-field dynamics of two non-spinning BHs.

[14] Let us specify that while the NR losses are computed from the waveform, the EOB losses are computed subtracting the initial and final energy and angular momentum, i.e. effectively accounting for the action of the radiation reaction on the dynamics.

Table 8: Comparison between EOB and NR scattering angle. From left to right the columns report: the ordering number; the EOB impact parameter $r_{\rm min}$; the NR and EOB radiated energies, $(\Delta E^{\rm NR}/M, \Delta E^{\rm EOB}/M)$; the NR and EOB radiated angular momentum, $(\Delta J^{\rm NR}/M^2, \Delta J^{\rm EOB}/M^2)$; the NR and EOB scattering angles $(\chi^{\rm NR}, \chi^{\rm EOB})$ and their fractional difference $\hat{\Delta}\chi \equiv |\chi^{\rm NR} - \chi^{\rm EOB}|/\chi^{\rm NR}$.

#	$r_{\rm min}$	$\Delta E^{\rm NR}/M$	$\Delta E^{\rm EOB}/M$	$\Delta J^{\rm NR}/M^2$	$\Delta J^{\rm EOB}/M^2$	$\chi^{\rm NR}$ [deg]	$\chi^{\rm EOB}$[deg]	$\hat{\Delta}\chi$[%]
1	3.512	0.01946(17)	0.018785	0.17007(89)	0.159229	305.8(2.6)	317.349057	3.7767
2	3.79	0.01407(10)	0.012886	0.1380(14)	0.119728	253.0(1.4)	257.702771	1.8588
3	4.09	0.010734(75)	0.009449	0.1164(14)	0.095350	222.9(1.7)	224.412595	0.6786
4	4.89	0.005644(38)	0.004612	0.076920(80)	0.057402	172.0(1.4)	171.283157	0.4168
5	5.37	0.003995(27)	0.003175	0.06163(53)	0.044473	152.0(1.3)	151.118180	0.5801
6	6.52	0.001980(13)	0.001524	0.04022(53)	0.027313	120.7(1.5)	119.931396	0.6368
7	7.61	0.0011337(90)	0.000867	0.029533(53)	0.018971	101.6(1.7)	101.066199	0.5254
8	8.68	0.007108(77)	0.000547	0.02325(47)	0.014158	88.3(1.8)	87.965443	0.3789
9	9.74	0.0004753(75)	0.000371	0.01914(76)	0.011084	78.4(1.8)	78.168216	0.2956
10	10.79	0.0003338(77)	0.000265	0.0162(11)	0.008982	70.7(1.9)	70.477124	0.3152

6.5 Summary

We have explored the performance of a new EOB model for spin-aligned binaries for three types of binary configurations: (i) quasi-circular inspiral; (ii) eccentric inspiral; (iii) hyperbolic scattering. The novelty of this model is the use of recently computed high-order PN information in both the orbital and spin sector.

In the non-spinning case, the best resummation option to incorporate (some of) the currently available 5PN information in the EOB potentials (A, D, Q) consists in using diagonal and near diagonal Padé approximants. In this case, the performance of the model in the quasi-circular limit is essentially equivalent to the standard quasi-circular version of `TEOBResumS` [196].

Results in the spinning case are globally more faceted. First of all, differently from previous work, we incorporate spin-spin effects up to NNLO, where the centrifugal radius is now written in a factorized and resummed form. Within this paradigm, we have explored two options for the spin-orbit sector: (i) on the one hand, we follow the usual `TEOBResumS` paradigm and include an effective N^{3}LO spin-orbit correction through a parameter c_3 that is informed by NR simulations; (ii) on the other hand, we exploit recent analytical results [154] that provided the complete analytical expression for this contribution. This latter can be additionally modified through the inclusion of a N^{4}LO effective spin-orbit term. In the case of the NR-informed c_3 it is possible to obtain a model that is NR faithful in the usual sense, with $\bar{F}_{\rm max} \lesssim 3\%$. One should note however that the performance worsens specifically when the mass ratio and the spins are large and positive. By contrast, when the analytically known N^{3}LO spin-orbit information is implemented, the model remains acceptably faithful in a more limited range of $-0.4 \lesssim \tilde{a}_0 \lesssim +0.4$, although the EOB/NR phase difference at merger can be as large

as several radians. For the special equal-mass, equal-spin case, we have also shown that the N^{3}LO-accurate analytical spin-orbit sector can be flexed and improved using an effective N^{4}LO function c_4 that can be tuned to NR simulations like c_3. This allows to achieve an EOB/NR phasing agreement that is comparable to, although slightly less good than, the one obtained with the NR-tuned c_3 alone. This result suggests that, at least within the current analytical paradigm, pushing the spin-orbit information to the currently known analytical level doesn't seem to be fruitful.

The improvement in the quasi-circular sector of the model also reflects on the modelization of eccentric inspirals. We performed a EOB/NR waveform comparison analogous to the one of Ref. [171] and we found that a rather small EOB/NR phase difference is maintained up to merger, especially for the non-spinning datasets considered. This entails EOB/NR unfaithfulness $\bar{F}_{\rm EOB/NR}(M)$ that are always below 1% and actually $\lesssim 0.3\%$ for most configurations. This finding mirrors the improvement achieved in the model in the description of the late-inspiral and plunge phase with respect to Ref. [171].

For the hyperbolic orbits case, we repeat the EOB/NR comparison of the scattering angle previously performed [247, 171]. Remarkably, the joint action of the increased PN information, new Padé resummation and NR-informed a_6^c (notably, to quasi-circular NR simulations) allows for a further improvement of the EOB/NR agreement of the scattering angles. This amounts to a EOB/NR disagreement of only $\sim 4\%$ for the dataset with the smallest impact parameter, a factor of 4 smaller than the result of Ref. [171]. This consistency between the various configurations seems to suggest that, at least in the non-spinning case, the combination of the various analytical ingredients entering the model can offer a reliable and robust representation of the general BBH dynamics.

7 Conclusions

In this thesis we have performed an extensive study of semi-analytical EOB-NR models. The EOB approach is fundamental to resum analytical perturbative results in order to improve their reliability during the late inspiral stages of binary systems. NR results are then used to inform the models so to reach an even better accuracy near merger and to describe the merger-ringdown waveform.

EOB-NR models are unique between GW approximants because they describe both the dynamics and waveform of binary systems. This makes them very easy to extend beyond quasi-circular orbits so to compute eccentric or hyperbolic ones. They are also flexible enough to take into account parametric extensions of GR.

We first compared the two state-of-the-art EOB-NR models for spin-aligned binaries, `TEOBResumS` and `SEOBNRv4`. They are both built using the same EOB framework but differ both in the amount of analytical information they contain and in various arbitrary decisions made during their development. In fact, when building an EOB-NR model, one can choose: how to implement the ν-dependent deformation of the Kerr metric; how to resum all the PN-expanded quantities; what gauge to use in the spinning sector; where and how to include NR information. All these choices contribute to the theoretical uncertainty built into these models. In performing this analysis, we found qualitative and quantitative differences between `TEOBResumS` and `SEOBNRv4`, especially in the spin sectors. These discrepancies are mitigated but not eliminated by the calibration to NR simulations. While these differences are not appreciable with the SNRs of current detections, they could give rise to biases in the estimated parameters for signals measured by the next generation of GW detectors. Studies of these waveform systematics will hence be

very important to understand the theoretical limits of EOB-NR models.

Secondly, we detailed the use of the eccentric extension of `TEOBResumS` to generate waveforms for scatterings and dynamical captures of BBHs. Accurate theoretical models for these scenarios are not yet available but would be very useful to complement the current analyses based on quasi-circular models. In particular, hyperbolic models could help discerning dynamical captures and head-on collisions from highly precessing systems, since the emitted waveforms can have a very similar morphology. We have thus explored the parameter space of dynamical captures, characterizing various regions on the basis of the number of close encounters that happen before merger. We also studied the impact that including high-order PN information in one of the EOB potentials has on the scattering angle comparison with the few available NR simulations of BH hyperbolic encounters. We found it however impossible to make statements on the accuracy of the model because of the scarce number of numerical results for these scenarios.

The third work describes the effort to build a general version of `TEOBResumS` with a satisfactory EOB/NR agreement for quasi-circular, eccentric and hyperbolic simulations. We studied the effect of high-order information on both the non-spinning and the spinning sectors of the model. In doing so, we needed to change resummation schemes for some of the analytical perturbative series. We found that, even increasing the amount of analytical content of the model, NR information is still fundamental to reach the desired level of accuracy. With specific choices for the resummations of the EOB potentials, at least in the non-spinning case, we were able to reach a reliable representation of the general BBH dynamics.

With these results in mind, we can look at the future with optimism. `TEOBResumS` is not yet accurate enough to be used

for analyses of GW signals that we expect to measure with the third generation of detectors. However, the required unfaithfulness could be reached in the coming years. At the same time, EOB-NR models show promising signs in the waveform generation for eccentric binaries, that will be detected by future GW detectors, and even scattering systems. Numerical results will play a fundamental role in these endeavors: simulations covering the parameter space for eccentric and hyperbolic systems will be needed to inform and successively validate semi-analytical models. If these efforts will be successful, and theoretical predictions will be able to match the astounding sensitivity of the next generation of GW observatories, we will deepen our understanding of black holes and neutron stars, general relativity, cosmology and the universe as a whole.

A Notation and conventions

Geometric units	$G = c = 1$
Mass of heavier object	m_1
Mass of lighter object	m_2
Total mass	$M = m_1 + m_2$
Reduced mass	$\mu = m_1 m_2 / M$
Mass ratio	$q = m_1/m_2$
Symmetric mass ratio	$\nu = m_1 m_2 / M^2$
Mass fractions	$X_i = m_i/M$
Spins of the objects	$S_i, \qquad i = 1, 2$
Dimensionless spins	$\chi_i = S_i/m_i^2$
	$\tilde{a}_i = X_i \chi_i$
Additional spin variables	$\tilde{a}_0 = \tilde{a}_1 + \tilde{a}_2$
	$\tilde{a}_{12} = \tilde{a}_1 - \tilde{a}_2$
	$\hat{S} = X_1^2 \chi_1 + X_2^2 \chi_2$
	$\hat{S}_* = X_1 X_2 (\chi_1 + \chi_2)$
EOB time	$t = T/M$
EOB orbital phase	φ
Relative EOB separation	$r = R/M$
	$\mathrm{u} = 1/\mathrm{r}$
EOB angular momentum	$p_\varphi = P_\varphi/(\mu M)$
EOB radial momentum	$p_r = P_r/\mu$
	$p_{r_*} \equiv \sqrt{A/B}\, p_r$
Time derivative	$\dot{x} = \partial x/\partial t$
Radial derivative	$x' = \partial x/\partial r$
EOB orbital frequency	$\Omega = \dot{\varphi}$
EOB potentials	A, D, Q
	$B = D/A$
Centrifugal radius	r_c
Gyro-gravitomagnetic functions	G_S, G_{S_*}
EOB Hamiltonian	$\hat{H}_{\mathrm{EOB}} = \sqrt{1 + 2\nu\left(\hat{H}_{\mathrm{eff}} - 1\right)}/\nu$
EOB effective Hamiltonian	$\hat{H}_{\mathrm{eff}} = \hat{H}_{\mathrm{eff}}^{\mathrm{orb}} + p_\varphi \left(G_s \hat{S} + G_{S_*} \hat{S}_*\right)$
	$\hat{H}_{\mathrm{eff}}^{\mathrm{orb}} = \sqrt{p_{r_*}^2 + A\left[1 + \frac{p_\varphi^2}{r_c^2} + Q\right]}$
Radiation reaction fluxes	$\hat{\mathcal{F}}_r, \hat{\mathcal{F}}_\varphi$

References

[1] B. P. Abbott et al., "Observation of Gravitational Waves from a Binary Black Hole Merger," Phys. Rev. Lett., vol. 116, no. 6, p. 061102, 2016.

[2] A. Einstein, "The Foundation of the General Theory of Relativity," Annalen Phys., vol. 49, no. 7, pp. 769–822, 1916. [,65(1916)].

[3] A. Einstein, "Approximative Integration of the Field Equations of Gravitation," Sitzungsber. Preuss. Akad. Wiss. Berlin (Math. Phys.), vol. 1916, pp. 688–696, 1916.

[4] K. Schwarzschild, "On the gravitational field of a mass point according to Einstein's theory," Sitzungsber. Preuss. Akad. Wiss. Berlin (Math. Phys.), vol. 1916, pp. 189–196, 1916.

[5] B. P. Abbott et al., "GW170817: Observation of Gravitational Waves from a Binary Neutron Star Inspiral," Phys. Rev. Lett., vol. 119, no. 16, p. 161101, 2017.

[6] B. P. Abbott et al., "Multi-messenger Observations of a Binary Neutron Star Merger," Astrophys. J., vol. 848, no. 2, p. L12, 2017.

[7] J. Weber, "Evidence for discovery of gravitational radiation," Phys. Rev. Lett., vol. 22, pp. 1320–1324, 1969.

[8] P. Astone et al., "IGEC2: A 17-month search for gravitational wave bursts in 2005-2007," Phys. Rev. D, vol. 82, p. 022003, 2010.

[9] J. Aasi et al., "Advanced LIGO," Class. Quant. Grav., vol. 32, p. 074001, 2015.

[10] F. Acernese et al., "Advanced Virgo: a second-generation interferometric gravitational wave detector," Class. Quant. Grav., vol. 32, no. 2, p. 024001, 2015.

[11] T. Akutsu et al., "KAGRA: 2.5 Generation Interferometric Gravitational Wave Detector," Nature Astron., vol. 3, no. 1, pp. 35–40, 2019.

[12] D. Reitze et al., "Cosmic Explorer: The U.S. Contribution to Gravitational-Wave Astronomy beyond LIGO," Bull. Am. Astron. Soc., vol. 51, p. 035, 7 2019.

[13] M. Punturo, M. Abernathy, F. Acernese, B. Allen, N. Andersson, et al., "The Einstein Telescope: A third-generation gravitational wave observatory," Class.Quant.Grav., vol. 27, p. 194002, 2010.

[14] P. Amaro-Seoane et al., "Laser Interferometer Space Antenna," 2 2017.

[15] A. Sesana, "Prospects for Multiband Gravitational-Wave Astronomy after GW150914," Phys. Rev. Lett., vol. 116, no. 23, p. 231102, 2016.

[16] B. P. Abbott et al., "GWTC-1: A Gravitational-Wave Transient Catalog of Compact Binary Mergers Observed by LIGO and Virgo during the First and Second Observing Runs," Phys. Rev., vol. X9, no. 3, p. 031040, 2019.

[17] R. Abbott et al., "GWTC-2: Compact Binary Coalescences Observed by LIGO and Virgo During the First Half of the Third Observing Run," Phys. Rev. X, vol. 11, p. 021053, 2021.

[18] R. Abbott et al., "GWTC-3: Compact Binary Coalescences Observed by LIGO and Virgo During the Second Part of the Third Observing Run," 11 2021.

[19] R. Abbott et al., "The population of merging compact binaries inferred using gravitational waves through GWTC-3," 11 2021.

[20] B. P. Abbott et al., "GW190425: Observation of a Compact Binary Coalescence with Total Mass $\sim 3.4 M_{\odot}$," Astrophys. J. Lett., vol. 892, no. 1, p. L3, 2020.

[21] R. Abbott et al., "GW190814: Gravitational Waves from the Coalescence of a 23 Solar Mass Black Hole with a 2.6 Solar Mass Compact Object," Astrophys. J. Lett., vol. 896, no. 2, p. L44, 2020.

[22] R. Abbott et al., "Observation of Gravitational Waves from Two Neutron Star–Black Hole Coalescences," Astrophys. J. Lett., vol. 915, no. 1, p. L5, 2021.

[23] C. E. Rhoades, Jr. and R. Ruffini, "Maximum mass of a neutron star," Phys. Rev. Lett., vol. 32, pp. 324–327, 1974.

[24] V. Kalogera and G. Baym, "The maximum mass of a neutron star," Astrophys. J. Lett., vol. 470, pp. L61–L64, 1996.

[25] L. Blanchet, T. Damour, B. R. Iyer, C. M. Will, and A. Wiseman, "Gravitational radiation damping of compact binary systems to second postNewtonian order," Phys.Rev.Lett., vol. 74, pp. 3515–3518, 1995.

[26] R. Abbott et al., "Search for intermediate mass black hole binaries in the third observing run of Advanced LIGO and Advanced Virgo," 5 2021.

[27] T. Damour, "Coalescence of two spinning black holes: An effective one- body approach," Phys. Rev., vol. D64, p. 124013, 2001.

[28] P. Ajith, M. Hannam, S. Husa, Y. Chen, B. Brügmann, et al., "Inspiral-merger-ringdown waveforms for black-hole binaries with non-precessing spins," Phys.Rev.Lett., vol. 106, p. 241101, 2011.

[29] L. Blanchet, "Gravitational Radiation from Post-Newtonian Sources and Inspiralling Compact Binaries," Living Rev. Relativity, vol. 17, p. 2, 2014.

[30] M. Pürrer, M. Hannam, and F. Ohme, "Can we measure individual black-hole spins from gravitational-wave observations?," Phys. Rev. D, vol. 93, no. 8, p. 084042, 2016.

[31] M. Hannam, P. Schmidt, A. Bohé, L. Haegel, S. Husa, F. Ohme, G. Pratten, and M. Pürrer, "Simple Model of Complete Precessing Black-Hole-Binary Gravitational Waveforms," Phys. Rev. Lett., vol. 113, no. 15, p. 151101, 2014.

[32] P. Schmidt, F. Ohme, and M. Hannam, "Towards models of gravitational waveforms from generic binaries II: Modelling precession effects with a single effective precession parameter," Phys. Rev., vol. D91, no. 2, p. 024043, 2015.

[33] C. L. Rodriguez, M. Zevin, C. Pankow, V. Kalogera, and F. A. Rasio, "Illuminating Black Hole Binary Formation Channels with Spins in Advanced LIGO," Astrophys. J. Lett., vol. 832, no. 1, p. L2, 2016.

[34] S. Stevenson, C. P. L. Berry, and I. Mandel, "Hierarchical analysis of gravitational-wave measurements of binary black hole spin–orbit misalignments," Mon. Not. Roy. Astron. Soc., vol. 471, no. 3, pp. 2801–2811, 2017.

[35] R. M. O'Leary, F. A. Rasio, J. M. Fregeau, N. Ivanova, and R. W. O'Shaughnessy, "Binary mergers and growth of black holes in dense star clusters," Astrophys. J., vol. 637, pp. 937–951, 2006.

[36] R. M. O'Leary, B. Kocsis, and A. Loeb, "Gravitational waves from scattering of stellar-mass black holes in galactic nuclei," Mon. Not. Roy. Astron. Soc., vol. 395, no. 4, pp. 2127–2146, 2009.

[37] J. Samsing, M. MacLeod, and E. Ramirez-Ruiz, "The Formation of Eccentric Compact Binary Inspirals and the Role of Gravitational Wave Emission in Binary-Single Stellar Encounters," Astrophys. J., vol. 784, p. 71, 2014.

[38] C. L. Rodriguez, S. Chatterjee, and F. A. Rasio, "Binary Black Hole Mergers from Globular Clusters: Masses, Merger Rates, and the Impact of Stellar Evolution," Phys. Rev., vol. D93, no. 8, p. 084029, 2016.

[39] K. Belczynski, D. E. Holz, T. Bulik, and R. O'Shaughnessy, "The first gravitational-wave source from the isolated evolution of two 40-100 Msun stars," Nature, vol. 534, p. 512, 2016.

[40] J. Samsing, "Eccentric Black Hole Mergers Forming in Globular Clusters," Phys. Rev., vol. D97, no. 10, p. 103014, 2018.

[41] B. P. Abbott et al., "Search for Eccentric Binary Black Hole Mergers with Advanced LIGO and Advanced Virgo during their First and Second Observing Runs," Astrophys. J., vol. 883, no. 2, p. 149, 2019.

[42] A. H. Nitz, A. Lenon, and D. A. Brown, "Search for Eccentric Binary Neutron Star Mergers in the first and second observing runs of Advanced LIGO," Astrophys. J., vol. 890, p. 1, 12 2019.

[43] I. M. Romero-Shaw, P. D. Lasky, and E. Thrane, "Searching for Eccentricity: Signatures of Dynamical Formation in the First Gravitational-Wave Transient Catalogue of LIGO and Virgo," Mon. Not. Roy. Astron. Soc., vol. 490, no. 4, pp. 5210–5216, 2019.

[44] J. M. Corral-Santana, J. Casares, T. Munoz-Darias, F. E. Bauer, I. G. Martinez-Pais, and D. M. Russell, "BlackCAT: A catalogue of stellar-mass black holes in X-ray transients," Astron. Astrophys., vol. 587, p. A61, 2016.

[45] N. Yunes and X. Siemens, "Gravitational-Wave Tests of General Relativity with Ground-Based Detectors and Pulsar Timing-Arrays," Living Rev. Rel., vol. 16, p. 9, 2013.

[46] E. Berti et al., "Testing General Relativity with Present and Future Astrophysical Observations," Class. Quant. Grav., vol. 32, p. 243001, 2015.

[47] B. P. Abbott et al., "Tests of general relativity with GW150914," Phys. Rev. Lett., vol. 116, no. 22, p. 221101, 2016. [Erratum: Phys.Rev.Lett. 121, 129902 (2018)].

[48] B. P. Abbott et al., "Tests of General Relativity with the Binary Black Hole Signals from the LIGO-Virgo Catalog GWTC-1," 2019.

[49] G. Carullo, W. Del Pozzo, and J. Veitch, "Observational Black Hole Spectroscopy: A time-domain multimode analysis of GW150914," Phys. Rev. D, vol. 99, no. 12, p. 123029, 2019. [Erratum: Phys.Rev.D 100, 089903 (2019)].

[50] R. Abbott et al., "Tests of General Relativity with GWTC-3," 12 2021.

[51] A. Ghosh, R. Brito, and A. Buonanno, "Constraints on quasinormal-mode frequencies with LIGO-Virgo binary–black-hole observations," Phys. Rev. D, vol. 103, no. 12, p. 124041, 2021.

[52] D. M. Eardley, D. L. Lee, and A. P. Lightman, "Gravitational-wave observations as a tool for testing relativistic gravity," Phys. Rev. D, vol. 8, pp. 3308–3321, 1973.

[53] C. Corda, "Interferometric detection of gravitational waves: the definitive test for General Relativity," Int. J. Mod. Phys. D, vol. 18, pp. 2275–2282, 2009.

[54] C. M. Will, "The Confrontation between General Relativity and Experiment," Living Rev. Rel., vol. 17, p. 4, 2014.

[55] M. Isi and A. J. Weinstein, "Probing gravitational wave polarizations with signals from compact binary coalescences," 10 2017.

[56] A. Samajdar and K. G. Arun, "Projected constraints on the dispersion of gravitational waves using advanced ground- and space-based interferometers," Phys. Rev. D, vol. 96, no. 10, p. 104027, 2017.

[57] A. Toubiana, S. Marsat, E. Barausse, S. Babak, and J. Baker, "Tests of general relativity with stellar-mass black hole binaries observed by LISA," Phys. Rev. D, vol. 101, no. 10, p. 104038, 2020.

[58] S. Borhanian and B. S. Sathyaprakash, "Listening to the Universe with Next Generation Ground-Based Gravitational-Wave Detectors," 2 2022.

[59] E. Berti, V. Cardoso, and C. M. Will, "On gravitational-wave spectroscopy of massive black holes with the space interferometer LISA," Phys. Rev., vol. D73, p. 064030, 2006.

[60] E. Berti, K. Yagi, H. Yang, and N. Yunes, "Extreme Gravity Tests with Gravitational Waves from Compact Binary Coalescences: (II) Ringdown," Gen. Rel. Grav., vol. 50, no. 5, p. 49, 2018.

[61] L. Barack et al., "Black holes, gravitational waves and fundamental physics: a roadmap," Class. Quant. Grav., vol. 36, no. 14, p. 143001, 2019.

[62] E. Barausse et al., "Prospects for Fundamental Physics with LISA," Gen. Rel. Grav., vol. 52, no. 8, p. 81, 2020.

[63] B. P. Abbott et al., "A Gravitational-wave Measurement of the Hubble Constant Following the Second Observing Run of Advanced LIGO and Virgo," Astrophys. J., vol. 909, no. 2, p. 218, 2021. [Erratum: Astrophys.J. 923, 279 (2021)].

[64] L. Verde, T. Treu, and A. G. Riess, "Tensions between the Early and the Late Universe," Nature Astron., vol. 3, p. 891, 7 2019.

[65] J. M. Lattimer, "The nuclear equation of state and neutron star masses," Ann. Rev. Nucl. Part. Sci., vol. 62, pp. 485–515, 2012.

[66] L. Baiotti, "Gravitational waves from neutron star mergers and their relation to the nuclear equation of state," Prog. Part. Nucl. Phys., vol. 109, p. 103714, 2019.

[67] D. Radice, A. Perego, F. Zappa, and S. Bernuzzi, "GW170817: Joint Constraint on the Neutron Star Equation of State from Multimessenger Observations," Astrophys. J., vol. 852, no. 2, p. L29, 2018.

[68] R. Essick, P. Landry, and D. E. Holz, "Nonparametric Inference of Neutron Star Composition, Equation of State, and Maximum Mass with GW170817," Phys. Rev. D, vol. 101, no. 6, p. 063007, 2020.

[69] B. P. Abbott et al., "Model comparison from LIGO–Virgo data on GW170817's binary components and consequences for the merger remnant," Class. Quant. Grav., vol. 37, no. 4, p. 045006, 2020.

[70] B. P. Abbott et al., "GW170817: Measurements of neutron star radii and equation of state," Phys. Rev. Lett., vol. 121, no. 16, p. 161101, 2018.

[71] B. P. Abbott et al., "Gravitational Waves and Gamma-rays from a Binary Neutron Star Merger: GW170817 and GRB 170817A," Astrophys. J. Lett., vol. 848, no. 2, p. L13, 2017.

[72] A. Goldstein et al., "An Ordinary Short Gamma-Ray Burst with Extraordinary Implications: Fermi-GBM Detection of GRB 170817A," Astrophys. J., vol. 848, no. 2, p. L14, 2017.

[73] E. Troja et al., "The X-ray counterpart to the gravitational wave event GW 170817," Nature, 2017.

[74] V. Savchenko et al., "INTEGRAL Detection of the First Prompt Gamma-Ray Signal Coincident with the Gravitational-wave Event GW170817," Astrophys. J., vol. 848, no. 2, p. L15, 2017.

[75] G. Hallinan et al., "A Radio Counterpart to a Neutron Star Merger," 2017.

[76] R. Margutti et al., "The Binary Neutron Star Event LIGO/Virgo GW170817 160 Days after Merger: Synchrotron Emission across the Electromagnetic Spectrum," Astrophys. J., vol. 856, no. 1, p. L18, 2018.

[77] J. D. Lyman et al., "The optical afterglow of the short gamma-ray burst associated with GW170817," Nat. Astron., vol. 2, no. 9, pp. 751–754, 2018.

[78] K. P. Mooley, A. T. Deller, O. Gottlieb, E. Nakar, G. Hallinan, S. Bourke, D. A. Frail, A. Horesh, A. Corsi, and K. Hotokezaka, "Superluminal motion of a relativistic jet in the neutron-star merger GW170817," Nature, vol. 561, no. 7723, pp. 355–359, 2018.

[79] G. Ghirlanda et al., "Compact radio emission indicates a structured jet was produced by a binary neutron star merger," Science, vol. 363, p. 968, 2019.

[80] P. S. Cowperthwaite et al., "The Electromagnetic Counterpart of the Binary Neutron Star Merger LIGO/Virgo GW170817. II. UV, Optical, and Near-infrared Light Curves and Comparison to Kilonova Models," Astrophys. J., vol. 848, no. 2, p. L17, 2017.

[81] D. Kasen, B. Metzger, J. Barnes, E. Quataert, and E. Ramirez-Ruiz, "Origin of the heavy elements in binary neutron-star mergers from a gravitational wave event," Nature, 2017. [Nature551,80(2017)].

[82] M. Soares-Santos et al., "The Electromagnetic Counterpart of the Binary Neutron Star Merger LIGO/Virgo GW170817. I. Dark Energy Camera Discovery of the Optical Counterpart," Astrophys. J., vol. 848, no. 2, p. L16, 2017.

[83] S. Valenti, D. J. Sand, S. Yang, E. Cappellaro, L. Tartaglia, A. Corsi, S. W. Jha, D. E. Reichart, J. Haislip, and V. Kouprianov, "The discovery of the electromagnetic counterpart of GW170817: kilonova AT 2017gfo/DLT17ck," Astrophys. J., vol. 848, no. 2, p. L24, 2017.

[84] I. Arcavi et al., "Optical emission from a kilonova following a gravitational-wave-detected neutron-star merger," Nature, vol. 551, p. 64, 2017.

[85] N. R. Tanvir et al., "The Emergence of a Lanthanide-Rich Kilonova Following the Merger of Two Neutron Stars," Astrophys. J., vol. 848, p. L27, 2017.

[86] P. A. Evans et al., "Swift and NuSTAR observations of GW170817: detection of a blue kilonova," 2017.

[87] M. R. Drout et al., "Light Curves of the Neutron Star Merger GW170817/SSS17a: Implications for R-Process Nucleosynthesis," 2017.

[88] R. Chornock et al., "The Electromagnetic Counterpart of the Binary Neutron Star Merger LIGO/VIRGO GW170817. IV. Detection of Near-infrared Signatures of r-process Nucleosynthesis with Gemini-South," Astrophys. J., vol. 848, no. 2, p. L19, 2017.

[89] M. M. Kasliwal et al., "Illuminating Gravitational Waves: A Concordant Picture of Photons from a Neutron Star Merger," 2017.

[90] E. Pian et al., "Spectroscopic identification of r-process nucleosynthesis in a double neutron star merger," Nature, 2017.

[91] S. J. Smartt et al., "A kilonova as the electromagnetic counterpart to a gravitational-wave source," Nature, 2017.

[92] D. Watson et al., "Identification of strontium in the merger of two neutron stars," Nature, vol. 574, no. 7779, pp. 497–500, 2019.

[93] B. F. Schutz, "Determining the Hubble Constant from Gravitational Wave Observations," Nature, vol. 323, pp. 310–311, 1986.

[94] B. P. Abbott et al., "A gravitational-wave standard siren measurement of the Hubble constant," Nature, vol. 551, no. 7678, pp. 85–88, 2017.

[95] K. Hotokezaka, E. Nakar, O. Gottlieb, S. Nissanke, K. Masuda, G. Hallinan, K. P. Mooley, and A. T. Deller, "A Hubble constant measurement from superluminal motion of the jet in GW170817," Nature Astron., vol. 3, no. 10, pp. 940–944, 2019.

[96] V. Cardoso and P. Pani, "Testing the nature of dark compact objects: a status report," Living Rev. Rel., vol. 22, no. 1, p. 4, 2019.

[97] B. Carr and F. Kuhnel, "Primordial Black Holes as Dark Matter: Recent Developments," Ann. Rev. Nucl. Part. Sci., vol. 70, pp. 355–394, 2020.

[98] R. Penrose and R. M. Floyd, "Extraction of rotational energy from a black hole," Nature, vol. 229, pp. 177–179, 1971.

[99] B. S. Sathyaprakash and S. V. Dhurandhar, "Choice of filters for the detection of gravitational waves from coalescing binaries," Phys. Rev., vol. D44, pp. 3819–3834, 1991.

[100] B. Allen, W. G. Anderson, P. R. Brady, D. A. Brown, and J. D. E. Creighton, "FINDCHIRP: An Algorithm for detection of gravitational waves from inspiraling compact binaries," Phys. Rev., vol. D85, p. 122006, 2012.

[101] S. Babak et al., "Searching for gravitational waves from binary coalescence," Phys. Rev. D, vol. 87, no. 2, p. 024033, 2013.

[102] S. A. Usman et al., "The PyCBC search for gravitational waves from compact binary coalescence," Class. Quant. Grav., vol. 33, no. 21, p. 215004, 2016.

[103] T. Bayes, Rev., "An essay toward solving a problem in the doctrine of chances," Phil. Trans. Roy. Soc. Lond., vol. 53, pp. 370–418, 1764.

[104] J. Veitch et al., "Parameter estimation for compact binaries with ground-based gravitational-wave observations using the LALInference software library," Phys. Rev., vol. D91, no. 4, p. 042003, 2015.

[105] T. B. Littenberg and N. J. Cornish, "Bayesian inference for spectral estimation of gravitational wave detector noise," Phys. Rev. D, vol. 91, no. 8, p. 084034, 2015.

[106] N. J. Cornish and T. B. Littenberg, "BayesWave: Bayesian Inference for Gravitational Wave Bursts and Instrument Glitches," Class. Quant. Grav., vol. 32, no. 13, p. 135012, 2015.

[107] C. Biwer, C. D. Capano, S. De, M. Cabero, D. A. Brown, A. H. Nitz, and V. Raymond, "PyCBC Inference: A Python-based parameter estimation toolkit for compact binary coalescence signals," Publ. Astron. Soc. Pac., vol. 131, no. 996, p. 024503, 2019.

[108] G. Ashton et al., "BILBY: A user-friendly Bayesian inference library for gravitational-wave astronomy," Astrophys. J. Suppl., vol. 241, no. 2, p. 27, 2019.

[109] R. J. E. Smith, G. Ashton, A. Vajpeyi, and C. Talbot, "Massively parallel Bayesian inference for transient gravitational-wave astronomy," Mon. Not. Roy. Astron. Soc., vol. 498, no. 3, pp. 4492–4502, 2020.

[110] I. M. Romero-Shaw et al., "Bayesian inference for compact binary coalescences with bilby: validation and application to the first LIGO–Virgo gravitational-wave transient catalogue," Mon. Not. Roy. Astron. Soc., vol. 499, no. 3, pp. 3295–3319, 2020.

[111] F. Pretorius, "Evolution of binary black hole spacetimes," Phys. Rev. Lett., vol. 95, p. 121101, 2005.

[112] M. Campanelli, C. O. Lousto, P. Marronetti, and Y. Zlochower, "Accurate Evolutions of Orbiting Black-Hole Binaries Without Excision," Phys. Rev. Lett., vol. 96, p. 111101, 2006.

[113] A. H. Mroue, M. A. Scheel, B. Szilagyi, H. P. Pfeiffer, M. Boyle, et al., "A catalog of 174 binary black-hole simulations for gravitational-wave astronomy," Phys.Rev.Lett., vol. 111, p. 241104, 2013.

[114] S. Husa, S. Khan, M. Hannam, M. Pürrer, F. Ohme, X. Jiménez Forteza, and A. Bohé, "Frequency-domain gravitational waves from nonprecessing black-hole binaries. I. New numerical waveforms and anatomy of the signal," Phys. Rev., vol. D93, no. 4, p. 044006, 2016.

[115] K. Jani, J. Healy, J. A. Clark, L. London, P. Laguna, and D. Shoemaker, "Georgia Tech Catalog of Gravitational Waveforms," Class. Quant. Grav., vol. 33, no. 20, p. 204001, 2016.

[116] M. Boyle et al., "The SXS Collaboration catalog of binary black hole simulations," Class. Quant. Grav., vol. 36, no. 19, p. 195006, 2019.

[117] J. Healy, C. O. Lousto, J. Lange, R. O'Shaughnessy, Y. Zlochower, and M. Campanelli, "Second RIT binary black hole simulations catalog and its application to gravitational waves parameter estimation," Phys. Rev. D, vol. 100, no. 2, p. 024021, 2019.

[118] I. Hinder, L. E. Kidder, and H. P. Pfeiffer, "An eccentric binary black hole inspiral-merger-ringdown gravitational waveform model from numerical relativity and post-Newtonian theory," 2017.

[119] B. Szilágyi, J. Blackman, A. Buonanno, A. Taracchini, H. P. Pfeiffer, M. A. Scheel, T. Chu, L. E. Kidder, and Y. Pan, "Approaching the Post-Newtonian

Regime with Numerical Relativity: A Compact-Object Binary Simulation Spanning 350 Gravitational-Wave Cycles," Phys. Rev. Lett., vol. 115, no. 3, p. 031102, 2015.

[120] E. A. Huerta et al., "Physics of eccentric binary black hole mergers: A numerical relativity perspective," Phys. Rev., vol. D100, no. 6, p. 064003, 2019.

[121] S. E. Field, C. R. Galley, J. S. Hesthaven, J. Kaye, and M. Tiglio, "Fast prediction and evaluation of gravitational waveforms using surrogate models," Phys.Rev., vol. X4, no. 3, p. 031006, 2014.

[122] J. Blackman, S. E. Field, M. A. Scheel, C. R. Galley, D. A. Hemberger, P. Schmidt, and R. Smith, "A Surrogate Model of Gravitational Waveforms from Numerical Relativity Simulations of Precessing Binary Black Hole Mergers," Phys. Rev., vol. D95, no. 10, p. 104023, 2017.

[123] V. Varma, S. E. Field, M. A. Scheel, J. Blackman, D. Gerosa, L. C. Stein, L. E. Kidder, and H. P. Pfeiffer, "Surrogate models for precessing binary black hole simulations with unequal masses," Phys. Rev. Research., vol. 1, p. 033015, 2019.

[124] S. Rosswog, "The multi-messenger picture of compact binary mergers," Int.J.Mod.Phys., vol. D24, no. 05, p. 1530012, 2015.

[125] M. Shibata and K. Taniguchi, "Coalescence of Black Hole-Neutron Star Binaries," Living Rev. Rel., vol. 14, p. 6, 2011.

[126] S. Bernuzzi, A. Nagar, T. Dietrich, and T. Damour, "Modeling the Dynamics of Tidally Interacting Binary Neutron Stars up to the Merger," Phys.Rev.Lett., vol. 114, no. 16, p. 161103, 2015.

[127] L. Baiotti and L. Rezzolla, "Binary neutron star mergers: a review of Einstein's richest laboratory," Rept. Prog. Phys., vol. 80, no. 9, p. 096901, 2017.

[128] V. Paschalidis, "General relativistic simulations of compact binary mergers as engines for short gamma-ray bursts," Class. Quant. Grav., vol. 34, no. 8, p. 084002, 2017.

[129] A. Einstein, L. Infeld, and B. Hoffmann, "The Gravitational equations and the problem of motion," Annals Math., vol. 39, pp. 65–100, 1938.

[130] L. Blanchet and T. Damour, "Postnewtonian generation of gravitational waves," Annales Poincare Phys.Theor., vol. 50, pp. 377–408, 1989.

[131] T. Damour, P. Jaranowski, and G. Schäfer, "Nonlocal-in-time action for the fourth post-Newtonian conservative dynamics of two-body systems," Phys. Rev., vol. D89, no. 6, p. 064058, 2014.

[132] M. Levi and J. Steinhoff, "Next-to-next-to-leading order gravitational spin-orbit coupling via the effective field theory for spinning objects in the post-Newtonian scheme," JCAP, vol. 1601, p. 011, 2016.

[133] G. Schaefer and P. Jaranowski, "Hamiltonian formulation of general relativity and post-Newtonian dynamics of compact binaries," Living Rev. Rel., vol. 21, no. 1, p. 7, 2018.

[134] D. Bini, T. Damour, and A. Geralico, "Novel approach to binary dynamics: application to the fifth post-Newtonian level," Phys. Rev. Lett., vol. 123, no. 23, p. 231104, 2019.

[135] D. Bini, T. Damour, and A. Geralico, "Binary dynamics at the fifth and fifth-and-a-half post-Newtonian orders," Phys. Rev. D, vol. 102, no. 2, p. 024062, 2020.

[136] D. Bini, T. Damour, and A. Geralico, "Sixth post-Newtonian local-in-time dynamics of binary systems," Phys. Rev. D, vol. 102, no. 2, p. 024061, 2020.

[137] D. Bini, T. Damour, and A. Geralico, "Sixth post-Newtonian nonlocal-in-time dynamics of binary systems," 7 2020.

[138] A. Antonelli, C. Kavanagh, M. Khalil, J. Steinhoff, and J. Vines, "Gravitational spin-orbit and aligned spin_1-spin_2 couplings through third-subleading post-Newtonian orders," Phys. Rev. D, vol. 102, p. 124024, 2020.

[139] L. Bel, T. Damour, N. Deruelle, J. Ibanez, and J. Martin, "Poincaré-invariant gravitational field and equations of motion of two pointlike objects: The postlinear approximation of general relativity," Gen. Rel. Grav., vol. 13, pp. 963–1004, 1981.

[140] T. Ledvinka, G. Schaefer, and J. Bicak, "Relativistic Closed-Form Hamiltonian for Many-Body Gravitating Systems in the Post-Minkowskian Approximation," Phys. Rev. Lett., vol. 100, p. 251101, 2008.

[141] T. Damour, "High-energy gravitational scattering and the general relativistic two-body problem," Phys. Rev., vol. D97, no. 4, p. 044038, 2018.

[142] C. Cheung, I. Z. Rothstein, and M. P. Solon, "From Scattering Amplitudes to Classical Potentials in the Post-Minkowskian Expansion," Phys. Rev. Lett., vol. 121, no. 25, p. 251101, 2018.

[143] T. Damour, "Gravitational scattering, post-Minkowskian approximation and Effective One-Body theory," Phys. Rev., vol. D94, no. 10, p. 104015, 2016.

[144] T. Damour, "Classical and quantum scattering in post-Minkowskian gravity," Phys. Rev. D, vol. 102, no. 2, p. 024060, 2020.

[145] Z. Bern, C. Cheung, R. Roiban, C.-H. Shen, M. P. Solon, and M. Zeng, "Scattering Amplitudes and the Conservative Hamiltonian for Binary Systems at Third Post-Minkowskian Order," Phys. Rev. Lett., vol. 122, no. 20, p. 201603, 2019.

[146] T. Damour, "Radiative contribution to classical gravitational scattering at the third order in G," Phys. Rev. D, vol. 102, no. 12, p. 124008, 2020.

[147] Z. Bern, J. Parra-Martinez, R. Roiban, M. S. Ruf, C.-H. Shen, M. P. Solon, and M. Zeng, "Scattering Amplitudes and Conservative Binary Dynamics at $\mathcal{O}(G^4)$," Phys. Rev. Lett., vol. 126, no. 17, p. 171601, 2021.

[148] A. V. Manohar, A. K. Ridgway, and C.-H. Shen, "Radiated Angular Momentum and Dissipative Effects in Classical Scattering," 3 2022.

[149] T. Tanaka, Y. Mino, M. Sasaki, and M. Shibata, "Gravitational waves from a spinning particle in circular orbits around a rotating black hole," Phys.Rev., vol. D54, pp. 3762–3777, 1996.

[150] Y. Mino, M. Sasaki, and T. Tanaka, "Gravitational radiation reaction to a particle motion," Phys.Rev., vol. D55, pp. 3457–3476, 1997.

[151] E. Poisson, A. Pound, and I. Vega, "The Motion of point particles in curved spacetime," Living Rev.Rel., vol. 14, p. 7, 2011.

[152] L. Barack and A. Pound, "Self-force and radiation reaction in general relativity," Rept. Prog. Phys., vol. 82, no. 1, p. 016904, 2019.

[153] A. Pound, B. Wardell, N. Warburton, and J. Miller, "Second-Order Self-Force Calculation of Gravitational Binding Energy in Compact Binaries," Phys. Rev. Lett., vol. 124, no. 2, p. 021101, 2020.

[154] A. Antonelli, C. Kavanagh, M. Khalil, J. Steinhoff, and J. Vines, "Gravitational spin-orbit coupling through third-subleading post-Newtonian order: from first-order self-force to arbitrary mass ratios," Phys. Rev. Lett., vol. 125, no. 1, p. 011103, 2020.

[155] M. van de Meent and H. P. Pfeiffer, "Intermediate mass-ratio black hole binaries: Applicability of small mass-ratio perturbation theory," Phys. Rev. Lett., vol. 125, no. 18, p. 181101, 2020.

[156] J. Mathews, A. Pound, and B. Wardell, "Self-force calculations with a spinning secondary," Phys. Rev. D, vol. 105, no. 8, p. 084031, 2022.

[157] S. A. Teukolsky, "Perturbations of a rotating black hole. 1. Fundamental equations for gravitational electromagnetic and neutrino field perturbations," Astrophys. J., vol. 185, pp. 635–647, 1973.

[158] K. D. Kokkotas and B. G. Schmidt, "Quasi-normal modes of stars and black holes," Living Rev. Rel., vol. 2, p. 2, 1999.

[159] L. London, D. Shoemaker, and J. Healy, "Modeling ringdown: Beyond the fundamental quasinormal modes," Phys. Rev., vol. D90, no. 12, p. 124032, 2014. [Erratum: Phys. Rev.D94,no.6,069902(2016)].

[160] T. Damour and A. Nagar, "Relativistic tidal properties of neutron stars," Phys. Rev., vol. D80, p. 084035, 2009.

[161] T. Hinderer, "Tidal Love numbers of neutron stars," Astrophys.J., vol. 677, pp. 1216–1220, 2008.

[162] E. E. Flanagan and T. Hinderer, "Constraining neutron star tidal Love numbers with gravitational wave detectors," Phys.Rev., vol. D77, p. 021502, 2008.

[163] A. Buonanno and T. Damour, "Effective one-body approach to general relativistic two-body dynamics," Phys. Rev., vol. D59, p. 084006, 1999.

[164] A. Buonanno and T. Damour, "Transition from inspiral to plunge in binary black hole coalescences," Phys. Rev., vol. D62, p. 064015, 2000.

[165] T. Damour, P. Jaranowski, and G. Schaefer, "On the determination of the last stable orbit for circular general relativistic binaries at the third post-Newtonian approximation," Phys. Rev., vol. D62, p. 084011, 2000.

[166] A. Nagar et al., "Time-domain effective-one-body gravitational waveforms for coalescing compact binaries with nonprecessing spins, tides and self-spin effects," Phys. Rev., vol. D98, no. 10, p. 104052, 2018.

[167] R. Cotesta, A. Buonanno, A. Bohé, A. Taracchini, I. Hinder, and S. Ossokine, "Enriching the Symphony of Gravitational Waves from Binary Black Holes by Tuning Higher Harmonics," Phys. Rev., vol. D98, no. 8, p. 084028, 2018.

[168] R. Gamba, S. Akçay, S. Bernuzzi, and J. Williams, "Effective-one-body waveforms for precessing coalescing compact binaries with post-Newtonian Twist," 11 2021.

[169] S. Ossokine et al., "Multipolar Effective-One-Body Waveforms for Precessing Binary Black Holes: Construction and Validation," Phys. Rev. D, vol. 102, no. 4, p. 044055, 2020.

[170] D. Chiaramello and A. Nagar, "Faithful analytical effective-one-body waveform model for spin-aligned, moderately eccentric, coalescing black hole binaries," Phys. Rev. D, vol. 101, no. 10, p. 101501, 2020.

[171] A. Nagar, A. Bonino, and P. Rettegno, "Effective one-body multipolar waveform model for spin-aligned, quasicircular, eccentric, hyperbolic black hole binaries," Phys. Rev. D, vol. 103, no. 10, p. 104021, 2021.

[172] A. Placidi, S. Albanesi, A. Nagar, M. Orselli, S. Bernuzzi, and G. Grignani, "Exploiting Newton-factorized, 2PN-accurate, waveform multipoles in effective-one-body models for spin-aligned noncircularized binaries," 12 2021.

[173] M. Khalil, A. Buonanno, J. Steinhoff, and J. Vines, "Radiation-reaction force and multipolar waveforms for eccentric, spin-aligned binaries in the effective-one-body formalism," Phys. Rev. D, vol. 104, no. 2, p. 024046, 2021.

[174] A. Ramos-Buades, A. Buonanno, M. Khalil, and S. Ossokine, "Effective-one-body multipolar waveforms for eccentric binary black holes with nonprecessing spins," Phys. Rev. D, vol. 105, no. 4, p. 044035, 2022.

[175] B. D. Lackey, M. Pürrer, A. Taracchini, and S. Marsat, "Surrogate model for an aligned-spin effective one body waveform model of binary neutron star inspirals using Gaussian process regression," Phys. Rev. D, vol. 100, no. 2, p. 024002, 2019.

[176] R. Cotesta, S. Marsat, and M. Pürrer, "Frequency domain reduced order model of aligned-spin effective-one-body waveforms with higher-order modes," Phys. Rev. D, vol. 101, no. 12, p. 124040, 2020.

[177] S. Schmidt, M. Breschi, R. Gamba, G. Pagano, P. Rettegno, G. Riemenschneider, S. Bernuzzi, A. Nagar, and W. Del Pozzo, "Machine Learning Gravitational Waves from Binary Black Hole Mergers," Phys. Rev. D, vol. 103, p. 043020, 2021.

[178] G. Riemenschneider, P. Rettegno, M. Breschi, A. Albertini, R. Gamba, S. Bernuzzi, and A. Nagar, "Assessment of consistent next-to-quasicircular corrections and postadiabatic approximation in effective-one-body multipolar waveforms for binary black hole coalescences," Phys. Rev. D, vol. 104, no. 10, p. 104045, 2021.

[179] A. Nagar and P. Rettegno, "Efficient effective one body time-domain gravitational waveforms," Phys. Rev., vol. D99, no. 2, p. 021501, 2019.

[180] R. Gamba, S. Bernuzzi, and A. Nagar, "Fast, faithful, frequency-domain effective-one-body waveforms for compact binary coalescences," Phys. Rev. D, vol. 104, no. 8, p. 084058, 2021.

[181] D. P. Mihaylov, S. Ossokine, A. Buonanno, and A. Ghosh, "Fast post-adiabatic waveforms in the time domain: Applications to compact binary coalescences in LIGO and Virgo," Phys. Rev. D, vol. 104, no. 12, p. 124087, 2021.

[182] P. Ajith, S. Babak, Y. Chen, M. Hewitson, B. Krishnan, et al., "Phenomenological template family for black-hole coalescence waveforms," Class.Quant.Grav., vol. 24, pp. S689–S700, 2007.

[183] L. Santamaria, F. Ohme, P. Ajith, B. Brügmann, N. Dorband, et al., "Matching post-Newtonian and numerical relativity waveforms: systematic errors and a new phenomenological model for non-precessing black hole binaries," Phys.Rev., vol. D82, p. 064016, 2010.

[184] S. Khan, K. Chatziioannou, M. Hannam, and F. Ohme, "Phenomenological model for the gravitational-wave signal from precessing binary black holes with two-spin effects," Phys. Rev., vol. D100, no. 2, p. 024059, 2019.

[185] G. Pratten et al., "Computationally efficient models for the dominant and subdominant harmonic modes of precessing binary black holes," Phys. Rev. D, vol. 103, no. 10, p. 104056, 2021.

[186] G. Pratten, S. Husa, C. Garcia-Quiros, M. Colleoni, A. Ramos-Buades, H. Estelles, and R. Jaume, "Setting the cornerstone for a family of models for gravitational waves from compact binaries: The dominant harmonic for nonprecessing quasicircular black holes," Phys. Rev. D, vol. 102, no. 6, p. 064001, 2020.

[187] C. García-Quirós, M. Colleoni, S. Husa, H. Estellés, G. Pratten, A. Ramos-Buades, M. Mateu-Lucena, and R. Jaume, "Multimode frequency-domain model for the gravitational wave signal from nonprecessing black-hole binaries," Phys. Rev. D, vol. 102, no. 6, p. 064002, 2020.

[188] S. Khan, F. Ohme, K. Chatziioannou, and M. Hannam, "Including higher order multipoles in gravitational-wave models for precessing binary black holes," 2019.

[189] A. Albertini, A. Nagar, P. Rettegno, S. Albanesi, and R. Gamba, "Waveforms and fluxes: Towards a self-consistent effective one body waveform model for nonprecessing, coalescing black-hole binaries for third generation detectors," 11 2021.

[190] T. Damour and A. Nagar, "New effective-one-body description of coalescing nonprecessing spinning black-hole binaries," Phys.Rev., vol. D90, no. 4, p. 044018, 2014.

[191] A. Nagar, T. Damour, C. Reisswig, and D. Pollney, "Energetics and phasing of nonprecessing spinning coalescing black hole binaries," Phys. Rev., vol. D93, no. 4, p. 044046, 2016.

[192] A. Nagar, G. Riemenschneider, and G. Pratten, "Impact of Numerical Relativity information on effective-one-body waveform models," Phys. Rev., vol. D96, no. 8, p. 084045, 2017.

[193] S. Akcay, S. Bernuzzi, F. Messina, A. Nagar, N. Ortiz, and P. Rettegno, "Effective-one-body multipolar waveform for tidally interacting binary neutron stars up to merger," Phys. Rev., vol. D99, no. 4, p. 044051, 2019.

[194] A. Nagar, F. Messina, P. Rettegno, D. Bini, T. Damour, A. Geralico, S. Akcay, and S. Bernuzzi, "Nonlinear-in-spin effects in effective-one-body waveform models of spin-aligned, inspiralling, neutron star binaries," Phys. Rev., vol. D99, p. 044007, 2019.

[195] A. Nagar, G. Pratten, G. Riemenschneider, and R. Gamba, "A Multipolar Effective One Body Model for Non-Spinning Black Hole Binaries," 2019.

[196] A. Nagar, G. Riemenschneider, G. Pratten, P. Rettegno, and F. Messina, "Multipolar effective one body waveform model for spin-aligned black hole binaries," Phys. Rev. D, vol. 102, no. 2, p. 024077, 2020.

[197] E. Barausse and A. Buonanno, "An Improved effective-one-body Hamiltonian for spinning black-hole binaries," Phys.Rev., vol. D81, p. 084024, 2010.

[198] E. Barausse, E. Racine, and A. Buonanno, "Hamiltonian of a spinning test-particle in curved spacetime," Phys. Rev., vol. D80, p. 104025, 2009.

[199] E. Barausse and A. Buonanno, "Extending the effective-one-body Hamiltonian of black-hole binaries to include next-to-next-to-leading spin-orbit couplings," Phys.Rev., vol. D84, p. 104027, 2011.

[200] A. Taracchini, A. Buonanno, Y. Pan, T. Hinderer, M. Boyle, et al., "Effective-one-body model for black-hole binaries with generic mass ratios and spins," Phys.Rev., vol. D89, no. 6, p. 061502, 2014.

[201] T. Hinderer et al., "Periastron advance in spinning black hole binaries: comparing effective-one-body and Numerical Relativity," Phys. Rev., vol. D88, no. 8, p. 084005, 2013.

[202] Y. Pan, A. Buonanno, A. Taracchini, L. E. Kidder, A. H. Mroue, et al., "Inspiral-merger-ringdown waveforms of spinning, precessing black-hole binaries in the effective-one-body formalism," Phys.Rev., vol. D89, p. 084006, 2014.

[203] S. Babak, A. Taracchini, and A. Buonanno, "Validating the effective-one-body model of spinning, precessing binary black holes against numerical relativity," Phys. Rev., vol. D95, no. 2, p. 024010, 2017.

[204] A. Bohé et al., "Improved effective-one-body model of spinning, nonprecessing binary black holes for the era of gravitational-wave astrophysics with advanced detectors," Phys. Rev., vol. D95, no. 4, p. 044028, 2017.

[205] T. Hinderer et al., "Effects of neutron-star dynamic tides on gravitational waveforms within the effective-one-body approach," Phys. Rev. Lett., vol. 116, no. 18, p. 181101, 2016.

[206] J. Steinhoff, T. Hinderer, A. Buonanno, and A. Taracchini, "Dynamical Tides in General Relativity: Effective Action and Effective-One-Body Hamiltonian," Phys. Rev., vol. D94, no. 10, p. 104028, 2016.

[207] S. Albanesi, A. Nagar, and S. Bernuzzi, "Effective one-body model for extreme-mass-ratio spinning binaries on eccentric equatorial orbits: Testing radiation reaction and waveform," Phys. Rev. D, vol. 104, no. 2, p. 024067, 2021.

[208] X. Liu, Z. Cao, and Z.-H. Zhu, "A higher-multipole gravitational waveform model for an eccentric binary black holes based on the effective-one-body-numerical-relativity formalism," 2 2021.

[209] J. C. Bustillo, N. Sanchis-Gual, A. Torres-Forné, and J. A. Font, "Confusing Head-On Collisions with Precessing Intermediate-Mass Binary Black Hole Mergers," Phys. Rev. Lett., vol. 126, no. 20, p. 201101, 2021.

[210] A. Taracchini, Y. Pan, A. Buonanno, E. Barausse, M. Boyle, et al., "Prototype effective-one-body model for nonprecessing spinning inspiral-merger-ringdown waveforms," Phys.Rev., vol. D86, p. 024011, 2012.

[211] T. Damour, B. R. Iyer, and A. Nagar, "Improved resummation of post-Newtonian multipolar waveforms from circularized compact binaries," Phys. Rev., vol. D79, p. 064004, 2009.

[212] Y. Pan, A. Buonanno, R. Fujita, E. Racine, and H. Tagoshi, "Post-Newtonian factorized multipolar waveforms for spinning, non-precessing black-hole binaries," Phys.Rev., vol. D83, p. 064003, 2011.

[213] A. Taracchini, A. Buonanno, S. A. Hughes, and G. Khanna, "Modeling the horizon-absorbed gravitational flux for equatorial-circular orbits in Kerr spacetime," Phys.Rev., vol. D88, p. 044001, 2013.

[214] A. Nagar and A. Shah, "Factorization and resummation: A new paradigm to improve gravitational wave amplitudes," Phys. Rev., vol. D94, no. 10, p. 104017, 2016.

[215] F. Messina, A. Maldarella, and A. Nagar, "Factorization and resummation: A new paradigm to improve gravitational wave amplitudes. II: the higher multipolar modes," Phys. Rev., vol. D97, no. 8, p. 084016, 2018.

[216] A. Nagar, F. Messina, C. Kavanagh, G. Lukes-Gerakopoulos, N. Warburton, S. Bernuzzi, and E. Harms, "Factorization and resummation: A new

paradigm to improve gravitational wave amplitudes. III: the spinning test-body terms," Phys. Rev., vol. D100, no. 10, p. 104056, 2019.

[217] A. Buonanno, Y. Pan, H. P. Pfeiffer, M. A. Scheel, L. T. Buchman, and L. E. Kidder, "Effective-one-body waveforms calibrated to numerical relativity simulations: Coalescence of non-spinning, equal-mass black holes," Phys. Rev. D, vol. 79, p. 124028, 2009.

[218] Y. Pan, A. Buonanno, L. T. Buchman, T. Chu, L. E. Kidder, et al., "Effective-one-body waveforms calibrated to numerical relativity simulations: coalescence of non-precessing, spinning, equal-mass black holes," Phys.Rev., vol. D81, p. 084041, 2010.

[219] T. Damour, A. Nagar, and S. Bernuzzi, "Improved effective-one-body description of coalescing nonspinning black-hole binaries and its numerical-relativity completion," Phys.Rev., vol. D87, p. 084035, 2013.

[220] Y. Pan, A. Buonanno, M. Boyle, L. T. Buchman, L. E. Kidder, et al., "Inspiral-merger-ringdown multipolar waveforms of nonspinning black-hole binaries using the effective-one-body formalism," Phys.Rev., vol. D84, p. 124052, 2011.

[221] T. Damour and A. Nagar, "A new analytic representation of the ringdown waveform of coalescing spinning black hole binaries," Phys.Rev., vol. D90, p. 024054, 2014.

[222] W. Del Pozzo and A. Nagar, "Analytic family of post-merger template waveforms," Phys. Rev. D, vol. 95, no. 12, p. 124034, 2017.

[223] M. Levi and J. Steinhoff, "Next-to-next-to-leading order gravitational spin-squared potential via the effective field theory for spinning objects in the post-Newtonian scheme," JCAP, vol. 1601, p. 008, 2016.

[224] S. Balmelli and T. Damour, "New effective-one-body Hamiltonian with next-to-leading order spin-spin coupling," Phys. Rev., vol. D92, no. 12, p. 124022, 2015.

[225] T. Damour, P. Jaranowski, and G. Schäfer, "Effective one body approach to the dynamics of two spinning black holes with next-to-leading order spin-orbit coupling," Phys.Rev., vol. D78, p. 024009, 2008.

[226] A. Nagar and S. Akcay, "Horizon-absorbed energy flux in circularized, nonspinning black-hole binaries and its effective-one-body representation," Phys.Rev., vol. D85, p. 044025, 2012.

[227] T. Damour and A. Nagar, "An improved analytical description of inspiralling and coalescing black-hole binaries," Phys. Rev., vol. D79, p. 081503, 2009.

[228] D. Bini and T. Damour, "Gravitational radiation reaction along general orbits in the effective one-body formalism," Phys.Rev., vol. D86, p. 124012, 2012.

[229] M. Pürrer and C.-J. Haster, "Gravitational waveform accuracy requirements for future ground-based detectors," Phys. Rev. Res., vol. 2, no. 2, p. 023151, 2020.

[230] P. Rettegno, F. Martinetti, A. Nagar, D. Bini, G. Riemenschneider, and T. Damour, "Comparing Effective One Body Hamiltonians for spin-aligned coalescing binaries," 2019.

[231] D. Bini, T. Damour, and A. Geralico, "Spin-dependent two-body interactions from gravitational self-force computations," Phys. Rev., vol. D92, no. 12, p. 124058, 2015. [Erratum: Phys. Rev.D93,no.10,109902(2016)].

[232] S. Akcay, L. Barack, T. Damour, and N. Sago, "Gravitational self-force and the effective-one-body formalism between the innermost stable circular orbit and the light ring," Phys. Rev., vol. D86, p. 104041, 2012.

[233] A. Nagar, "Effective one body Hamiltonian of two spinning black-holes with next-to-next-to-leading order spin-orbit coupling," Phys.Rev., vol. D84, p. 084028, 2011.

[234] A. Rasskazov and B. Kocsis, "The rate of stellar mass black hole scattering in galactic nuclei," Astrophys. J., vol. 881, p. 20, 2019.

[235] H. Tagawa, Z. Haiman, and B. Kocsis, "Formation and Evolution of Compact Object Binaries in AGN Disks," Astrophys. J., vol. 898, no. 1, p. 25, 2020.

[236] M. Zevin, J. Samsing, C. Rodriguez, C.-J. Haster, and E. Ramirez-Ruiz, "Eccentric Black Hole Mergers in Dense Star Clusters: The Role of Binary–Binary Encounters," Astrophys. J., vol. 871, no. 1, p. 91, 2019.

[237] J. Samsing and D. J. D'Orazio, "Black Hole Mergers From Globular Clusters Observable by LISA I: Eccentric Sources Originating From Relativistic N-body Dynamics," Mon. Not. Roy. Astron. Soc., vol. 481, no. 4, pp. 5445–5450, 2018.

[238] M. Punturo, M. Abernathy, F. Acernese, B. Allen, N. Andersson, et al., "The third generation of gravitational wave observatories and their science reach," Class.Quant.Grav., vol. 27, p. 084007, 2010.

[239] P. Amaro-Seoane, "Detecting Intermediate-Mass Ratio Inspirals From The Ground And Space," Phys. Rev. D, vol. 98, no. 6, p. 063018, 2018.

[240] W. E. East, S. T. McWilliams, J. Levin, and F. Pretorius, "Observing complete gravitational wave signals from dynamical capture binaries," Phys. Rev., vol. D87, no. 4, p. 043004, 2013.

[241] N. Loutrel, "Repeated Bursts: Gravitational Waves from Highly Eccentric Binaries," 9 2020.

[242] I. M. Romero-Shaw, P. D. Lasky, E. Thrane, and J. C. Bustillo, "GW190521: orbital eccentricity and signatures of dynamical formation in a binary black hole merger signal," Astrophys. J. Lett., vol. 903, no. 1, p. L5, 2020.

[243] V. Gayathri, J. Healy, J. Lange, B. O'Brien, M. Szczepanczyk, I. Bartos, M. Campanelli, S. Klimenko, C. O. Lousto, and R. O'Shaughnessy, "Eccentricity estimate for black hole mergers with numerical relativity simulations," Nature Astron., vol. 6, no. 3, pp. 344–349, 2022.

[244] R. Gold and B. Brügmann, "Eccentric black hole mergers and zoom-whirl behavior from elliptic inspirals to hyperbolic encounters," Phys. Rev., vol. D88, no. 6, p. 064051, 2013.

[245] P. E. Nelson, Z. B. Etienne, S. T. McWilliams, and V. Nguyen, "Induced Spins from Scattering Experiments of Initially Nonspinning Black Holes," Phys. Rev. D, vol. 100, no. 12, p. 124045, 2019.

[246] Y.-B. Bae, H. M. Lee, and G. Kang, "Gravitational Wave Capture in Spinning Black Hole Encounters," Astrophys. J., vol. 900, no. 2, p. 175, 2020.

[247] T. Damour, F. Guercilena, I. Hinder, S. Hopper, A. Nagar, et al., "Strong-Field Scattering of Two Black Holes: Numerics Versus Analytics," 2014.

[248] A. Nagar, P. Rettegno, R. Gamba, and S. Bernuzzi, "Effective-one-body waveforms from dynamical captures in black hole binaries," Phys. Rev. D, vol. 103, no. 6, p. 064013, 2021.

[249] D. Bini and T. Damour, "Analytical determination of the two-body gravitational interaction potential at the fourth post-Newtonian approximation," Phys.Rev., vol. D87, no. 12, p. 121501, 2013.

[250] T. Damour, P. Jaranowski, and G. Schäfer, "Fourth post-Newtonian effective one-body dynamics," Phys. Rev., vol. D91, no. 8, p. 084024, 2015.

[251] T. Damour, P. Jaranowski, and G. Schäfer, "Conservative dynamics of two-body systems at the fourth post-Newtonian approximation of general relativity," Phys. Rev., vol. D93, no. 8, p. 084014, 2016.

[252] Z. Cao and W.-B. Han, "Waveform model for an eccentric binary black hole based on the effective-one-body-numerical-relativity formalism," Phys. Rev., vol. D96, no. 4, p. 044028, 2017.

[253] X. Liu, Z. Cao, and L. Shao, "Validating the Effective-One-Body Numerical-Relativity Waveform Models for Spin-aligned Binary Black Holes along Eccentric Orbits," 2019.

[254] T. Islam, V. Varma, J. Lodman, S. E. Field, G. Khanna, M. A. Scheel, H. P. Pfeiffer, D. Gerosa, and L. E. Kidder, "Eccentric binary black hole surrogate models for the gravitational waveform and remnant properties: comparable mass, nonspinning case," 1 2021.

[255] Q. Yun, W.-B. Han, X. Zhong, and C. A. Benavides-Gallego, "Surrogate model for gravitational waveforms of spin-aligned binary black holes with eccentricities," Phys. Rev. D, vol. 103, no. 12, p. 124053, 2021.

[256] A. Sesana, "Self consistent model for the evolution of eccentric massive black hole binaries in stellar environments: implications for gravitational wave observations," Astrophys. J., vol. 719, pp. 851–864, 2010.

[257] K. Breivik, C. L. Rodriguez, S. L. Larson, V. Kalogera, and F. A. Rasio, "Distinguishing Between Formation Channels for Binary Black Holes with LISA," Astrophys. J. Lett., vol. 830, no. 1, p. L18, 2016.

[258] R. Gamba, M. Breschi, G. Carullo, P. Rettegno, S. Albanesi, S. Bernuzzi, and A. Nagar, "GW190521: A dynamical capture of two black holes," Submitted to Nature Astronomy, June 2021.

[259] M. Levi and J. Steinhoff, "Complete conservative dynamics for inspiralling compact binaries with spins at fourth post-Newtonian order," 2016.

[260] A. Nagar and P. Rettegno, "The next generation: Impact of high-order analytical information on effective one body waveform models for noncircularized, spin-aligned black hole binaries," 8 2021.

[261] "Updated Advanced LIGO sensitivity design curve." `https://dcc.ligo.org/LIGO-T1800044/public`.